Debris Flow Runout Analysis in Mocoa, Colombia

Surging and Non-Simultaneous Landslides

A Master's Thesis Report

M.A. Muthanna

Delft University of Technology

TU Delft

Debris Flow Runout Analysis in Mocoa, Colombia

Surging and Non-Simultaneous Landslides

by

M.A. Muthanna

to obtain the degree of Master of Science
at the Delft University of Technology,
to be defended publicly on 23rd August, 2024

Student number: 5714494
Project duration: January 1, 2023 – August 23, 2024

Supervision Team: Dr. M.A. Cabrera (TU Delft)
Dr. A.Leonardi (University of Sheffield)

Thesis Committee: Dr. M.A. Cabrera (chair) (TU Delft)
Dr. R.C.Lindenbergh (TU Delft)
Dr. L.Flessati (TU Delft)

Cover Photograph: An aerial view of a large landslide in Mocoa courtesy Jaime Saldarriaga/Reuters via the I.B. Times [1].
An electronic version of this thesis is available at http://repository.tudelft.nl/.

TU Delft

Preface

I dedicate this thesis to the victims of the Mocoa 2017 tragedy.

I am deeply grateful for the guidance and support of my thesis committee, Dr. Cabrera, Dr. Lindenbergh, and Dr. Flessati, who were incredibly generous with their time. I hope my thesis does justice to their effort of mentoring me.

I would also like to express my great appreciation for the advice provided by Dr. Alessandro Leonardi, whose original idea was to explore this fascinating topic. Many thanks to Carolina Castro Malaver for her help at the start of my thesis.

Finally, I must thank my family for their enduring support and encouragement.

M.A. Muthanna
Delft, August 2024

Summary

Debris flows are extremely rapid gravity-driven mass movements of saturated sediment in concentrations between 60% to 80% by volume that move along steep channels, eroding and entraining material, typically terminating in a fan-shaped deposit. Debris flows are responsible for causing innumerable deaths and extensive damage across the world. The mobilisation of rainfall-triggered landslides is the primary cause of such flows. Estimating the debris flow travel distance or runout is essential for managing this hazard.

The conventional approach to debris flow runout analysis idealises the triggering of landslides across the source area into an instantaneous event. When this idealisation is done, a key characteristic of debris flows, their tendency to propagate in surges or waves, is overlooked. This study analyses the effect of accounting for surging on runout estimation by spatially and time-resolving debris flow events. A prime candidate for such a study is the Mocoa Debris Flow of 2017, a tragedy that involved 273 shallow landslides mobilising into a debris flow, resulting in the death of more than 300 people and the devastation of local infrastructure [2]. First, the landslide inventory was analysed to assess the scale of the disaster. Then, a novel method to spatially resolve events based on stream orders is implemented, after which a runout analysis is performed for different spatially resolved scenarios using a depth-averaged numerical model. Next, the timing and distribution of landslides are assessed based on a four-day storm period using a process-based landslide susceptibility model. This assessment determines the relative volume of each debris flow surge. The surges are then incorporated into a time-resolved runout analysis. The results of both the spatially and time-resolved runout analyses are compared. We find a marginal difference in the estimate of runout based on critical performance criteria, such as area coverage ratio, in favour of the spatially resolved analysis.

This study concludes that incorporating the phenomenon of surging caused by non-simultaneous landslide events does not improve the forensic analysis of the Mocoa Debris Flow runout. One of the main limitations of this study is the absence of data measured during the event to confirm the extent of surging due to non-simultaneous landslides. A possible avenue for future research would be varying the period of rainfall that is considered by reevaluating initial groundwater conditions.

Contents

Preface i

Summary ii

1 Background 1
1.1 Shallow Landslides and Debris Flows . . . 1
1.1.1 Shallow Landslides . . . 1
1.1.2 Debris Flows . . . 4
1.2 Landslide Susceptibility and Debris Flow Hazard Analysis . . . 8
1.2.1 Landslide Susceptibility . . . 8
1.2.2 Runout Analysis . . . 9
1.2.3 Debris Flow Hazard Analysis . . . 10
1.3 Time-Resolved Triggering and Runout Analysis of Rainfall-Induced Shallow Landslides 12
1.3.1 Surging and its Significance . . . 12
1.3.2 Influential Works . . . 13
1.4 Case Study: Mocoa, 2017 . . . 14
1.4.1 Study Area Description . . . 15
1.4.2 Event Summary . . . 16
1.5 Conclusion . . . 18

2 Research Questions and Methodology 19
2.1 Research Questions . . . 19
2.2 Methodology . . . 19
2.3 Rapid Mass Movement Simulation (RAMMS) . . . 21
2.3.1 Introduction . . . 21
2.3.2 Model Assumptions . . . 21
2.3.3 Working Principle . . . 21
2.3.4 Rheology . . . 23
2.3.5 Limitations . . . 24
2.3.6 Conclusion . . . 25
2.3.7 RAMMS General Input . . . 25
2.4 Landslide Inventory Analysis . . . 26
2.5 Demarcating Sub Basins . . . 27
2.6 Transient Rainfall Infiltration and Grid-Based Regional Slope-Stability Model (TRIGRS) 31
2.6.1 Introduction . . . 31
2.6.2 Model Assumptions . . . 32
2.6.3 Working Principle . . . 33
2.6.4 Limitations . . . 33
2.6.5 Conclusion . . . 34
2.6.6 TRIGRS Analysis . . . 35
2.7 Simulation Approach . . . 38
2.8 Scenario Performance Assessment Criteria . . . 40
2.8.1 Area Ratios . . . 40
2.8.2 Release Ratio . . . 40
2.8.3 Velocity and Width at Cross-Sections of Interest . . . 40

3 Runout Analysis 42
3.1 Introduction to The Analysis . . . 42
3.2 Spatially Resolved Analysis . . . 42
3.2.1 Spatially Resolved Analysis Whole Source Area: Block Releases . . . 43

3.2.2 Spatially Resolved Analysis Highland Source Area: Block Releases 47
3.3 Time-Resolved Analysis 50
3.3.1 Debris Flow Surge Assessment 50
3.3.2 Time-Resolved Scenario Analysis: Block Releases 51
3.4 Simulation Numerical Volume Loss 55

4 Results and Discussion **57**
4.1 Spatially Resolved Results 57
4.1.1 Spatially Resolved Whole Source Area Results 57
4.1.2 Spatially Resolved Highland Source Area Results 60
4.2 Time-Resolved Results 63
4.3 Comparison of Spatially and Time-Resolved Results 66
4.4 Summary of Results and Research Answers 69
4.5 Limitations of This Study and Recommendations for Future Studies 71

5 Conclusion **73**

References **76**

List of Figures

1.1 Worldwide fatalities due to rainfall-triggered landslides, courtesy NASA's Scientific Visualization Studio (2018) [4]. . . . 1
1.2 The estimated average annual number of significant $(> 1000sq.m)$ rainfall-triggered landslides from 1980-2018. Figure adapted from Redshaw and Bottomley (2020) [12]. . . . 2
1.3 Rockfall diagram adapted from Highland and Johnson (2006) [15]. . . . 3
1.4 Rotational Slide diagram adapted from Highland and Johnson (2006) [15]. . . . 3
1.5 A debris flow with flow size classification parameters labelled as seen in Table 1.3 from Jakob (2005a) [17]. . . . 4
1.6 Debris Flow schematic courtesy Pierson (1986) in Hungr (2005) [24] [16]. . . . 5
1.7 Debris Flow triggers as illustrated by Dowling and Santi (2013). Debris flows are predominantly triggered by rainfall events [23]. . . . 5
1.8 Fatal debris flow distribution 1951-2011 (non-exhaustive) courtesy Dowling and Santi (2013) [23]. . . . 6
1.9 Fatal debris flow distribution 1951-2011 (a non-exhaustive record) courtesy Dowling and Santi (2013) [23]. . . . 6
1.10 The potential scale of influence of debris flows of size class 4 to 6 from Jakob (2005a) [17]. . . . 7
1.11 The various methods of analysing landslide susceptibility adapted from Reichenbach et al. (2018) [25]. Both Inventory and Process-based methods are applied in this study. . . . 8
1.12 An overview of Runout Analysis Methods adapted from McDougall (2016) [26]. A Continuum model is employed in this study. . . . 9
1.13 The five key steps of debris flow hazard analysis according to Jakob (2005b) [31]. . . . 10
1.14 Inversely graded levees formed by a recent debris flow in Sacajawea State Park, United States of America. Image courtesy Travis Corthouts [32]. . . . 10
1.15 A hazard probability analysis with different scenarios adapted from Strouth et al. (2024) [33]. . . . 11
1.16 Results of a hazard intensity analysis with different scenarios courtesy Strouth et al. (2024) [33]. . . . 11
1.17 A typical debris flow hazard map with three hazard classes from Ouyang et al. (2019) [34]. 12
1.18 A hydrograph of the debris flow event in Pians, 2007 shows 14 surges as recorded by Araia et al. (2013) [35]. . . . 13
1.19 Two non-simultaneous landslides in the same basin with an overlapping runout adapted from Iverson et al. (2024) [36]. . . . 13
1.20 An aerial view of a large landslide in Mocoa, courtesy Jaime Saldarriaga/Reuters via The I.B. Times [1]. . . . 15
1.21 The Study Area ($75km^2$) with major rivers and creeks, as well as the measured debris flow runout, and the town of Mocoa in the South-West as represented by Google's Open Buildings dataset [42]. . . . 15
1.22 Daily rainfall in the Mocoa drainage basin for six months up to the 2017 event, adapted from Sarmiento et al. (2019) [2]. . . . 16
1.23 Multiple shallow landslides in the middle and upper part of the Taruca micro-basin courtesy Corpoamazonia via Mongabay [44]. . . . 17
1.24 An aerial view of the debris fan with the creeks and landmarks labelled and the destroyed Junín Power Substation (J.P.S.) in the distance, courtesy Jorge Castro in Garcia-Delgado et al. (2019) [43]. . . . 17

2.1 The methodology of this thesis. . . . 20
2.2 The relationship between the flow height "H" and "L" the flow length from Iverson (2005) [56]. . . . 21

2.3 Cartesian framework topography of the RAMMS model adopted from Christen et al. (2010) [55]. . . . 22
2.4 The range of values of μ and Chezy's coefficient (C), where ξ = C^2 for the forensic analysis of different mass movements including debris flows using Voellmy rheology adapted from C. Scheidel et al. (2013) in C. Margottini et al. (2013) [60]. . . . 23
2.5 A view of the solid-liquid constituents of a debris flow showing the percentage of solids concentration ϕ_s adapted from Meyrat et al. (2024) [62]. . . . 24
2.6 Modifications made to the D.E.M. The dashed line indicates the region bounded by the fenced area, while the stream can be seen to the line's immediate left in the centre of the map. . . . 25
2.7 The study area with landslides that contributed to the Mocoa Debris Flow event along with the major rivers and creeks. . . . 26
2.8 The number of landslide events for a range of volumes as well as the cumulative number of events in the study area as seen in Scenarios 1 and 3. . . . 27
2.9 The stream network as produced by the Strahler Algorithm. . . . 28
2.10 The linearised stream network order. . . . 29
2.11 The single basin formed when considering the third order stream. This basin is used in Scenario 3. . . . 29
2.12 The number of landslide events for a range of volumes as well as the cumulative number of events when the study area is divided into four sub-basins as seen in Scenarios 4, 5, 8, and 10 [45]. . . . 30
2.13 The four sub-basins created by considering second and third-order streams. These sub-basins are used in Scenarios 4, 5, 8, and 10. . . . 30
2.14 The number of landslide events for a range of volumes as well as the cumulative number of events when the study area is divided into seven sub-basins, as seen in Scenarios 6, 7, 9, and 11. . . . 31
2.15 The seven sub-basins created by considering first, second and third order streams. These sub-basins are used in Scenarios 6, 7, 9, and 11. . . . 31
2.16 The TRIGRS hydrological model from Baum et al. (2008). The depth of the unsaturated layer is "d_u". While "Z_{max}" is the depth of the basal boundary from the ground surface. The depth of the soil above the water table is represented by "d", while "δ" is the slope angle. [40] . . . 32
2.17 An example of the TRIGRS output adapted from Savage et al. (2005) showing the unstable regions changing with time and rainfall [86]. . . . 34
2.18 Precipitation vs Time for the 102-hour storm period. . . . 35
2.19 TRIGRS Input: The 16 geotechnical zones demarcated by Chavarro et al. (2020) based on the parameters seen in Table 2.3 [87]. . . . 37
2.20 TRIGRS Output Factor of Safety at the sixteenth time step ($96h$). Red indicates unstable areas with yellow and green indicating stable areas. . . . 37
2.21 The three sections of interest. Sections 1, 2, and 3 within the study area. . . . 41

3.1 Block release locations of the four spatially resolved scenarios that consider the entire source area. . . . 43
3.2 The distribution of the modelled volume from each sub-basin of Scenarios 4 and 6. . . . 44
3.3 Maximum simulated runout heights for Scenarios 1 and 3. . . . 44
3.4 Maximum simulated runout heights for Scenarios 4 and 6. . . . 45
3.5 Maximum simulated runout velocities of the four spatially resolved scenarios that consider the entire source area. . . . 46
3.6 Block release locations of the three spatially resolved scenarios that consider only the highland source area. . . . 47
3.7 The distribution of the modelled volume from each sub-basin of Scenarios 5 and 7. . . . 48
3.8 Maximum simulated runout heights for Scenarios 2 and 5, considering only the highland source area. . . . 48
3.9 Maximum simulated runout height for Scenario 7, considering only the highland source area. . . . 49

3.10 Maximum simulated runout velocities of the three spatially resolved scenarios that consider only the highland source area. 50
3.11 Precipitation vs Time for the 102-hour storm period. 51
3.12 The distribution of debris flow volume as a response to rainfall over time and space when considering **four** sub-basins. 52
3.13 Block release locations of the time-resolved scenarios considering four sub-basins, Scenarios 8 and 10. 52
3.14 The distribution of debris flow volume as a response to rainfall over time and space when considering **seven** sub-basins. 53
3.15 Block release locations of the time-resolved scenarios considering seven sub-basins, Scenarios 9 and 11. 53
3.16 Maximum simulated runout heights of the four time-resolved scenarios. Scenarios 8 and 10 are based on four sub-basins and do and do not consider deposition, respectively. Scenarios 9 and 11 are based on seven sub-basins and do and do not consider deposition, respectively. 54
3.17 Maximum simulated runout velocities of the four time-resolved scenarios. 55

4.1 Area coverage and outrun ratios for the spatially resolved scenarios considering the whole source area. 58
4.2 Width ratios at the three critical sections for the spatially resolved scenarios considering the whole source area. 59
4.3 Velocity at the three critical sections for the spatially resolved scenarios considering the whole source area. 60
4.4 Area coverage and outrun ratios for the spatially resolved scenarios considering the highland source area. 61
4.5 Width ratios at the three critical sections for the spatially resolved scenarios considering the highland source area. 62
4.6 Velocity at the three critical sections for the spatially resolved scenarios considering the highland source area. 63
4.7 Area coverage and outrun ratios for the time-resolved scenarios 64
4.8 Width ratios at the three critical sections for the time-resolved scenarios 65
4.9 Velocity at the three critical sections for the time-resolved scenarios. 66
4.10 Comparing the area coverage and outrun ratios for the spatially and time-resolved scenarios. 67
4.11 Comparing the width ratios at the three critical sections for the spatially and time-resolved scenarios 68
4.12 Comparing velocity at the three critical sections for the spatially and time-resolved scenarios. 69
4.13 Area Coverage ratio for all scenarios. 70
4.14 Area Outrun ratio for all scenarios. 70

List of Tables

1.1 Landslide velocity scale adapted from Hungr et al. (2014) [13]. 2
1.2 Landslide movement classification adapted from Hungr et al. (2014) [13]. 3
1.3 Debris flow size classification adapted from Jakob (2005a) [17]. For a description of the potential consequences of each class, see Table 1.4. 7
1.4 Debris flow potential consequences according to the size classification by Jakob (2005a) [17]. For a quantitative measure of each class, see Table 1.3. 7

2.1 RAMMS General Input. 25
2.2 TRIGRS Input. 35
2.3 Geotechnical and hydraulic parameters for each of the 16 zones seen in Figure 2.19 courtesy Chavarro et al. (2020) [87]. 36
2.4 The simulation program consists of eleven scenarios. The horizontal line after Scenario 7 indicates the separation between the spatially resolved scenarios above the line and the time-resolved scenarios below it. 39

3.1 Numerical Volume Losses. 56

1

Background

1.1. Shallow Landslides and Debris Flows

1.1.1. Shallow Landslides

From 2004 to 2016, an estimated $55,997$ people were killed in $4,862$ distinct non-seismic landslide events [3]. The Global Landslide Catalog created by the National Aeronautics and Space Administration (NASA) reports $11,033$ rainfall-triggered landslides occurring worldwide from 2007 to 2019 as seen in Figure 1.1 [4].

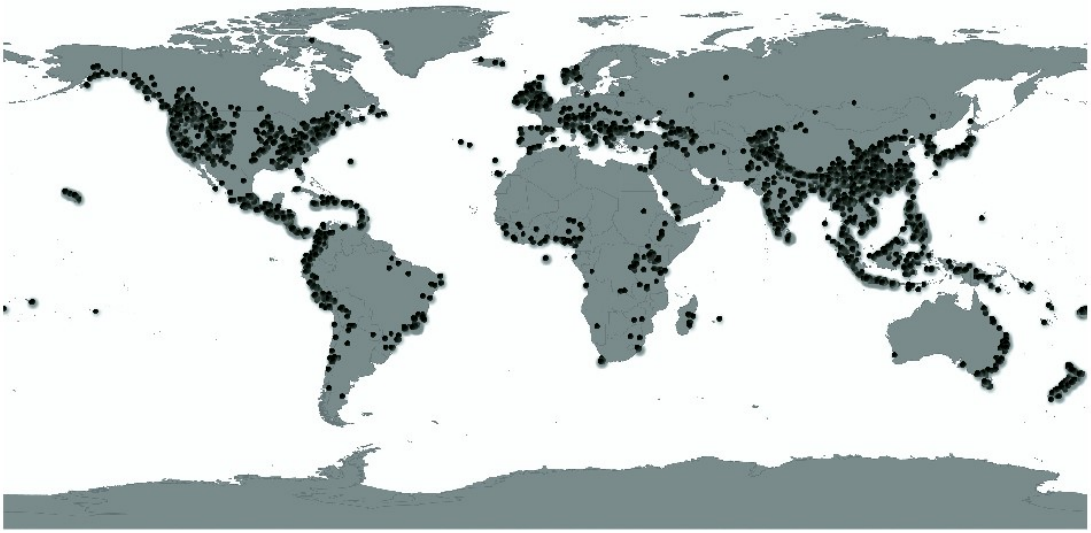

Figure 1.1: Worldwide fatalities due to rainfall-triggered landslides, courtesy NASA's Scientific Visualization Studio (2018) [4].

The lack of a complete database of events makes studying landslides, especially rainfall-triggered landslides, challenging. Eeckhaut and Hervás (2012) report that global landslide catalogues like the Emergency Events Database (EM-DAT) underestimate landslide occurrences [5]. They also found a significant disagreement between databases on the regional and national scales in Europe [5]. Dandridge et al. (2023) stated that a strong positive correlation exists between the economic status of a country and landslide reporting. They also say that a reporting bias towards predominantly English-speaking countries exists due to the method of compilation of NASA's Global Landslide Catalog (G.L.C.) [6]. According to Dandridge et al. (2023), landslide reporting is biased towards areas with high population densities, such as urban areas. Consequently, rural areas of non-English speaking countries such as Colombia are underrepresented in the database [6]. The disagreement between various databases makes assessing the true impact of landslides on a global scale difficult. However, the devastating

effect of standalone events on a local scale is undeniable. For instance, the 2013 landslides, which killed over $6,000$ people in India [7]. Or the landslides in Vargas, Venezuela(1999), which killed approximately $30,000$ people [8]. Landslides are an increasingly worrying hazard, with Froude and Petley (2018) finding that construction, illegal mining, and hill cutting are increasing the susceptibility of slopes to rainfall-triggered sliding [3]. Cheng et al. (2018) state that with the increase in extreme weather events, compound disaster events will increase, especially in adequate-rainfall mountainous areas [9]. Pei et al. (2023) have confirmed this possibility by describing an exponential relation between warming temperatures and the number of landslides in the Taxkorgan River basin [10]. The consensus is that the frequency of such events is increasing with time [9] [3] [10]. While the database of landslides is not perfect, the mechanisms themselves are formally classified. The United Nations International Strategy for Disaster Reduction defines landslides as "a variety of processes that result in the downward and outward movement of slope-forming materials, including rock, soil, and artificial fill/The materials may move by falling, toppling, sliding, spreading, flowing, or slope deformation" (UNISDR, 2017, p.30) [11].

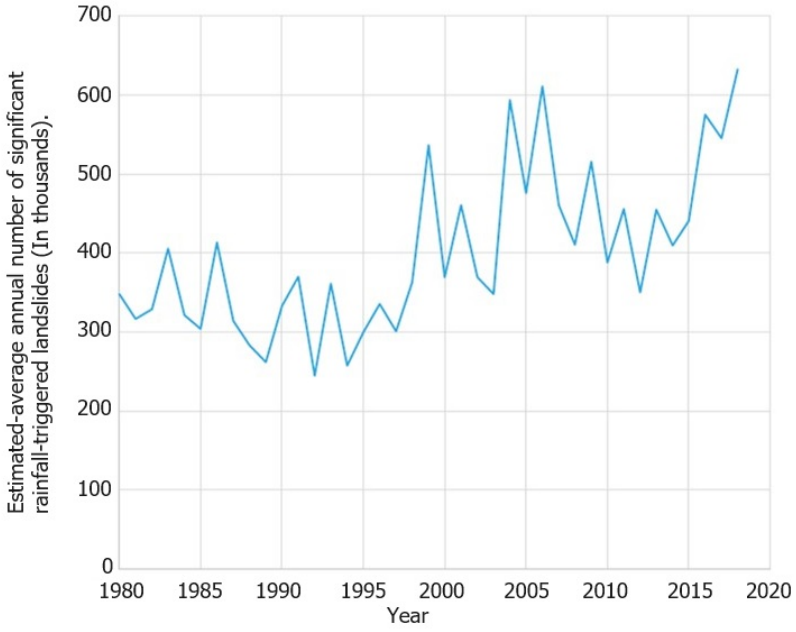

Figure 1.2: The estimated average annual number of significant $(> 1000sq.m)$ rainfall-triggered landslides from 1980-2018. Figure adapted from Redshaw and Bottomley (2020) [12].

Mass Movements are grouped by their velocity in Table 1.1 as recommended by Hungr et al. (2014) [13]. Along with the classification by velocity, The updated Varnes classification of landslides proposed by Hungr et al. (2014) formally defines thirty-two categories based on movement and material [13]. Six main types of movements exist in the updated Varnes classification of landslides [13]. Each type is broadly split into rock or soil with further sub-types, resulting in thirty-two distinct movements as seen in Table 1.2 [13]. The movements seen in Table 1.2 are either caused by anthropogenic intervention (mining, excavation, and other slope destabilising activities) or by natural processes such as seismicity, volcanic activity, or precipitation [14].

Table 1.1: Landslide velocity scale adapted from Hungr et al. (2014) [13].

Velocity Class	Description	Velocity (mm/s)	Typical Velocity
7	Extremely rapid	5×10^{3}	5 m/s
6	Very rapid	5×10^{1}	3 m/min
5	Rapid	5×10^{-1}	1.8 m/h
4	Moderate	5×10^{-3}	13 m/month
3	Slow	5×10^{-5}	1.6 m/year
2	Very slow	5×10^{-7}	16 mm/year
1	Extremely slow	-	-

Table 1.2: Landslide movement classification adapted from Hungr et al. (2014) [13].

Type of Movement	Rock	Soil
Fall	1. Rock/ice fall	2. Boulder/debris/silt fall
Topple	3. Rock block topple	5. Gravel/sand/silt topple
	4. Rock flexural topple	
Slide	6. Rock rotational slide	11. Clay/silt rotational slide
	7. Rock planar slide	12. Clay/silt planar slide
	8. Rock wedge slide	13. Gravel/sand/debris slide
	9. Rock compound slide	14. Clay/silt compound slide
	10. Rock irregular slide	
Spread	15. Rock slope spread	16. Sand/silt liquefaction spread
		17. Sensitive clay spread
Flow	18. Rock/ice avalanche	19. Sand/silt/debris dry flow
		20. Sand/silt/debris flowslide
		21. Sensitive clay flowslide
		22. Debris flowslide
		23. Mudflow
		24. Debris flood
		25. Debris avalanche
		26. Earthflow
		27. Peat flow
Slope deformation	28. Mountain slope deformation	30. Soil slope deformation
	29. Rock slope deformation	31. Soil creep
		32. Solifluction

The common mechanisms seen in tropical mountainous rainfall-triggered landslides are Rockfalls, Rotational Landslides and Debris Flows. (a) Rockfall is the detachment, very to extremely rapid free-fall falling, rolling, and bouncing of rocks, occurring singly or in clusters as seen in Figure 1.3 [14]. Fragments move as independent rigid bodies interacting with the substrate through episodic impacts [14]. Such a phenomenon is common to steep slopes in coastal areas and along riverbanks. It is usually triggered by undercutting slopes either naturally or by anthropogenic causes [15]. (b) Rotational Slide is the slow to rapid sliding of a mass of homogeneous and typically cohesive soil along a curved failure surface as seen in Figure 1.4 [13]. Rotational Slides are typically triggered by rainfall/rapid snowmelt/rapid changes in groundwater levels or earthquakes in slopes inclined between $20 - 40^o$ [14]. This study focuses on rainfall-triggered debris flows, as seen in the next section, Sub-Section 1.1.2 .

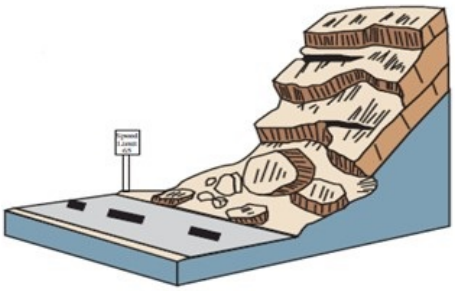

Figure 1.3: Rockfall diagram adapted from Highland and Johnson (2006) [15].

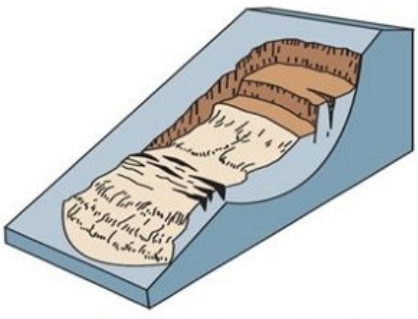

Figure 1.4: Rotational Slide diagram adapted from Highland and Johnson (2006) [15].

1.1.2. Debris Flows

Debris Flows are the very to extremely rapid surging flow of saturated debris in a steep channel $(20-45^o)$ as shown in Figure 1.5 [16] [13]. The initial mass movement enters channels such as streams or gullies, entraining loose material along the way, and terminates as a fan-shaped deposit known as a debris fan [16].

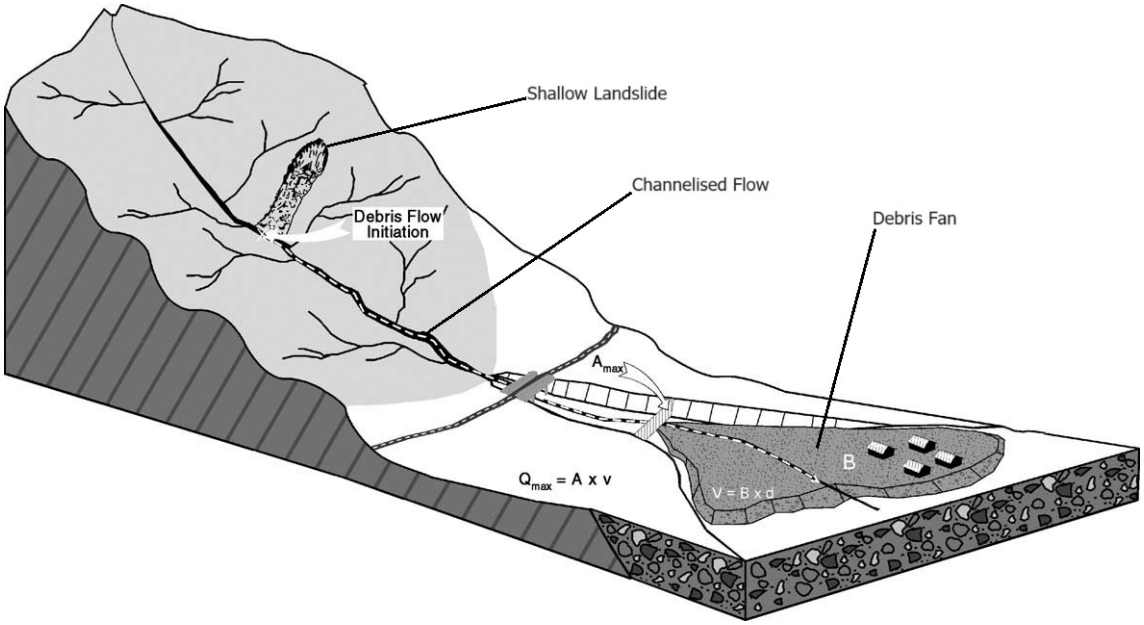

Figure 1.5: A debris flow with flow size classification parameters labelled as seen in Table 1.3 from Jakob (2005a) [17].

Debris is defined as " loose unsorted material of low plasticity" (Hungr et al., 2001, p.224) along with entrained organic material like logs and mulch produced by natural processes such as mass wasting or anthropogenic means like mine spoil [18]. Debris flows usually contain material from both ends of the grain-size classification spectrum from boulders to clay and are sometimes gap-graded [16]. According to Vallance (2024), the solid and liquid constituents of a debris flow move together and can be approximated as a single phase with roughly equal solid and liquid fractions by volume [19]. Whereas a stream flow has fine-grained sediments suspended in a fluid and coarse-grained sediments transported as a bed load, forming two distinct phases with little particle-to-particle interaction [19]. A transitional flow phase, called hyper-concentrated flow, has characteristics between that of stream flows and debris flows, carrying higher sediment loads than a stream flow but still separated into two phases, unlike a debris flow [19]. Vallance (2024) says that exact flow-phase transition points in terms of solid fraction cannot be defined as transitions are gradual and dependent on sediment-size distribution and the energy of the flow [19]. A typical debris flow schematic is shown in Figure 1.6 illustrating the transition of a hyper-concentrated flow to a fully formed debris flow as solid particles are entrained, resulting in an increase in the concentration of solids as compared to the liquid volume. The diagram also shows the development of a boulder front at the head of the debris flow due to the characteristic inverse sorting seen in debris flows where coarse grains congregate near the head of the flow, and finer grains are present in the tail [20]. The boulder front is preceded by a precursory watery surge [16]. Unlike debris avalanches, debris flows are specific to a given path and deposition area or debris fan [13]. Debris flows are common in steep gullies and canyons that lack vegetation and in volcanic regions with weak soil [13]. Debris flows have bulk densities that commonly vary from about $1,600$ to $2,400 kg/m^3$ [21]. Pierson (2005) defines debris flows as having sediment concentration in excess of 60% by volume or 80% by weight [22]. The flow is often initiated by landslides or rockfalls, themselves triggered by earthquakes or, more commonly, intense rainfall [13]. Figure 1.7 from Dowling and Santi (2013) shows the common triggers of fatal debris flows between 1951 and 2011, with rainfall events being the dominant cause [23].

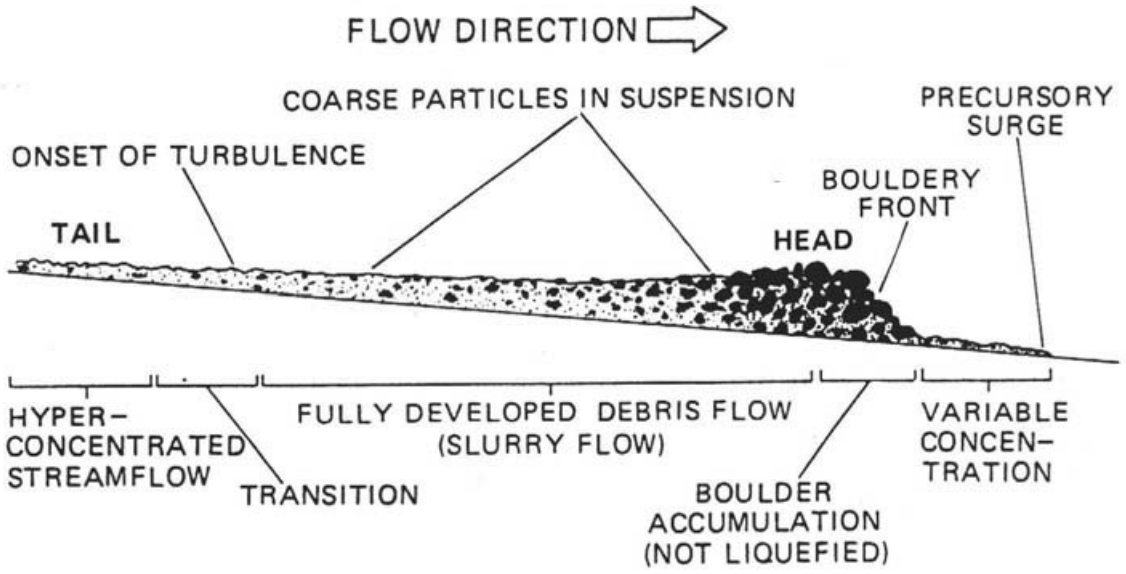

Figure 1.6: Debris Flow schematic courtesy Pierson (1986) in Hungr (2005) [24] [16].

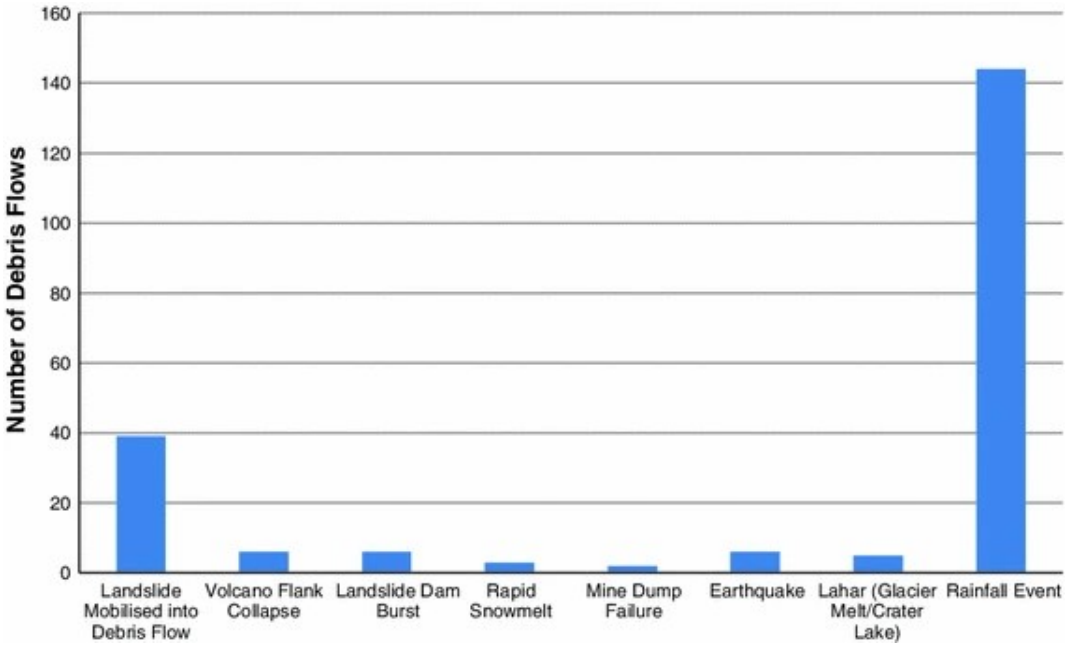

Figure 1.7: Debris Flow triggers as illustrated by Dowling and Santi (2013). Debris flows are predominantly triggered by rainfall events [23].

Debris flows are widespread, as seen in Figure 1.8 from Dowling and Santi (2013), which shows the distribution of fatal debris flows over sixty years from 1951-2011 and is complimented by Figure 1.9 by Dowling and Santi (2013) that shows the frequency of fatal debris flows over the same sixty year period [23].

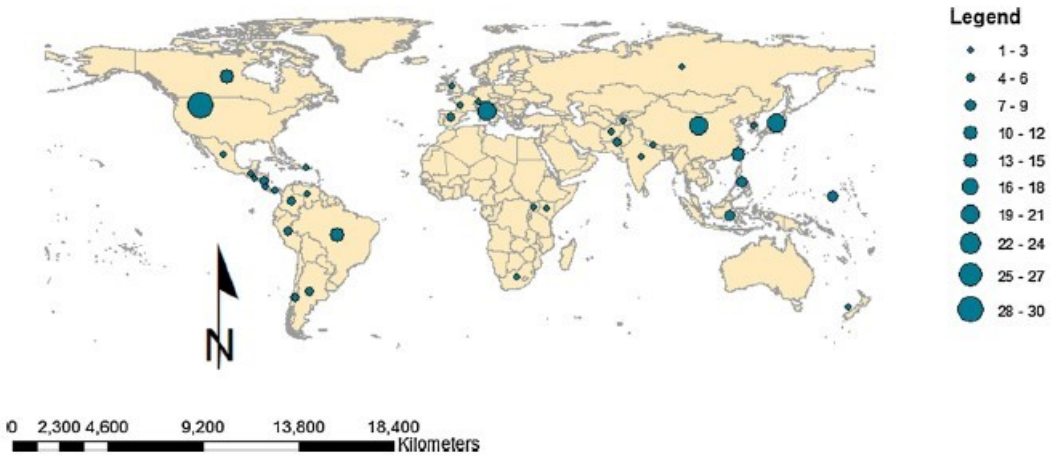

Figure 1.8: Fatal debris flow distribution 1951-2011 (non-exhaustive) courtesy Dowling and Santi (2013) [23].

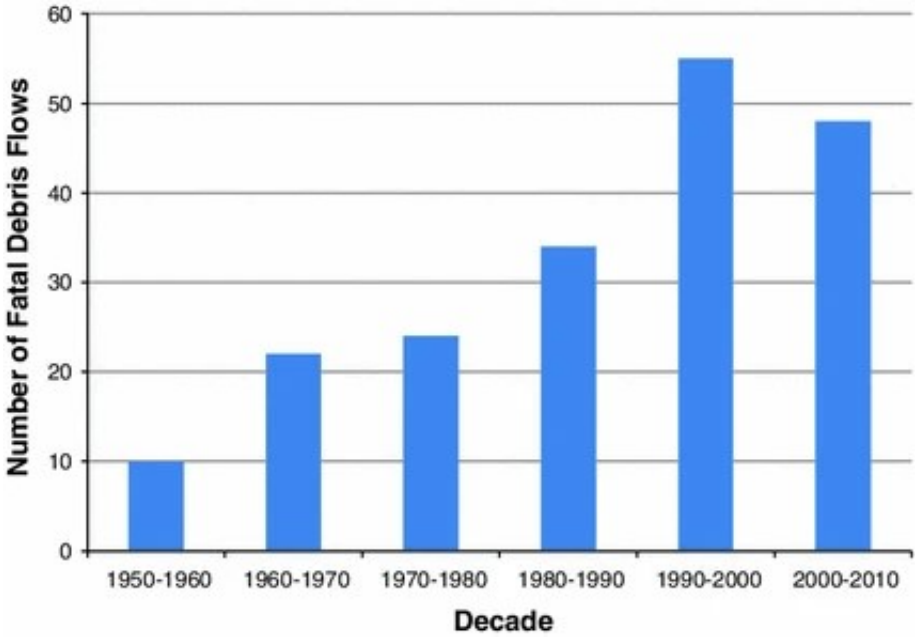

Figure 1.9: Fatal debris flow distribution 1951-2011 (a non-exhaustive record) courtesy Dowling and Santi (2013) [23].

Jakob (2005a) proposed a ten-scale size classification scheme for debris flows based on volume, area inundated and peak discharge as seen in Table 1.3 along with the potential consequences of such events as seen in Table 1.4 [17]. This scale can be related to the area affected by the debris flow and its nature (volcanic or boulder). In Table 1.3, V is the total volume, Q_b and Q_v are the peak discharge for boulder and volcanic debris flows, respectively, B_b and B_v are the area inundated by boulder and volcanic debris flows, respectively, as seen in Figure 1.5. N/A signifies events of this size have not been observed [17]. The peak discharge of Jakob's scale compliments the landslide velocity scale of Hungr et al. (2014), as seen in Table 1.1 [17] [13]. Figure 1.10 illustrates the relative size of large debris flows and how the different size classes, as seen in Table 1.4, affect settlements in valleys. [17].

Table 1.3: Debris flow size classification adapted from Jakob (2005a) [17]. For a description of the potential consequences of each class, see Table 1.4.

Size class	V, **range** (m^3)	Q_b, **range** (m^3/s)	Q_v, **range** (m^3/s)	B_b (m^2)	B_v (m^2)
1	$< 10^2$	< 5	< 1	$< 4 \times 10^2$	$< 4 \times 10^3$
2	$10^2 - 10^3$	$5 - 30$	$1 - 3$	$4 \times 10^2 - 2 \times 10^3$	$4 \times 10^3 - 2 \times 10^4$
3	$10^3 - 10^4$	$30 - 200$	$3 - 30$	$2 \times 10^3 - 9 \times 10^3$	$2 \times 10^4 - 9 \times 10^4$
4	$10^4 - 10^5$	$200 - 1500$	$30 - 300$	$9 \times 10^3 - 4 \times 10^4$	$9 \times 10^4 - 4 \times 10^5$
5	$10^5 - 10^6$	$1500 - 12,000$	$300 - 3 \times 10^3$	$4 \times 10^4 - 2 \times 10^5$	$4 \times 10^5 - 2 \times 10^6$
6	$10^5 - 10^6$	N/A	$3 \times 10^3 - 3 \times 10^4$	$> 2 \times 10^5$	$2 \times 10^6 - 3 \times 10^7$
7	$10^6 - 10^7$	N/A	$3 \times 10^4 - 3 \times 10^5$	N/A	$3 \times 10^7 - 3 \times 10^8$
8	$10^7 - 10^8$	N/A	$3 \times 10^5 - 3 \times 10^6$	N/A	$3 \times 10^8 - 3 \times 10^9$
9	$10^8 - 10^9$	N/A	$3 \times 10^6 - 3 \times 10^7$	N/A	$3 \times 10^9 - 3 \times 10^{10}$
10	$> 10^9$	N/A	$3 \times 10^7 - 3 \times 10^8$	N/A	$> 3 \times 10^{10}$

Table 1.4: Debris flow potential consequences according to the size classification by Jakob (2005a) [17]. For a quantitative measure of each class, see Table 1.3.

Size Class	**Potential Consequences**
1	Very localised damage, known to have killed forestry workers in small gullies, damage small buildings.
2	Could bury cars, destroy a small wooden building, break trees, block culverts, derail trains.
3	Could destroy larger buildings, damage concrete bridge piers, block or damage highways and pipelines.
4	Could destroy parts of villages, destroy sections of infrastructure corridors, bridges, could block creeks.
5	Could destroy parts of towns, destroy forests of $2\,\mathrm{km}^2$ in area, block creeks and small rivers.
6	Could destroy towns, obliterate valleys or fans up to several tens of km^2 in size, dam rivers.
7	Could destroy parts of cities, obliterate valleys or fans up to several tens of km^2 in size, dam large rivers.
8	Could destroy cities, inundate large valleys up to 100 km^2 in size, dam large rivers.
9	Vast and complete destruction over hundreds of km^2.
10	Vast and complete destruction over hundreds of km^2.

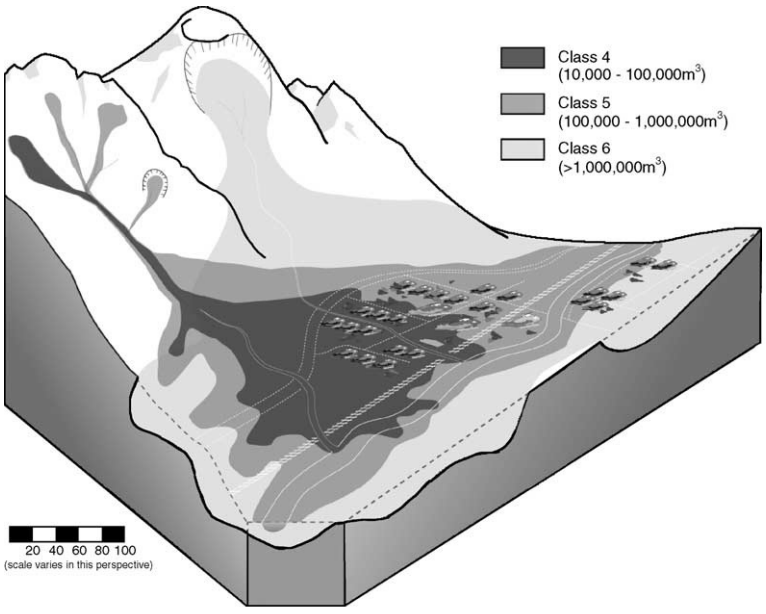

Figure 1.10: The potential scale of influence of debris flows of size class 4 to 6 from Jakob (2005a) [17].

According to Jakob (2005a), even the smallest debris flows have been known to cause localised damage and kill people [17]. With the largest debris flows capable of blocking small rivers and destroying parts of towns [17]. Debris flows are a global phenomenon with fatal consequences, deserving of further study and analysis.

1.2. Landslide Susceptibility and Debris Flow Hazard Analysis

1.2.1. Landslide Susceptibility

Landslide susceptibility and runout analysis are vital in debris flow hazard analysis. Effective landslide management is crucial given the range, complexity of movements, and fatal consequences. According to Reichenbach et al. (2018) [16], this includes (a) landslide susceptibility mapping, which involves identifying and mapping landslide-prone areas based on causation criteria, (b) hazard identification and mapping of areas that threaten human life or infrastructure along with probabilistic assessments, (c) risk assessment and management which involves determining the level of risk, its acceptability, and methods to reduce it [25].

A distinction is made between landslide "susceptibility" and "hazard" by Reichenbach et al. (2018) [25]. Susceptibility is defined as the probability of slope failures occurring in a given region within a set of geo-environmental conditions while disregarding the physical dimensions of the actual landslide [25]. While hazard is the probability that a landslide of a given magnitude will occur in a given period and area under certain geo-environmental conditions [25]. Per McDougall (2016), this terminology is typically used for the forward analysis of events [26]. La Porta et al. (2023) combine the "susceptibility" and the event magnitude into a single triggering phenomenon, terming the estimation of the post-failure characteristics such as flow volume, velocity, and composition, as the "runout problem" [27]. McDougall (2016) states that this terminology is typical of forensic analyses of mass movements and is also the terminology we will adopt for the rest of this work [26] According to Reichenbach et al. (2018), all landslide susceptibility mapping methods can be broadly grouped into five categories as in Figure 1.11 [25]:

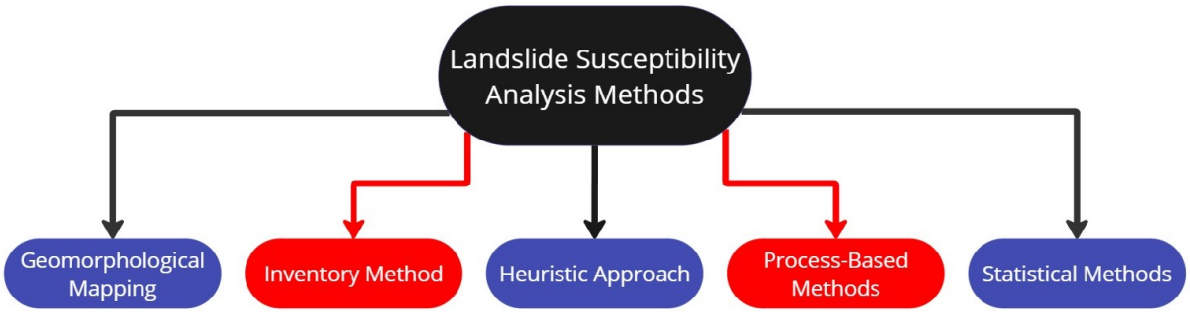

Figure 1.11: The various methods of analysing landslide susceptibility adapted from Reichenbach et al. (2018) [25]. Both Inventory and Process-based methods are applied in this study.

(a) Geomorphological Mapping depends on the expertise of the investigator, who evaluates and maps potential slides based on their understanding of the geomorphology of the study area. (b) The Inventory Method is based on the principle that history is the key to the future, meaning that landslides generally re-occur in areas, making it possible to predict where landslides will occur if case histories and landslide inventories are available [28]. (c) The Heuristic Approach is where investigators rank and weigh stability factors based on their expected importance. Again, this method relies on an individual's expertise. (d) Process-based methods are physics-based modelling schemes that analyse stability conditions using numerical models. (e) Statistical methods are based on analysing the functional relationships between known or inferred instability factors and the past and present distribution of landslides. The most common statistical methods are logistic regression and machine learning methods [25]. According to Reichenbach et al. (2018), process and statistics-based methods are preferred over all others to ascertain landslide susceptibility [25]. La Porta et al. (2023) agree with this as they say both methods are more advanced than alternatives by being strictly quantitative and, therefore, less reliant on an individual's expertise [27].

1.2.2. Runout Analysis

Runout is the distance travelled by a landslide from its origin. Landslide runout analysis is the analysis of post-mobilisation landslide motion. It determines the zones at risk from the mass movement. Runout distance is affected by the characteristics of the material, topography, land use, and vegetation in addition to the event size and trigger [29]. Runout analysis also helps assess the limits of secondary effects, such as waves, flooding, air blasts, and dust clouds [26]. Runout prediction is therefore required for landslide hazard assessment [26]. According to McDougall (2016) and Komu et al. (2023), runout analysis methods are bifurcated into three broad categories as seen in Figure 1.12; (a) Empirical–Statistical methods using statistical geometric correlations and (b) Analytical methods that use process-based modeling such as numerical models, continuum, discontinuum, and closed-form equations [26] [29]. Lastly, (c) Hybrid "semi-empirical" numerical models which are rarely employed [26].

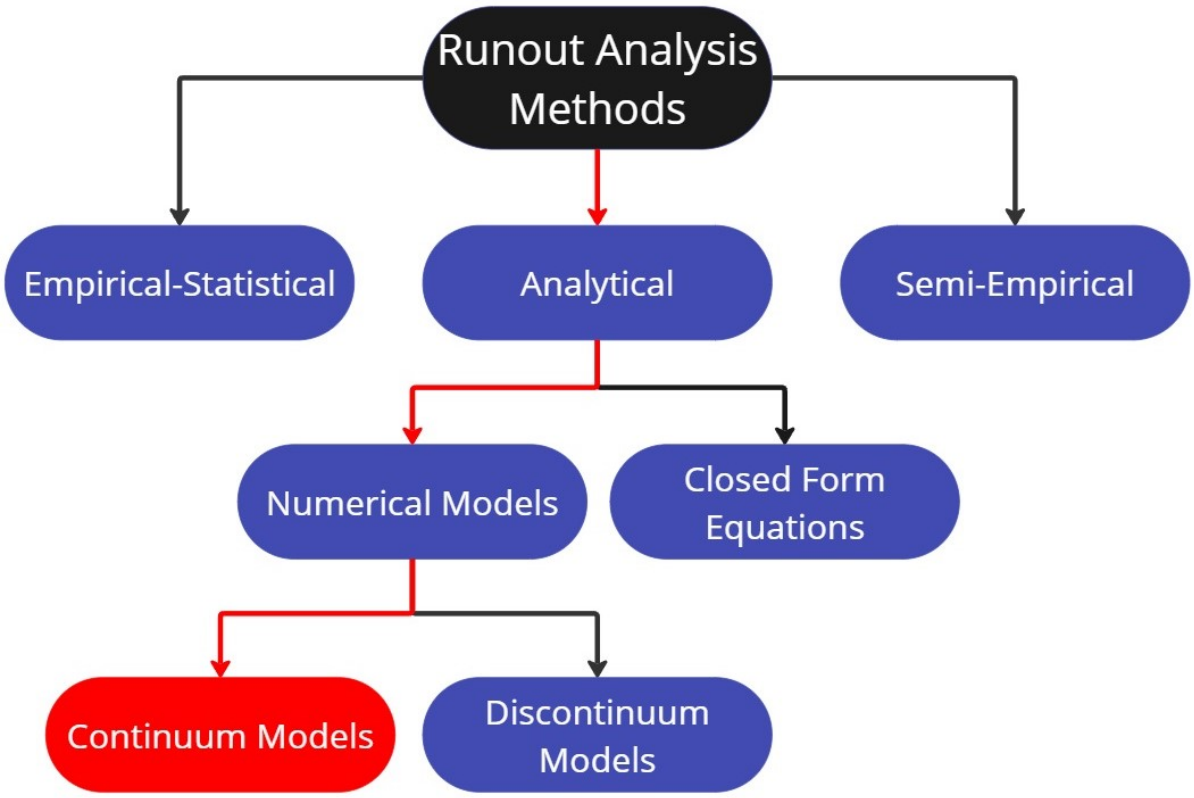

Figure 1.12: An overview of Runout Analysis Methods adapted from McDougall (2016) [26]. A Continuum model is employed in this study.

Empirical–statistical methods are based on simple geometric correlations [26]. They are rapid and express results in quantitative statistical terms [26]. These methods establish confidence limits of hazard assessment such as calculation of runout exceedance probability [26]. However, they cannot generate visualisations. Statistical methods are reliable and user-friendly but require high-quality input data [29]. Numerical models can estimate landslide intensity parameters such as flow depths and velocities. They also generate visualisations. McDougall (2016) states that most numerical models are continuum models based on depth-averaged shallow flow equations and account for the effects of entrainment, internal stresses, and rheology, often by employing empirical parameters in a single material phase, which makes them challenging to calibrate [26]. According to Sinha and Walton (2019), discontinuum models explicitly model geologic features on a smaller scale than continuum models and are limited to simulations of mm-scale grain-boundary contacts to m-scale rock joints [30].

1.2.3. Debris Flow Hazard Analysis

The widespread occurrence and fatal consequences of debris flows underscores the need for comprehensive debris flow hazard analysis. As per Hungr (2005), debris flow hazard assessment should estimate the likely behaviour of the flow as well as the intensity of the event within the hazard area, while the extent of the hazard area is in itself derived from a runout analysis, which in turn relates to landslide hazard assessment [16]. Jakob (2005b) outlines the steps of a debris flow hazard analysis as seen in Figure 1.13 [31]:

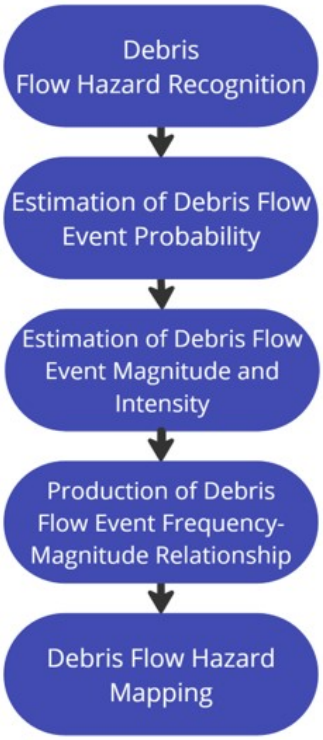

Figure 1.13: The five key steps of debris flow hazard analysis according to Jakob (2005b) [31].

(A) Debris Flow Hazard Recognition: This is based on field studies of geomorphic evidence such as inversely graded levee deposits as seen in Figure 1.14 and scour marks. Satellite imagery and historical records are also used to identify debris flow activity.

Figure 1.14: Inversely graded levees formed by a recent debris flow in Sacajawea State Park, United States of America. Image courtesy Travis Corthouts [32].

(B) Estimation of Debris Flow Event Probability: The likelihood of debris flow events occurring is related to the probability of shallow landslides occurring and the availability of erodible sediments. Event frequency, probability, and return period are determined as part of this step, as seen in Figure 1.15 [33].

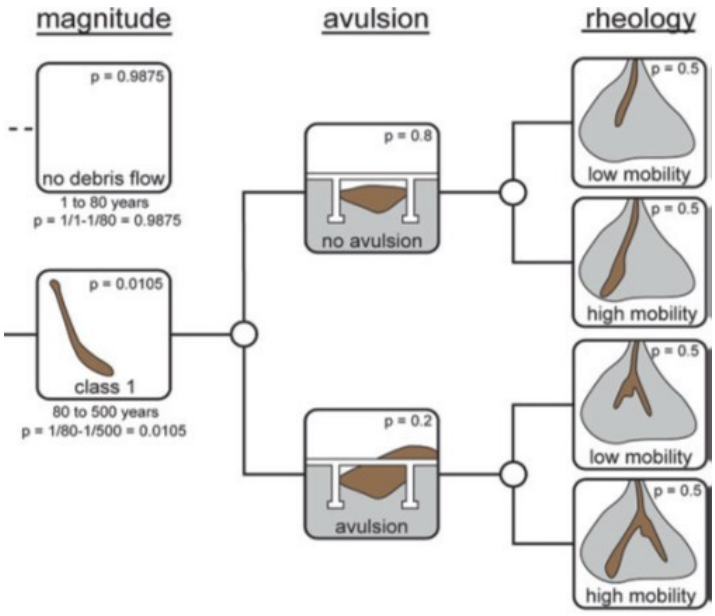

Figure 1.15: A hazard probability analysis with different scenarios adapted from Strouth et al. (2024) [33].

(C) Estimation of Debris flow Event Magnitude and Intensity: This is concurrent with the previous step and is expressed in terms of peak discharge and/or total volume of flow or area affected, depending on the objective of the hazard analysis and the available data. The probabilities of a range of event magnitudes and intensities are calculated as seen in Figure 1.16 [33].

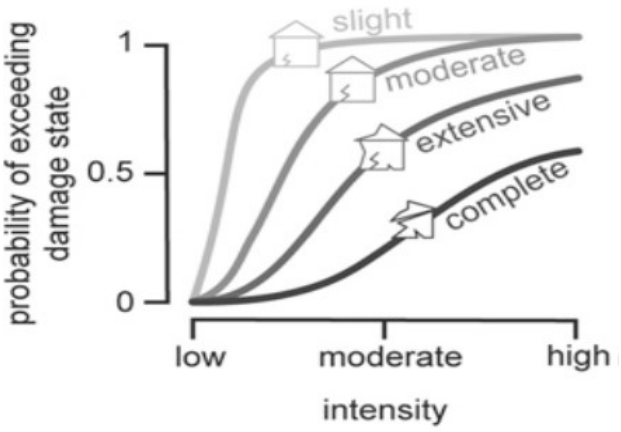

Figure 1.16: Results of a hazard intensity analysis with different scenarios courtesy Strouth et al. (2024) [33].

(D) Production Of Frequency-Magnitude Relationships: Deriving a relationship between the two previous steps in the form of Cumulative Frequency-Magnitude curves is necessary for estimating debris-flow magnitudes for any return period, which is useful in land use planning and structural design.

(E) Debris Flow Hazard Mapping: This is the final step in the hazard analysis of debris flows. Representing debris flow hazards on maps allows for effective communication of the hazard. The typical hazard

map uses three colours to classify the runout area risk as “High”, “Medium”, or “Low” risk depending on study-specific cutoff values as seen in Figure 1.17 [34].

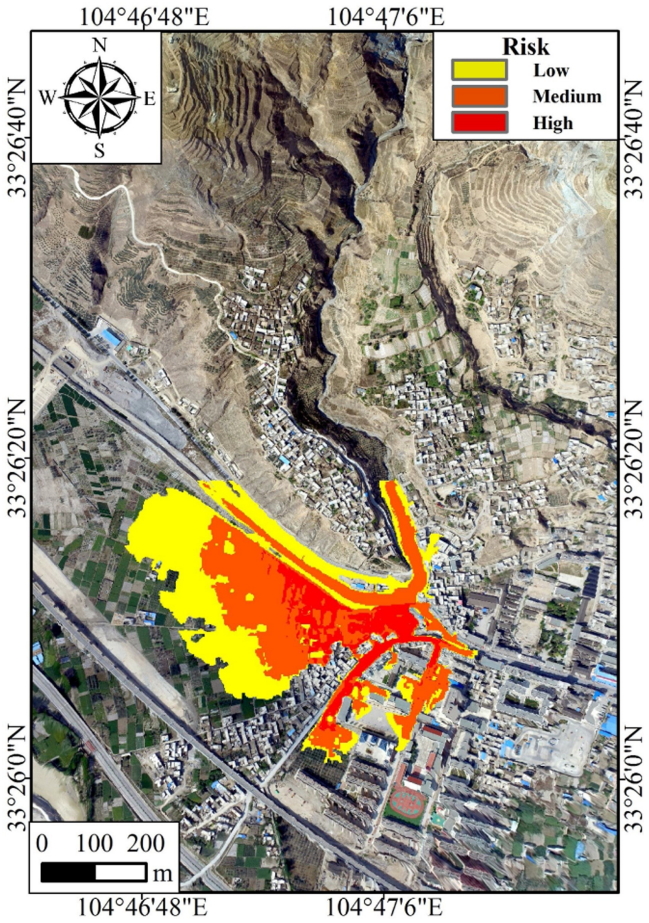

Figure 1.17: A typical debris flow hazard map with three hazard classes from Ouyang et al. (2019) [34].

1.3. Time-Resolved Triggering and Runout Analysis of Rainfall-Induced Shallow Landslides

1.3.1. Surging and its Significance

Flows generated by many shallow landslides are often distributed across multiple release areas, occur at different times, and converge to form a single large debris fan as per La Porta et al. (2023) [27]. A key aspect of such behaviour is the phenomenon of “surging” [27]. Hungr (2005) stated that debris flows typically move in separate, definite slugs of material or surges, broken up by a watery flow [16]. Surges vary from single digits to hundreds and may be separated by seconds to hours [16]. Surging can happen under different conditions outlined by Hungr (2005) as follows [16]: (a) When landslides are triggered at different times, i.e., non-simultaneously, (b) When sluggish flows periodically stall and then re-mobilise, (c) When turbulent fronts develop in otherwise laminar flow, this is seen in fine-grained flows, and (d) When longitudinal sorting of debris causes flow instability, a boulder front develops, which upon breaching causes a surge as seen in Figure 1.18 [16].

This study addresses the first cause, i.e., non-simultaneous triggering of landslides, by simulating debris flow surges of the Mocoa 2017 event that originated from multiple shallow landslides triggered in response to a four-day rainfall period.

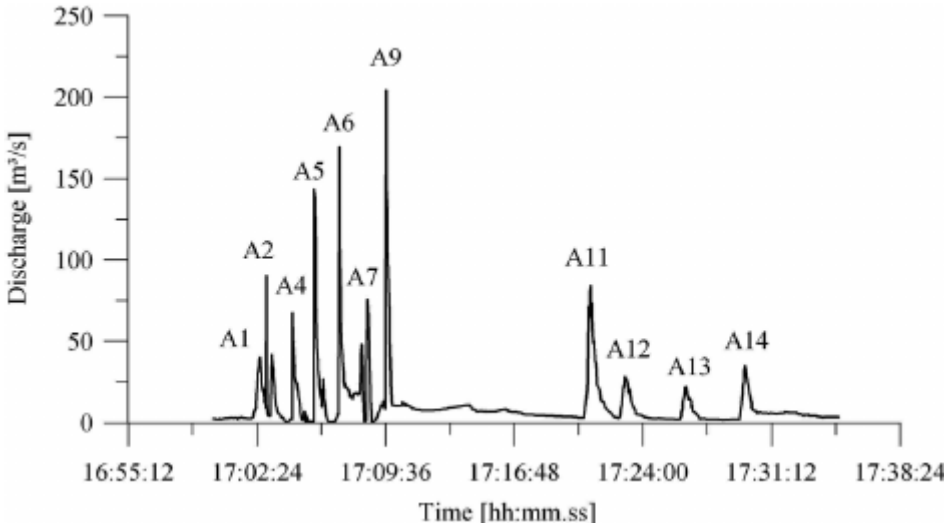

Figure 1.18: A hydrograph of the debris flow event in Pians, 2007 shows 14 surges as recorded by Araia et al. (2013) [35].

1.3.2. Influential Works

According to La Porta et al. (2023), conventionally, events that occur within the same basin and have overlapping runouts are considered as a single event for the purpose of analysis, while events in separate basins whose runouts do not overlap are considered individually [27]. This idealises the triggering of multiple landslides at different times across a basin into a single instantaneous event, thereby overlooking the effects of surging. Which can affect runout and flow height estimates [27]. Sequentially utilising landslide susceptibility and runout simulation models can separate shallow landslide events and the ensuing debris flow surges based on their location (spatial resolution) and initiation times (time resolution); this could improve runout analysis because it accounts for debris flow surges caused by non-simultaneous landslides as seen in Figure 1.19.

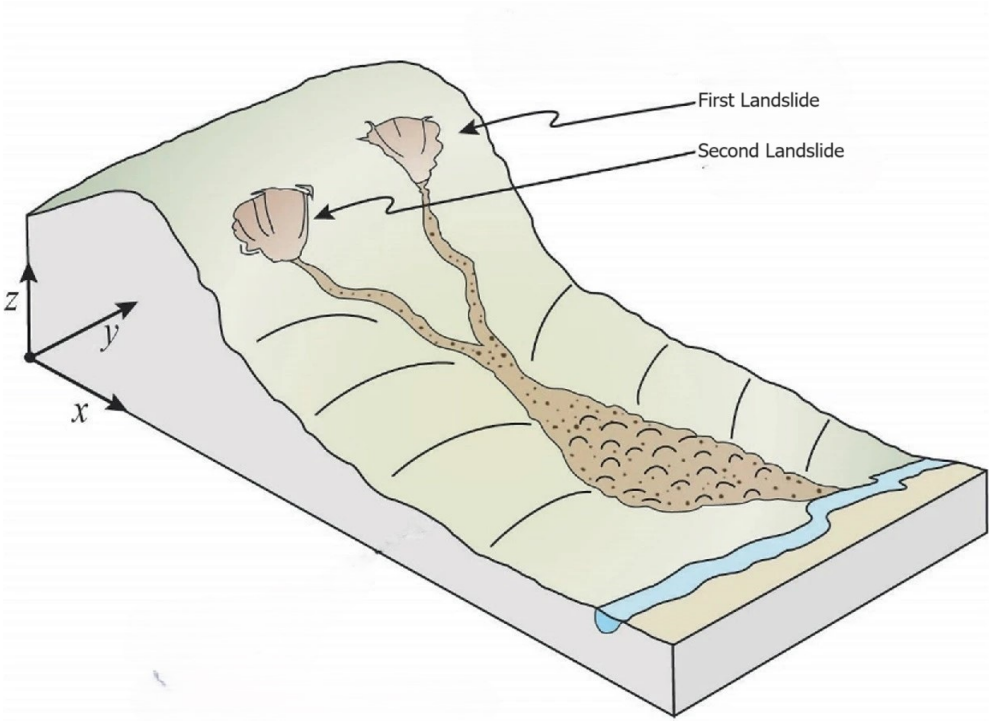

Figure 1.19: Two non-simultaneous landslides in the same basin with an overlapping runout adapted from Iverson et al. (2024) [36].

Stancanelli et al. (2017) applied the Transient Rainfall Infiltration and Grid-Based Regional Slope-Stability model (TRIGRS) and FLOW2D, a numerical runout model, to Giampilieri, 2009 a debris flow event in the town of Giampilieri, Italy [37]. Stancanelli et al. (2017) used TRIGRS to determine only the spatial resolution of the instabilities and used instantaneous releases when modelling the flow, thereby ignoring the non-simultaneous nature of the instabilities [37]. They found the conventional method to be more accurate than the spatially resolved method in producing the areal extent of the event. This result was in part due to the triggering parameters used, with Stancanelli et al. (2017) stating earlier in their text that "The limited knowledge of soil proprieties distribution is a problem common to many studies." (Stancanelli et al., 2017, p. 7) [37]. La Porta et al. (2023) used TRIGRS for the spatial and time resolution of instabilities with RASH3D, a numerical runout model for two events in Italian towns; Sarno, 1998 and Giampilieri, 2009 [27]. La Porta et al. (2023) found that the results of the conventional and time-resolved methods were similar for the Sarno event, as most of the instabilities were unrealistically triggered in the first time step. They achieved a more accurate runout for the times resolved approach when applied to the Giampilieri event as they had access to triggering analysis parameters calculated by Peres and Cancelliere (2016), which yielded a realistic distribution of the instabilities unlike at Sarno [27] [38]. The results of this method for the Giampilieri event are promising; however, the event contained a high number of landslides (600 shallow landslides), with much of the flow being channelised along narrow streets and affected by buildings and other minor topographical features. This lends greater than-normal importance to the surge sequence in arriving at a representative flow height [27]. The findings of both Stancanelli et al. (2017) and La Porta et al. (2023) highlight the importance of well-calibrated triggering parameters in analysing surges. Notably, Zhou et al. (2022) applied TRIGRS and Rapid Mass Movement Simulation (RAMMS), a numerical runout model, to the debris flow event in Dazhuang, China, 2013. They achieved a success rate of 81.86% for predicting the spatial distribution of landslides using TRIGRS and an overall accuracy of 76.77% in simulating a time-resolved debris flow compared to 78% for the conventional method, demonstrating good predictive ability; however, no improvement was seen for the time-resolved simulation compared to the conventional method [39]. The study is limited as the area of interest was small ($1.4km^2$) with a relatively short runout of approximately $800m$ through a rural area with a simple deposition zone, diminishing the relative importance of surging. However, it did benefit from extensive field investigations, which yielded reliable triggering parameters that enabled a parity of performance between the two methods.

Of the studies reviewed above, two of the three, Stancanelli et al. (2017) and La Porta et al. (2023), concerned events in Italy and the third, Zhou et al. (2022), did not explicitly consider surging. Therefore, there is limited precedent for comparing spatially and time-resolved debris flow runout analysis in developing countries, especially in South America. This study aims to see if the runout analysis of the Mocoa 2017 event can be improved by spatial and/or time resolution of events. For the spatial resolution of events, this study introduces a systematic procedure to subdivide the single basin of the study area into several sub-basins based on stream orders. The time resolution of events is analysed by using TRIGRS, which indicates the timing and area of slope instability or shallow landslide occurrence as a response to rainfall [40] [27]. The runout simulation model of choice varies from study to study, typically using depth-averaged numerical models; in this study, we use RAMMS, a two-dimensional depth-averaged numerical model. Further details of the tools employed in this study are in Chapter 2.1.

1.4. Case Study: Mocoa, 2017

Mocoa, Colombia, March 31st, 2017. Following four days of intense rainfall, a series of 420 mass movements occurred (see Figure 1.20), of which Sarmiento et al. (2019) classified 89% as flows, 10% as landslides, and 1% as rockfalls [2]. The multi-hazard Mocoa 2017 event was dominated by two major phenomena, i.e., a mud-flow along the Mulato River and a debris flow involving several other channels across the basin [2]. The mud-flow travelled within the banks of the Mulato River, only overflowing close to its confluence with the Mocoa River [2]. As a result, we can isolate the debris flow and its deposition, which caused most of the damage and is the sole concern of this study. Altogether, these mass movements devastated the area, causing between 25 and 100 million United States Dollars worth of economic damage [2]. Deaths numbered in excess of 300 people. The town's power substation was critically damaged, as were $1,462$ houses, leaving people without shelter, electricity, and running water [2].

Figure 1.20: An aerial view of a large landslide in Mocoa, courtesy Jaime Saldarriaga/Reuters via The I.B. Times [1].

1.4.1. Study Area Description

Situated in the southwest of Colombia. The town of Mocoa lies 604 meters above mean sea level (M.S.L.) in a valley of the Northern Andes Mountain range [41]. The eponymous river runs North-South on the Eastern edge of the town. Within the study area, its tributaries are the Sangoyaco and Mulato Rivers, which drain the highlands in the West and meet the Mocoa River in the East after passing through the town. The Taruca and Taruquita creeks, which also run West-East, converge to run South-South-East, meeting the Sangoyaco before it runs through the town as seen in Figure 1.21.

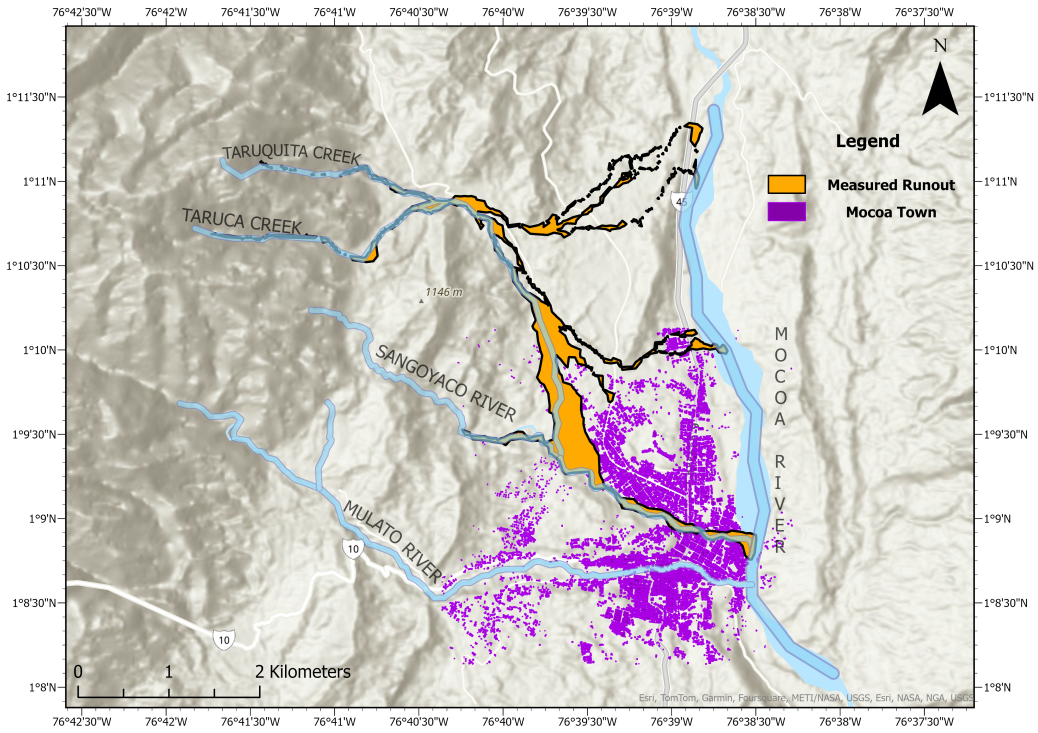

Figure 1.21: The Study Area ($75km^2$) with major rivers and creeks, as well as the measured debris flow runout, and the town of Mocoa in the South-West as represented by Google's Open Buildings dataset [42].

Within the Mocoa basin, the highlands (2300-$1100m$ above M.S.L.) in the West consist of Mocoa Monzo-granite, which contributed to 95% of the flow material, intruded by mafic dikes and sedimentary clasts, which made up the other 5% of the flow, as estimated by García-Delgado et al. (2019) [43]. The granite allows for very steep slopes (between 50° to 75°) in the upper zone with deep V-shaped valleys [2]. The intermediate zone ($1100 - 800m$ above M.S.L.) contains the Orito, Pepino, and Rumiyaco formations, mainly composed of reddish mudstones, sandstones, and grey mudstones, respectively [43] [2]. The lower part of the basin (sub $800m$ above M.S.L.) has thick quaternary alluvial deposits from a debris flow in 1962 covering Rumiyaco and the Villeta (marine fine-grained and calcareous rocks) formation [43] [2]. The area typically experiences a rainy season between April and August with a Monthly Multi-Annual Precipitation (M.M.A.) > $300mm$ and a dry season from October to February (M.M.A. $< 250mm$) [43].

1.4.2. Event Summary

According to Sarmiento et al. (2019), Two weeks of little to no precipitation was followed by four days of intense rainfall ($214.8mm$). This intense rainfall triggered mass movements across the basin [2]. With rainfall a day before the event accounting for $130mm$ alone [2]. Cheng et al. (2018) explain that the precipitation sequence resulted from larger climatic phenomena [9]. An El Niño from 2014 to 2016 decreased precipitation in the area, which reduced vegetation coverage, thereby diminishing the area's rainfall interception and water holding capacity, increasing the susceptibility to erosion and mass wasting [9]. A La Niña in 2017 allowed for higher rainfall, saturating the basin, effectively paving the way for the ensuing disaster [9] [2]. On March 31, 2017, a debris flow was triggered across the basin. According to Sarmiento et al. (2019), The debris flows transited independently through the Taruquita and Taruca Creeks, merging at their confluence, after which a minor portion went along the San Antonio Avulsion with the majority of the flow heading downstream towards the junction with the Sangoyaco River meeting another flow developed along the Sangoyaco River, eroding, entraining and depositing material along the way. Thereafter, the flow followed the Sangoyago river bed and passed destructively through the town, finally discharging into the Mocoa River, see Figure 1.21 [2]. The particle size distributions of deposits in the urban area were well-graded, ranging from clay to sandy material [2]. Rounded boulders with an estimated average diameter of $2.0m$ were found near the northern part of the town [2].

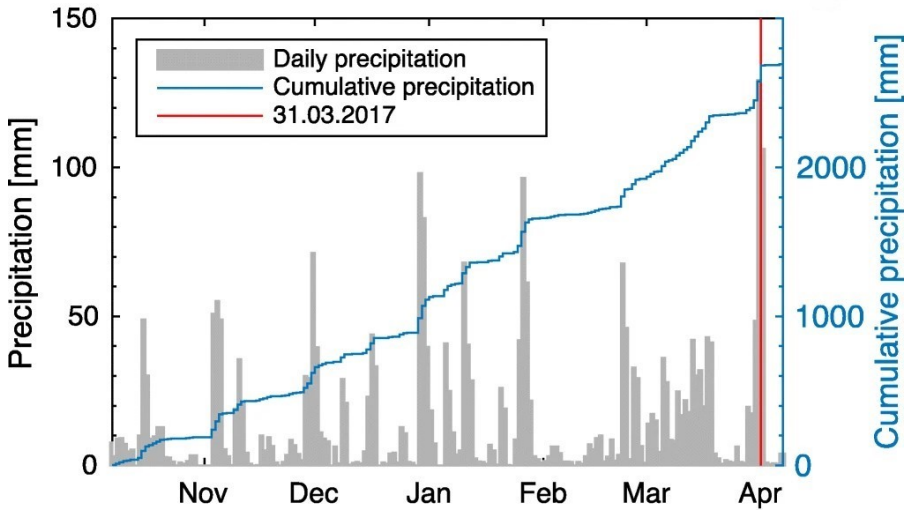

Figure 1.22: Daily rainfall in the Mocoa drainage basin for six months up to the 2017 event, adapted from Sarmiento et al. (2019) [2].

Figure 1.23: Multiple shallow landslides in the middle and upper part of the Taruca micro-basin courtesy Corpoamazonia via Mongabay [44].

Figure 1.24: An aerial view of the debris fan with the creeks and landmarks labelled and the destroyed Junín Power Substation (J.P.S.) in the distance, courtesy Jorge Castro in Garcia-Delgado et al. (2019) [43].

A total landslide volume of about $3.44 \times 10^6 m^3$ of material was calculated by García-Delgado et al. (2019), of which almost 10% or about $298,000 m^3$ mobilised into a debris flow with an average velocity of $8 - 12 m/s$ [43] [2]. Erosion and entrainment contributed to a total debris flow volume of around $2.6 \times 10^6 m^3$ [43]. The Colombian Geological Service (S.G.C.) classified the Mocoa Debris Flow event as a Class 5 Debris Flow on the scale proposed by Jakob (2005a) seen in Table 1.3 and Table 1.4 [45] [17]. A Class 5 debris flow has a volume in the order of volume of between $10^5 - 10^6 m^3$ and a peak discharge between $1,500 - 12,000 m^3/s$ while causing partial destruction of towns, infrastructure and bridges as well as obstruction of streams and small rivers as is consistent with the Mocoa 2017 event [45] [17]. The Mocoa event has been thoroughly studied by conventional approaches, most notably by Reyes et al. (2018) and S.G.C. (2018), making it an excellent case to be examined by an alternative approach [46] [45].

1.5. Conclusion

It is reasonable to question if events occurring in basins with multiple long runouts could benefit from greater spatial and time resolution. Prakash et al. (2024) have found that compared to other mass movements, debris flows are more likely to cause high fatality events due to their long runout distance and poor predictability, thereby posing a high risk to society [47]. Dowling and Santi (2013) have shown that developing countries, particularly those in South America and Asia, have more severe debris-flow disasters compared to other countries [23]. Debris flow susceptibility is related to an area's geological, geomorphological, and climatic conditions. The Mocoa study area is typical of towns within the inter-tropical zones of the Andean-Amazonian Piedmont [2]. This is why many people stand to benefit from the improvement of debris flow runout analysis. By spatially and time resolving shallow landslides and the ensuing debris flow of the Mocoa, 2017 event, we aim to analyse the often overlooked phenomenon of debris flow surging caused by non-simultaneous landslides and its effect on runout analysis in Mocoa, Colombia [23] [47].

2

Research Questions and Methodology

2.1. Research Questions

Section 1.3 defines debris flow surging and exposes the research gap which is to be addressed by the main research question, which is as follows;

1. ***Does accounting for debris flow surging caused by non-simultaneous landslides improve the accuracy of runout analysis in the Mocoa, 2017 event?***

   Sub-Research questions are as follows:

   (a) How does the spatial resolution of debris flow source areas affect the accuracy of the runout simulation?

   This question arises from the need to investigate the effects of dividing the source area into smaller source areas and to identify the spatial resolution that provides the best results.

   (b) Is it feasible to utilise the landslide inventory for the exact location of shallow landslides to simulate the runout?

   This question arises from the need to see if the most straightforward and possibly accurate method of spatial resolution of events will work, that is, using the exact location of mapped landslides for initiating the debris flow.

   (c) Is it adequate to consider only the highland region as a source area for accurate runout simulation?

   This question arises because the highland area accounts for roughly 80% of the debris flow volume and is similar to the area considered by other researchers in their analysis of the Mocoa event [48] [46].

   (d) Does the deposition between debris flow surges significantly affect the simulated runout?

   Each debris flow surge leaves behind a deposit, which could influence succeeding surges, thereby possibly modifying the simulated runout. The final sub-research question of this study aims to determine the extent to which surge depositions affect the predicted runout.

2.2. Methodology

First, the landslide inventory is analysed in Section 2.4 to assess the scale of the event. This is followed by a method to spatially resolve the study area and an assessment of the instabilities generated by the preceding rainfall using a process-based landslide susceptibility model in Section 2.5. Next, using a numerical runout simulation model, a spatially resolved analysis of the debris flow events is conducted in Section 3.2 followed by the modelling of debris flow surges in Section 3.3.1 and lastly, a time-resolved analysis in Section 3.3. After the analyses, the Performance Assessment Criteria seen in Section 2.8

are calculated and presented in Chapter 4 as the results of this study, along with answers to the research question in Section 4.4 a discussion of the limitations of this study follows in Section 4.5. Finally, a conclusion is arrived at in Chapter 5.

Surging is accounted for by sequentially utilizing a landslide susceptibility model known as Transient Rainfall Infiltration and Grid-Based Regional Slope-Stability Model (TRIGRS), which is introduced in Section 2.6 and a runout simulation model known as RAMMS (RApid Mass Movement Simulation) is used to separate shallow landslide events, that develop into debris flows, based on their location and time of initiation. RAMMS is introduced in Section 2.3. To systematically answer the research and sub-research questions, eleven scenarios have been devised in Section 2.7. All pre-processing and post-processing of data was carried out in a geographical information system (ArcGis). This study defines the term ”spatially resolved” as the process of dividing the study area into smaller source areas and ”spatial resolution” as the degree to which the source area has been divided into smaller source areas or has been spatially resolved. An outline of the methodology is shown in Figure 2.1

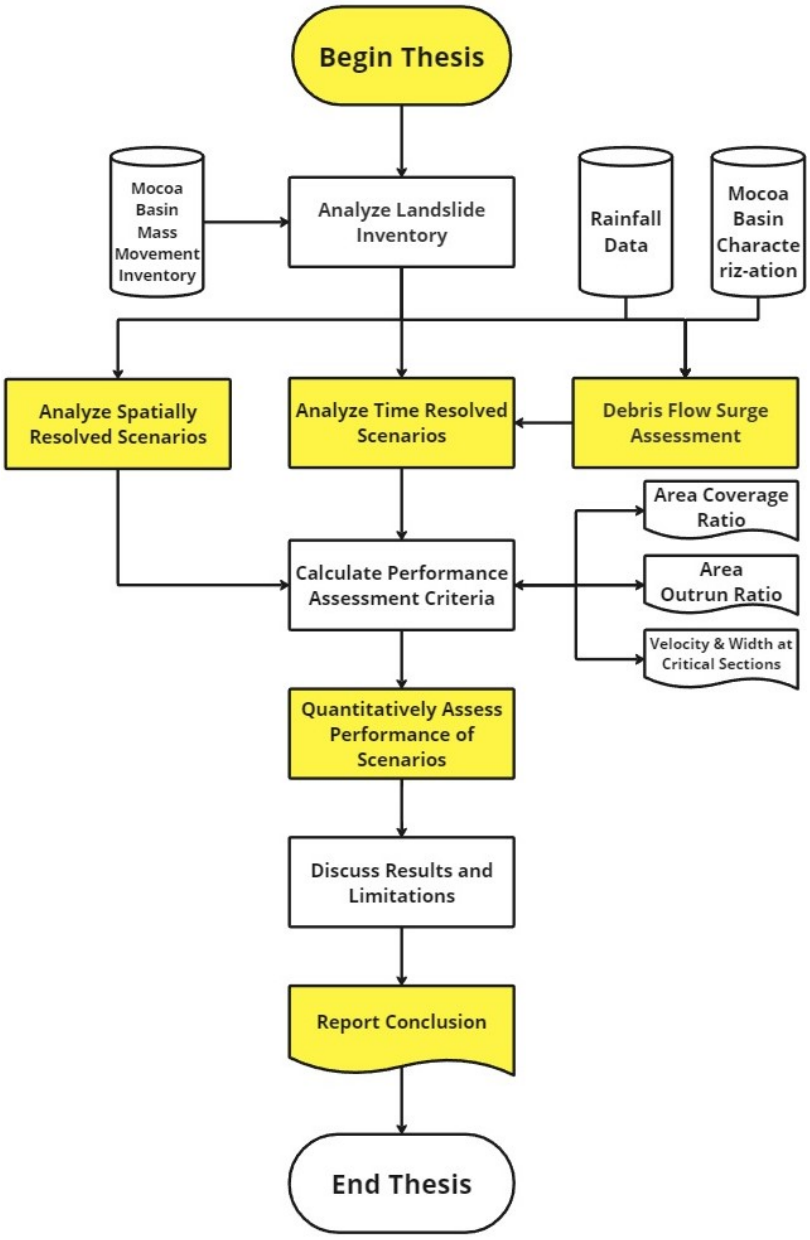

Figure 2.1: The methodology of this thesis.

2.3. Rapid Mass Movement Simulation (RAMMS)

2.3.1. Introduction

RAMMS (RApid Mass Movement Simulation) is a two-dimensional depth-averaged numerical model capable of simulating debris flow heights and slope-parallel velocities from initiation to final deposition in three-dimensional terrain [49]. RAMMS was validated at full-scale test sites such as Vallée de la Sionne and Illgraben, Switzerland [49] [50]. RAMMS facilitates the selection of multiple release areas with sequential activation and modifies the topography to account for each event [51].

2.3.2. Model Assumptions

Depth-averaged equations underlie the model, and the following general assumptions are made [52] [53] [54]:

1. The characteristic flow height and characteristic length scale are such that their ratio is small (H/L«1) as seen in Figure 2.2 [55].

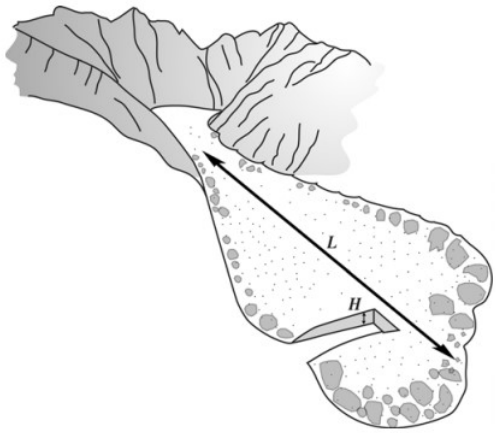

Figure 2.2: The relationship between the flow height ”H” and ”L” the flow length from Iverson (2005) [56].

2. The granular material that makes up the landslide is considered to be a single-phase, in-compressible homogeneous continuum that approximates the bulk behaviour of the real material.
3. The bed is impervious. The bed friction angle is constant and independent of the shear rate and solid concentration. A kinematic boundary condition is imposed on free and bed surfaces.
4. The depth-averaged stream-wise velocity is close to the actual velocity everywhere except at the very base. Shear stress is assumed to be linearly distributed over the depth and satisfies the basal and free surface boundary conditions.
5. The flowing mass slides on a thin basal layer. Shearing, fluidization, and significant density variations are confined to the thin basal layer, so a constant depth-averaged value for the density is used with minimal loss of accuracy.
6. Changes in bulk density have a small effect (less than a few per cent) on the convective terms in the equations of motion. Consequently, bulk density is assumed to be constant.
7. Active or passive stress is developed when an element dilates or contracts, respectively, in the direction parallel to the bed.

2.3.3. Working Principle

The RAMMS model assumes a fixed Eulerian 3D coordinate system in z (x, y). Flow is unsteady, non-uniform, and characterized by flow height H (x, y, t) with a mean velocity U (x, y, t) at time t [57]. The mass balance equation described by Christen et al. (2010) is [55]:

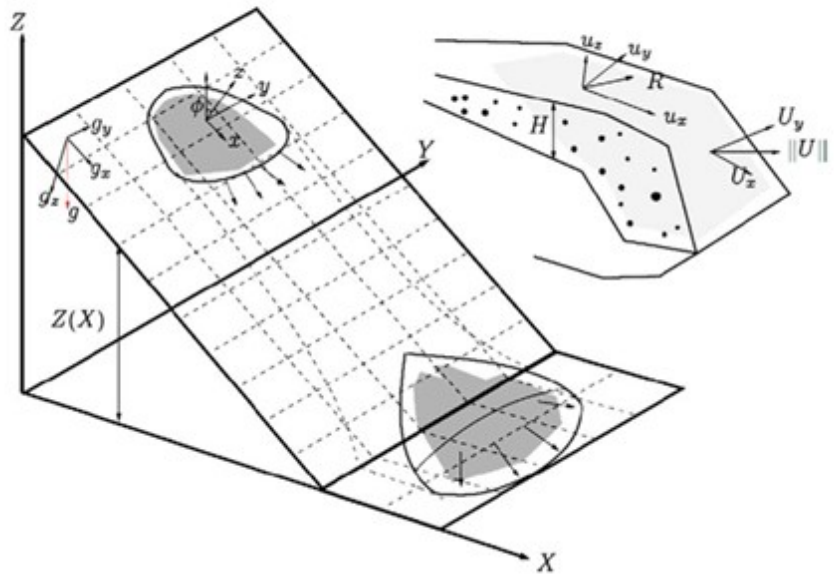

Figure 2.3: Cartesian framework topography of the RAMMS model adopted from Christen et al. (2010) [55].

$$\underbrace{\partial_t H}_{\substack{\text{rate of change}\\ \text{of flow height}}} + \underbrace{\partial_x (HU_x)}_{\substack{\text{rate of change}\\ \text{of momentum (X)}}} + \underbrace{\partial_y \Big(HU_y \Big)}_{\substack{\text{rate of change}\\ \text{of momentum (Y)}}} = \underbrace{\dot{Q}(x,y,t)}_{\substack{\text{mass production}\\ \text{source term}}} \tag{2.1}$$

The depth-averaged momentum balance equation described by Christen et al. (2010) is [55]:

$$\underbrace{\partial_t (HU_x)}_{\substack{\text{local rate of}\\ \text{change of momentum}}} \underbrace{+ \partial_x \left(c_x H U_x^2 + g_z k_{a/p} \frac{H^2}{2} \right)}_{\substack{\text{convective}\\ \text{acceleration}}} + \underbrace{\partial_y \left(HU_x U_y \right)}_{\substack{\text{advective}\\ \text{acceleration}}} = \underbrace{S_{gx}}_{\substack{\text{driving gravitational}\\ \text{acceleration}}} - \underbrace{S_{gx}}_{\substack{\text{frictional}\\ \text{deceleration}}} \tag{2.2}$$

A similar equation exists in the Y-direction. The velocity profile shape factors "c_x" and "c_y" account for shear gradients and non-rectangular velocity profiles. However, Christen et al. (2010) have found that their influence on realistic velocity profiles is insignificant and recommend them to be set to unity. i.e.; c_x = c_y = 1 [55]. The vertical and horizontal normal stresses are proportionally related by an earth pressure coefficient $k_{a/p}$ [55].

$$k_{a/p} = tan^2 \left[45° \mp \frac{\phi}{2} \right] \tag{2.3}$$

Where ϕ is the internal friction angle. Active (a) refers to dilatant flow regions, and passive (p) refers to compressive regions. Christen et al. (2010) recommend $k_{a/p}$ = 1 as it was found to be insignificant to the final calculated runout distances and velocities [55].

Finite Volume Method

RAMMS applies a Total Variation Diminishing (TVD) Finite Volume Scheme (FVM) on three-dimensional terrain [57]. According to Christen et al. (2010), RAMMS constructs a numerical mesh in the following manner: For each debris flow simulation, a domain is specified such that no interaction takes place between the flow and boundary [55]. A finite volume quadrilateral surface mesh is constructed by discretizing the domain in the X-Y plane using a Cartesian mesh [55]. The corresponding surface elevation is calculated by bi-linear interpolation of the four nearest grid points from the original Digital

Elevation Model (D.E.M.) [55]. Thereby resampling a coarse D.E.M. into a fine computational mesh [55]. RAMMS implements a HLLE–Heun numerical scheme to solve the governing equations [55]. Harten-Lax-van Leer-Einfeldt (HLLE) is a type of approximate Riemann solver used in computational fluid dynamics [55]. While Heun's method is an extension of the Euler method into a two-stage second-order Runge–Kutta method [55]. Losses in runout volume due to the approximations made by this method are given in Table 3.1.

2.3.4. Rheology

RAMMS implements an extended Voellmy Salm model to describe the rheology of the flowing debris. The flow dynamics are primarily influenced by the net effective acceleration [55]. The standard Voellmy equation is [55];

$$\underbrace{S_i}_{\substack{\text{net effective acceleration}\\ \text{in x and y directions}}} = \underbrace{hg_i}_{\substack{\text{driving gravitational}\\ \text{acceleration}}} \underbrace{- \frac{u_i}{\|\mathbf{u}\|}\left(h\mu g_z + \frac{g}{\xi}\mathbf{u}^2\right)}_{\substack{\text{frictional}\\ \text{deceleration}}} \tag{2.4}$$

The Voellmy rheology model is based on the Coulomb friction (μ) and the velocity squared dependent turbulent friction (ξ) terms. The Coulomb friction (μ) governs flow mobility as the slope angle ϕ at which the flow halts is given by [49],

$$\mu = \tan\phi \tag{2.5}$$

Typically μ ranges between 0.05 and 0.4 for debris flows [49]. The turbulent friction (ξ) term governs the peak flow velocity and the rate of deceleration [58]. An increase in ξ increases deceleration [58]. Khan et al. (2021) found that ξ varies with the sediment concentration of the fluid [59]. For granular flow, ξ ranges between $100 - 200 m/s^2$ [49]. Typical values of ξ and μ are shown in Figure 2.4.

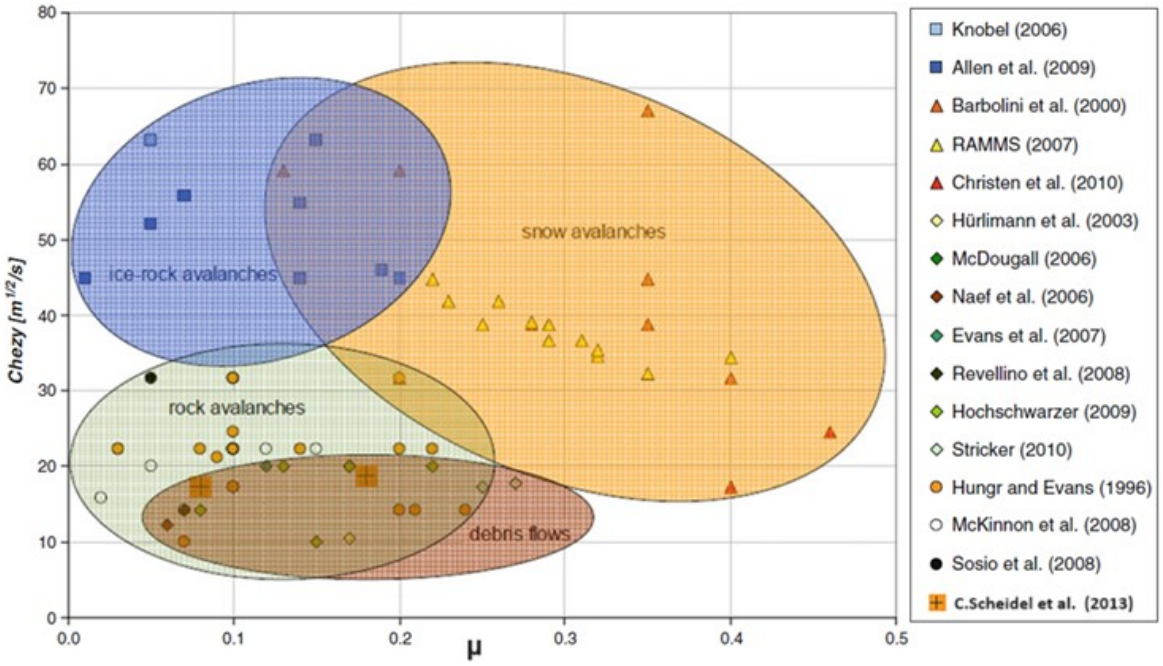

Figure 2.4: The range of values of μ and Chezy's coefficient (C), where ξ = C^2 for the forensic analysis of different mass movements including debris flows using Voellmy rheology adapted from C. Scheidel et al. (2013) in C. Margottini et al. (2013) [60].

The effect of curvature on the driving forces is included in the modifications proposed by Fischer et al. (2012) [61]. Fischer et al. (2012) introduce "f", a centrifugal acceleration term that is both a function of the flow velocity (u) and terrain curvature represented by the matrix "K" in all directions [61]. Where;

$$f = uKu^T \tag{2.6}$$

The centrifugal force F follows as;

$$F = \rho h f \tag{2.7}$$

Where ”h” is flow height [61]. The Voellmy Salm friction in the i-direction (S_i) includes the turbulence coefficient (R_ξ) and the curvature dependent friction coefficient (R_t) and is formulated as [61]:

$$S_i = hg_i - \frac{u_i}{\|\mathbf{u}\|}\left(h\mu g_z + R_t\mathbf{u}^2 + R_\xi\mathbf{u}^2\right) \tag{2.8}$$

Where ,

$$R_t = \mu h\frac{\mathbf{u}^T\mathbf{K}\mathbf{u}}{\mathbf{u}^2} \tag{2.9}$$

and

$$R_\xi = \frac{g}{\xi} \tag{2.10}$$

This model is calibrated by forensically analysing well-documented historical events and determining the best-fit parameter sets [49]. Velocity and runout distances are important factors to characterize the debris flow and to simulate its impact on the infrastructure [59].

2.3.5. Limitations

In reality, debris flows are not a homogeneous single-phase continuum; instead, they are characterised by strong interactions of the solid and liquid constituents [20]. The degree and nature of the solid-liquid interaction varies from flow to flow but always plays a definitive mechanical role [20]. Single-phase debris-flow models do not account for the interactions between the solid and fluid constituents, thereby neglecting the evolution of flow bulk density, resistance and velocity [36].

Figure 2.5: A view of the solid-liquid constituents of a debris flow showing the percentage of solids concentration ϕ_s adapted from Meyrat et al. (2024) [62].

To justify the implementation of the Voellmy model in this study. We refer the reader to Bartelt et al. (1999), where a comprehensive argument, for and against, applying Voellmy rheology to mass movement analysis is made [63]. They highlight the flaws, phenomenological and simplistic nature of the model, its advantages, commonality with other rheological models, proven assumption of plug flow, and its basis on real mass movement behaviour [63]. Bartelt et al. (1999) conclude their argument by recommending the Voellmy-fluid model, despite its shortcomings, for use in real-world mass movements until a more sophisticated model is developed [63]. This argument was made a quarter of a century ago. The Voellmy model continues to be used in most numerical models, as shown in Dash et al. (2021) [64]. Furthermore, the Voellmy parameters have been calibrated for Mocoa in a dedicated study by Correa (2023) [48].

2.3.6. Conclusion

The RAMMS model is a popular debris flow simulation tool validated by field tests to accurately simulate debris flow runout [58] [57]. The model inputs and their sensitivities are thoroughly studied in various literature, justifying their use in this study [65] [66] [67].

2.3.7. RAMMS General Input

The RAMMS input listed in Table 2.1 is common across all debris flow simulations, other simulation specific inputs are specified during the analysis.

Table 2.1: RAMMS General Input.

Input	Value	Source
D.E.M.	$12.5\,\mathrm{m}$	ALOS PALSAR [68]
μ	0.07	Correa (2023) [48]
ξ	$100\,\mathrm{m/s^2}$	Correa (2023) [48]
Flow Density	$2,000\,\mathrm{kg/m^3}$	Mean of typical values that range from $1,600$ to $2,400 kg/m^3$ [21]

The parameters μ and ξ were obtained from Correa (2023). Further calibration is beyond the scope of this study. The $12.5m$ Digital Elevation Model (D.E.M.) is the lowest resolution pre-event D.E.M. covering the study area that is freely available, hence its use in this study. The D.E.M. was then hydrologically conditioned to correct inaccuracies as per Environmental Systems Research Institute, Inc. (Esri) guidelines [69]. As part of this procedure, two significant modifications were made, as seen in Figure 2.6: (a) A stream was added or burnt into the D.E.M. to represent the confluence of the Taruca and Taruquita near the centre of the study area. (b) Two areas were fenced to represent the thick vegetation and slope not captured by the D.E.M.

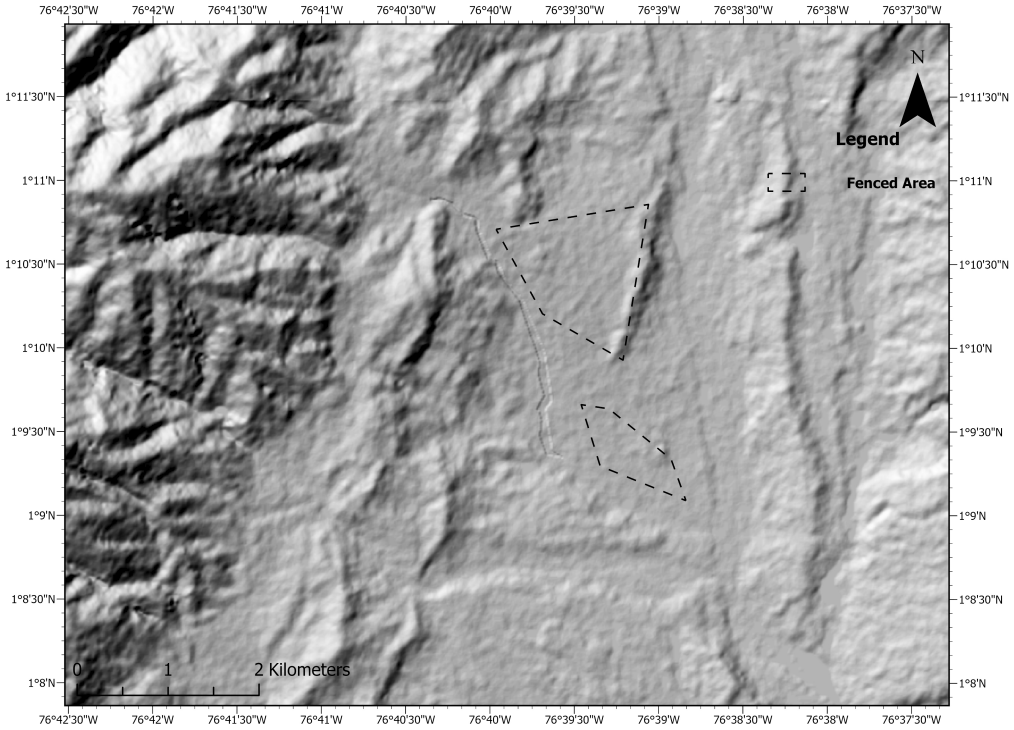

Figure 2.6: Modifications made to the D.E.M. The dashed line indicates the region bounded by the fenced area, while the stream can be seen to the line's immediate left in the centre of the map.

The stream was added by lowering the elevation along the stream path, as represented by satellite imagery. In this case, the reduction in elevation required was $9m$ this value was arrived at by iteration starting from $0.5m$ in steps of $0.5m$ and mapping the stream network in the same manner as in Figure 2.9 to verify that the stream is present as in reality. The fenced area was created by raising the elevation by $30m$ along the perimeter to prevent the debris flow from traversing the area; this increase in elevation was again obtained by iterations starting from $1m$ and progressively increasing it to the minimum required elevation. According to Esri guidelines, when hydrologically conditioning a D.E.M., the actual elevation is not important. Instead, the resulting flow pattern should match with reality or the expected flow over the terrain [69].

2.4. Landslide Inventory Analysis

The landslide inventory was compiled by the Colombian Geological Service (SGC) [45]. Figure 2.7 exhibits the 273 shallow landslides that contributed to the Mocoa Debris Flow event.

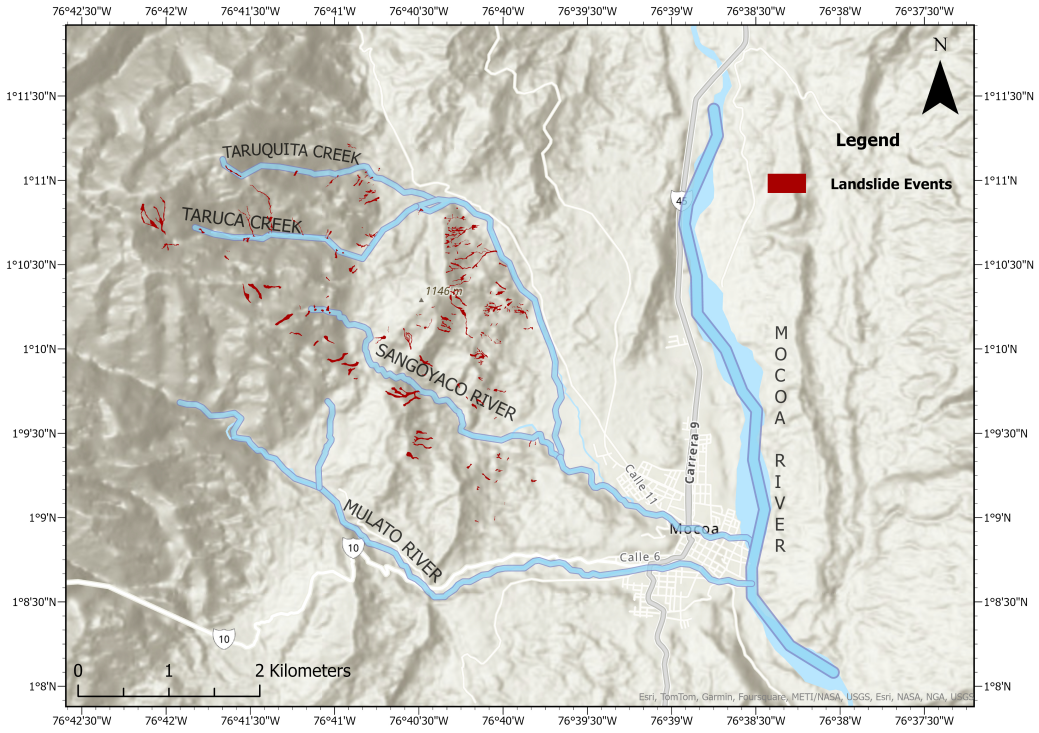

Figure 2.7: The study area with landslides that contributed to the Mocoa Debris Flow event along with the major rivers and creeks.

Individual landslide volumes vary, with the largest being $13,275m^3$ and the smallest being $15m^3$. The median volume of all the landslides is $325m^3$, as seen in Figure 2.8. Altogether these landslides contributed $297,143m^3$ of material to the debris flow. A total debris flow volume of around $2.6 \times 10^6 m^3$, as calculated by Garcia-Delgado et al. (2019), implies a volume of $2.3 \times 10^6 m^3$ was due to erosion and entrainment of debris [43].

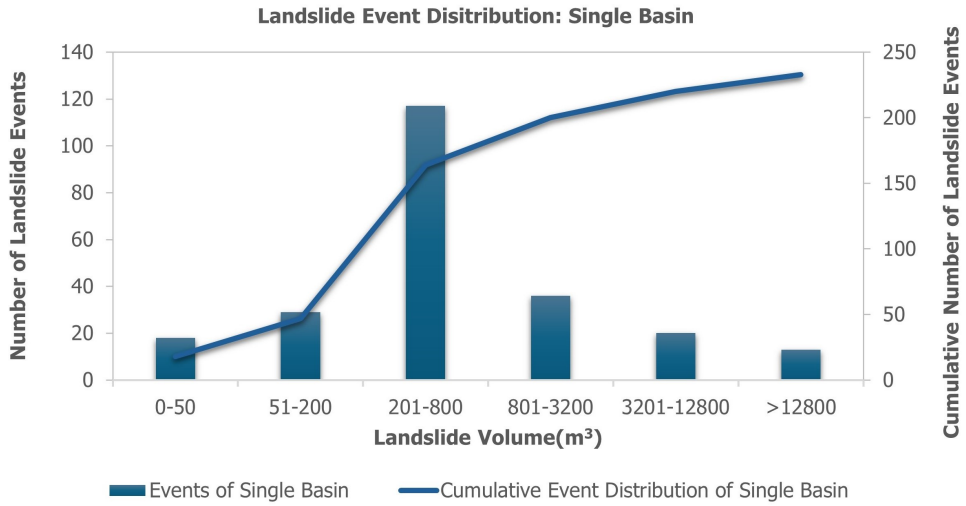

Figure 2.8: The number of landslide events for a range of volumes as well as the cumulative number of events in the study area as seen in Scenarios 1 and 3.

The ratio of landslide volume to total debris flow volume is 8.75. This multiplication factor was used with the landslide volumes later in the analysis to account for erosion and entrainment when modelling the debris flow. Volumes obtained using this ratio are termed 'modelled volume'. The ratio of the entrained volume to the landslide volume is 7.75 which is marginally higher than the figure of 7.5 calculated by Sarmiento et al. (2019). This difference (0.25) is because Sarmiento et al. (2019) included the mud flow along the Mulato River in their calculations, but this study does not, as it focuses on the debris flow. Sarmiento et al. (2019) state that the Mulato Basin produced five times less solid material than the Taruca Basin, so it is appropriate that their ratio of entrained volume to landslide volume is lower than what this study calculates [2]. By accounting for erosion and entertainment in such a manner, we ensure that the volume of flow modelled is consistent with that of the actual debris flow event.

2.5. Demarcating Sub Basins

The procedural demarcation of watersheds introduces a method to resolve the study area into basins and sub-basins for convenient analysis. Watershed morphometry heavily influences debris flow volume and frequency [70]. Hungr (2005) states that debris flows are typically confined to basins arising from gullies up to second-order streams, as they possess steep slopes $(25 - 45^o)$, which favours debris flow initiation [16]. Furthermore, Hungr (2005) asserts that "…it is prudent to consider multiple triggers, involving several tributaries of a given basin" (Hungr, 2005, p.17) [16]. In the demarcation of sub-basins, tributaries are given due consideration by basing the sub-division of basins on stream orders. To begin, we determine the single basin of interest within the study area. The process of delineating a basin is as follows: Firstly, a flow direction raster is calculated by implementing the D8 algorithm. This algorithm assigns flow direction for each cell to its steepest down-slope neighbour in one of eight directions [71] [72] [73]. A flow accumulation raster is calculated by determining the accumulated flow in each cell, which is the number of cells that flow into it [74]. Areas of high accumulation flow usually indicate stream channels, while areas of zero accumulation are typically ridges [74] [75]. In this way, major rivers and creeks were identified in the study area. The rivers and creeks were then hierarchized. There exist two common algorithms for this purpose. The Strahler and the Shreve algorithms. The Shreve algorithm was found to produce thirty-two stream orders, resulting in many sub-basins that were too small to encapsulate landslide areas, so the Shreve method was disregarded. Unlike the Shreve algorithm, the Strahler algorithm only increases stream orders when two streams of the same order intersect; otherwise, it continues with the order of the highest intersecting stream [76] [77]. This made the Strahler method more suitable for our analysis as it allows the creation of conveniently sized sub-basins, thus enabling spatial resolution with only four stream orders for the entire area, as seen in Figure 2.9. The Mocoa River, as the mainstem, was ordered fourth, with its tributaries ranking third, the tributary relevant to this study being the Sangoyaco River after its confluence with the Taruca-

Taruquita, and sub-tributaries, namely the Sangoyaco and Taruca-Taruquita ranked second. Closer to their origins, the Sangoyaco, Taruca, and Taruquita were ranked as first-order streams. Figure 2.10 shows the linearised network described above. Each point in the diagram represents a major pour point, some of which are used to demarcate sub-basins, with the lines representing streams of interest. A pour point or watershed outlet point is the lowest point along a watershed boundary and, consequently, a point of highest accumulation flow [78]. In the first stage, a single Basin of $11.3km^2$ was created by considering the confluence of the Sangoyaco and Taruca-Taruquita; in other words, all third-ordered streams in the system, as seen in Figure 2.11. The landslide distribution remains the same as seen in Figure 2.8. The spatial resolution is then improved by considering all second-order streams in addition to the first order, thereby demarcating four sub-basins as seen in Figure 2.13. The distribution of landslide volumes across the four sub-basins is seen in Figure 2.12. Sub Basins 2 and 3 contain more than half the total landslides, while Sub Basin 1 contains landslides across all the size classes. Sub Basin 4 is mostly populated by landslides smaller than $800m^3$. Finally, seven sub-basins were demarcated by considering all stream orders and an additional point along the Taruca to account for the very large landslides in Sub Basin 1 as seen in Figure 2.15. The distribution of landslide volumes across the seven sub-basins is seen in Figure 2.14. Sub Basin 4 and 6 contain the majority of landslides, with Sub Basin 1 containing very large landslides ($> 12800m^3$). Sub Basin 3 contains few but large landslides (3200-$12800m^3$).

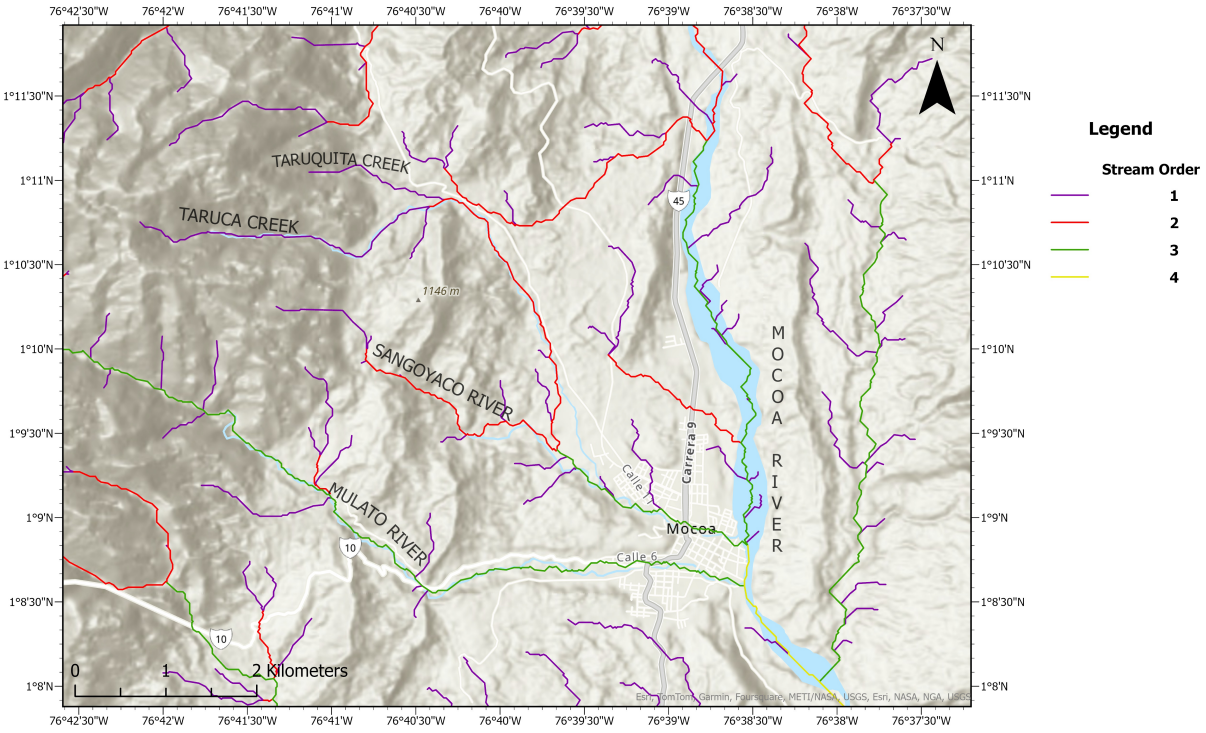

Figure 2.9: The stream network as produced by the Strahler Algorithm.

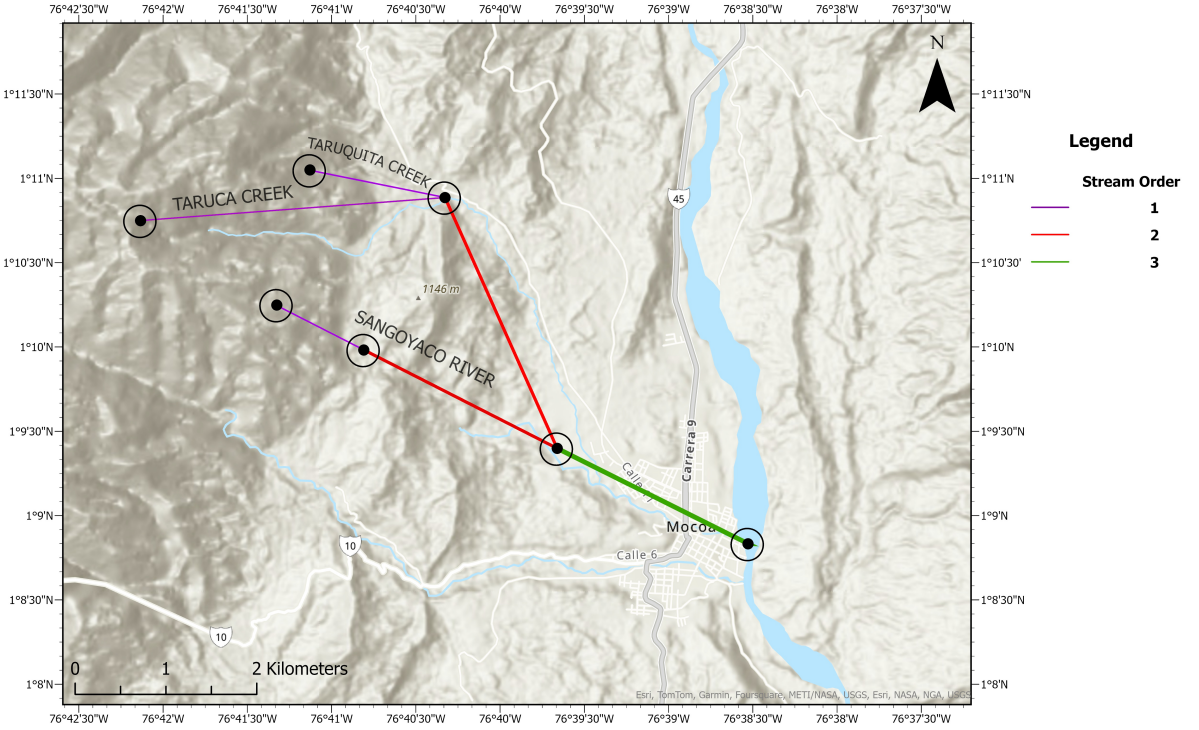

Figure 2.10: The linearised stream network order.

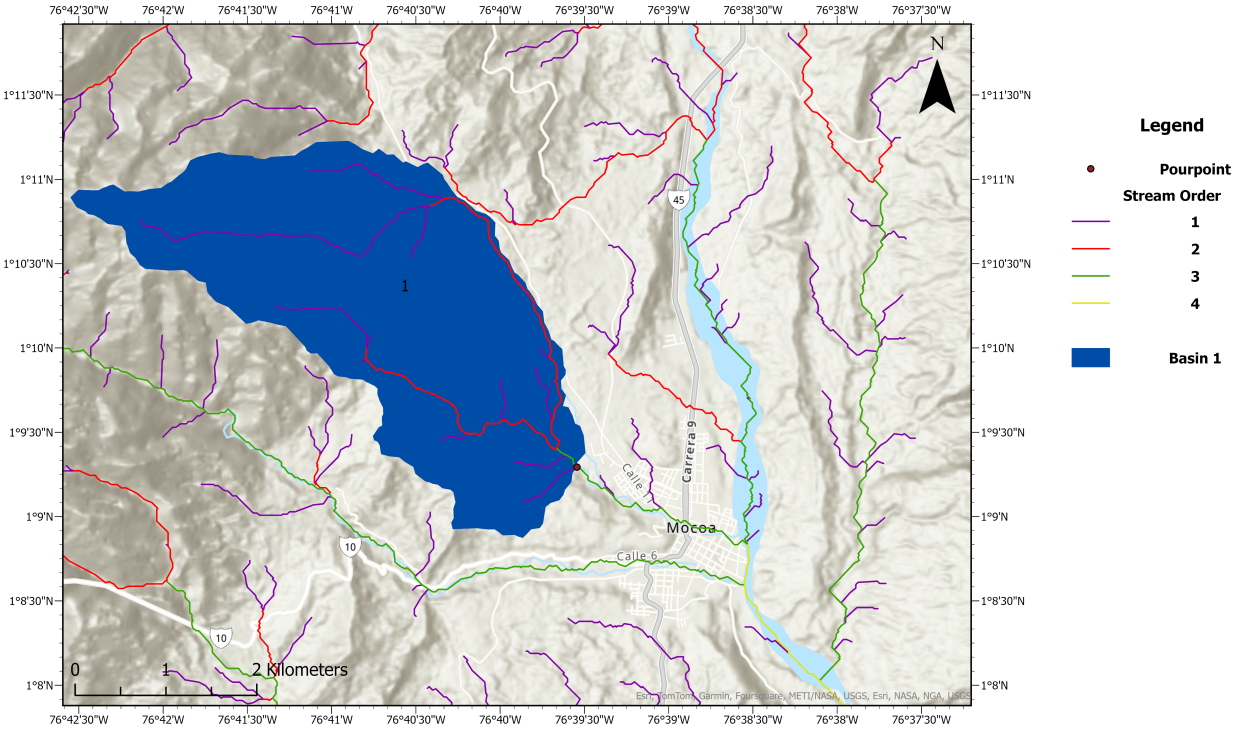

Figure 2.11: The single basin formed when considering the third order stream. This basin is used in Scenario 3.

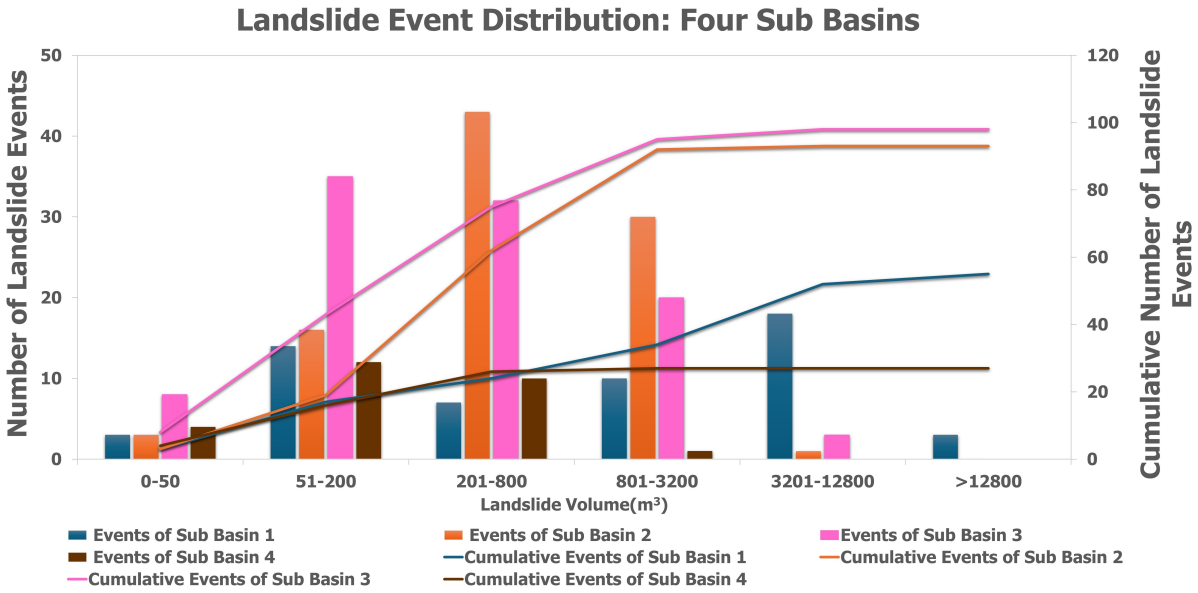

Figure 2.12: The number of landslide events for a range of volumes as well as the cumulative number of events when the study area is divided into four sub-basins as seen in Scenarios 4, 5, 8, and 10 [45].

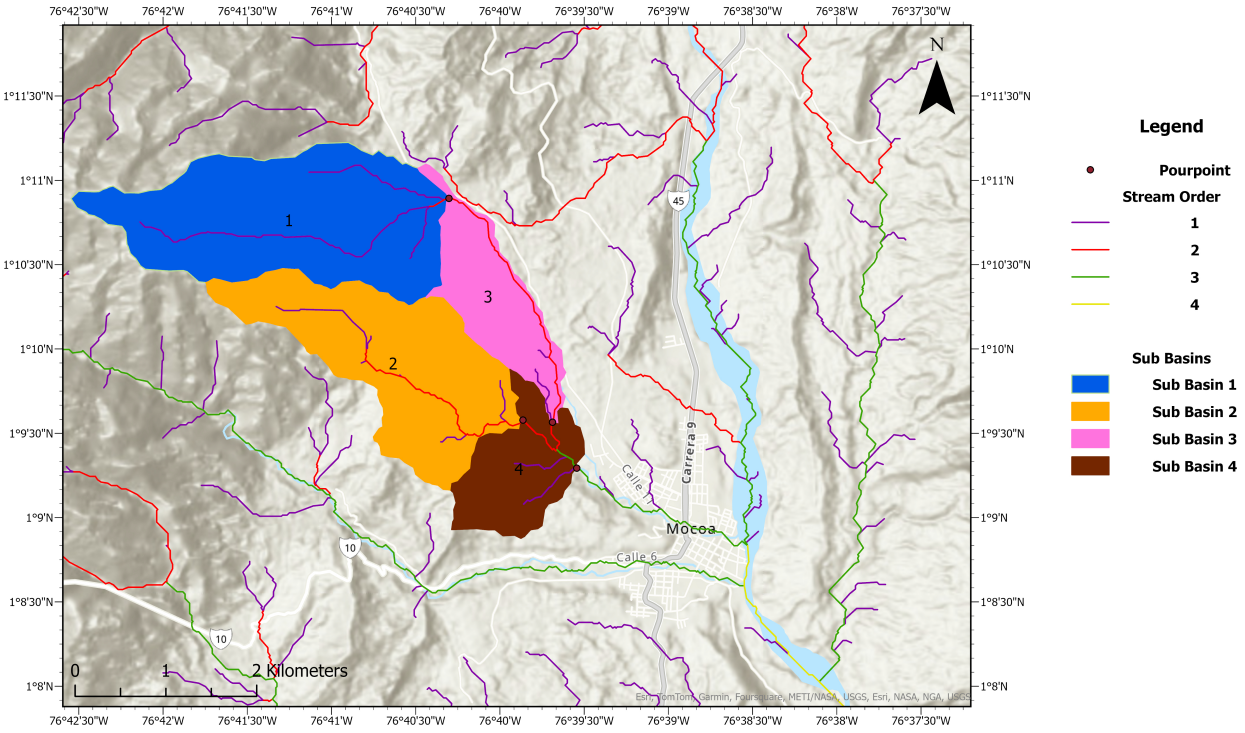

Figure 2.13: The four sub-basins created by considering second and third-order streams. These sub-basins are used in Scenarios 4, 5, 8, and 10.

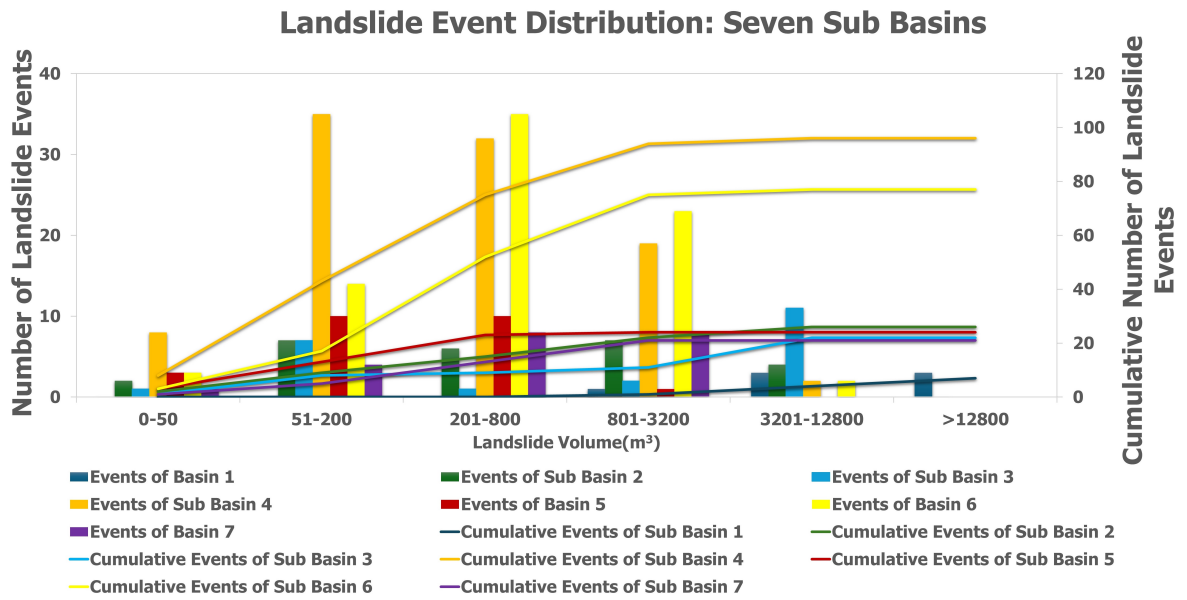

Figure 2.14: The number of landslide events for a range of volumes as well as the cumulative number of events when the study area is divided into seven sub-basins, as seen in Scenarios 6, 7, 9, and 11.

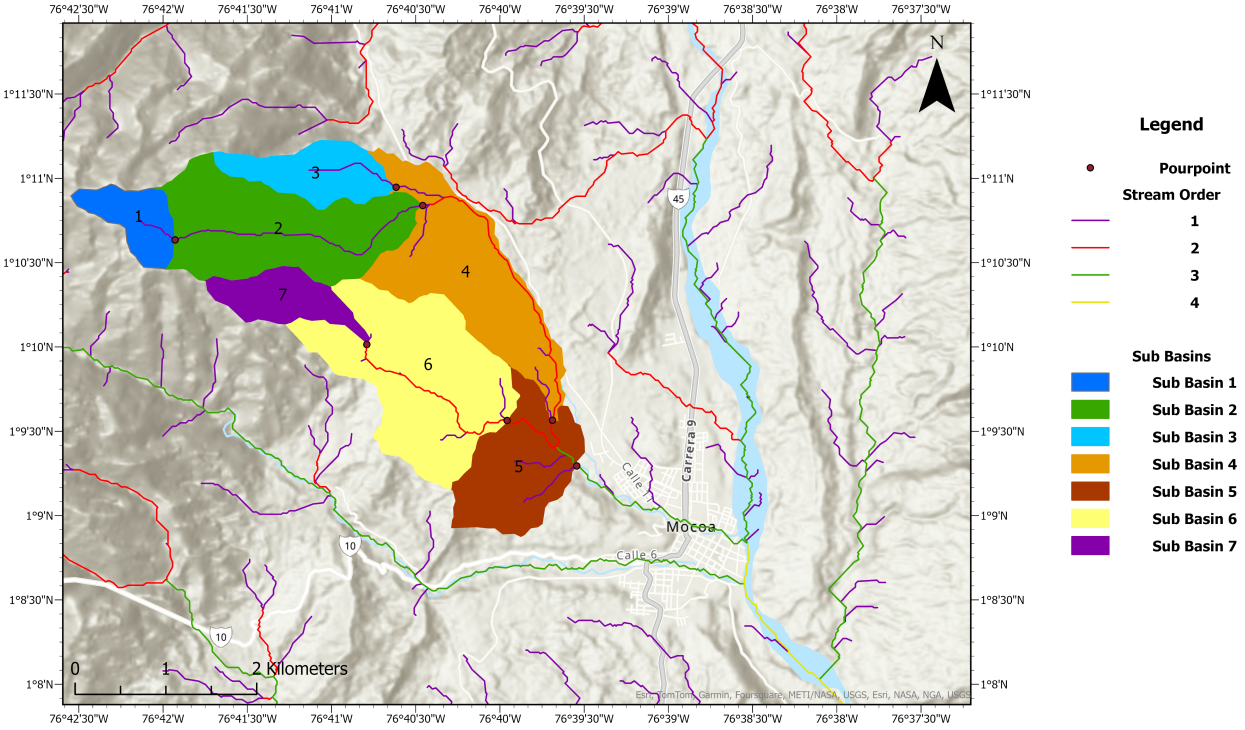

Figure 2.15: The seven sub-basins created by considering first, second and third order streams. These sub-basins are used in Scenarios 6, 7, 9, and 11.

2.6. Transient Rainfall Infiltration and Grid-Based Regional Slope-Stability Model (TRIGRS)

2.6.1. Introduction

The Transient Rainfall Infiltration and Grid-Based Regional Slope-Stability Model (TRIGRS) is a Fortran-based program used to evaluate the spatial and time effects of rainfall on landslide occurrence. It

determines the response of slope stability to the simulated rainfall and resulting transient pore pressure changes [40]. TRIGRS is a process-based landslide susceptibility method.

First, the model accepts a digital terrain model, soil characteristics, rainfall intensities, and initial hydraulic conditions. It then applies the methods of Iverson (2000) for saturated conditions or Srivastava and Yeh (1991) for partially saturated conditions to solve equations by Richard (1931) describing the flow of liquids in unsaturated porous mediums [40] [79] [80][81]. Richard's equations are based on Darcy's law, which states that the flux of water through saturated porous media is directly proportional to the hydraulic gradient [81] [82]. TRIGRS is then able to evaluate the effects of rainfall infiltration on landslide occurrence, timing, and depth [79].

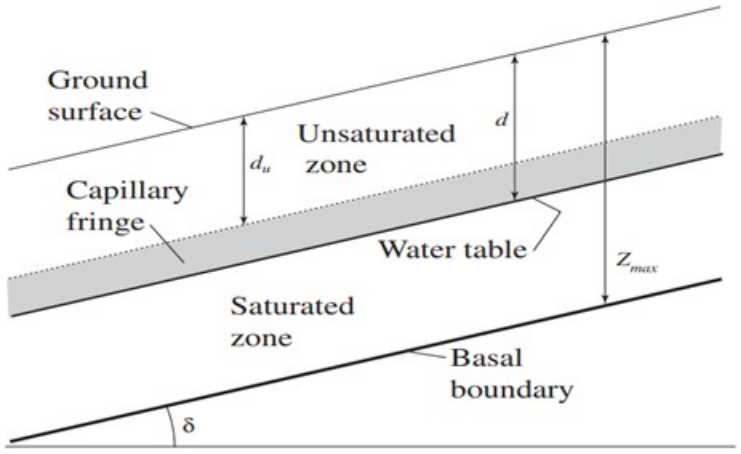

Figure 2.16: The TRIGRS hydrological model from Baum et al. (2008). The depth of the unsaturated layer is "d_u". While "Z_{max}" is the depth of the basal boundary from the ground surface. The depth of the soil above the water table is represented by "d", while "δ" is the slope angle. [40]

2.6.2. Model Assumptions

As per Baum et al. (2008) and Iverson (2000), the TRIGRS model makes the following assumptions [40] [79]:

1. Slope thickness and soil properties are uniform throughout each zone.
2. One-dimensional infinite-slope stability analysis is valid, which is why all forces that are not resolvable in planes parallel to the ground surface are neglected. This approximation is valid only if H « L, where H is the slip surface depth, and L is the landslide length or width.
3. Pore-water pressure is a function of time and depth only.
4. The model assumes flow in homogeneous, isotropic soil in one dimension with vertical infiltration that occurs at a specified rate of fixed duration at the ground surface.
5. An infinitely deep impermeable basal boundary is considered.
6. Flow is always in the linear range for Darcy's law, and hydraulic diffusivity is constant.
7. A balance of mass between rainfall input, infiltration, and runoff is maintained over the entire grid.
8. Complete saturation is assumed below the water table.
9. Runoff occurs from a particular cell when the sum of precipitation to that cell and runoff from other cells exceeds the cell's infiltrability. The runoff from the cell either infiltrates another cell or reaches a sink within a time step.
10. Stream flow is not incorporated in the model, as runoff is considered to occur instantaneously from cell to cell.
11. Water is also assumed to runoff any cells where the water table is initially at the ground surface, and the initial infiltration rate is negative.

12. Evapotranspiration is neglected as it is of minor importance in storms. It is significant only at larger time scales in between storms.
13. The landslide thickness is much smaller than the up-slope groundwater contributing area.
14. The rainfall duration that triggers slope failure is much less than the steady-state groundwater response time.

2.6.3. Working Principle

Slope stability is modelled according to the infinite-slope stability analysis method proposed by Taylor, 1948 [83]. Failure of an infinite slope is characterized by the ratio of resisting basal friction to gravity-induced downslope basal driving stress. This ratio is called the factor of safety or F_S and is calculated at a depth Z.

$$F_S(Z,t) = \frac{\tan\phi'}{\tan\delta} + \frac{c' - \psi(Z,t)\gamma_w \tan\phi'}{\gamma_s Z \sin\delta\cos\delta} \tag{2.11}$$

Where c' is soil cohesion for effective stress, ϕ' is the soil friction angle for effective stress, γ_w is the unit weight of groundwater,γ_s is the unit weight of soil. Failure occurs when F_S<1 and stability exists where F_S >1. Equilibrium exists where F_S = 1. The depth Z where F_S first drops below 1 is the depth of landslide initiation. The initiation depth depends on soil properties and the time and depth variation of the pressure head, which depends on rainfall history [40]. The TRIGRS Model calculates "Ψ" - the ground-water pressure head under unsaturated conditions with the limitation that the pressure head of gravity-driven flow cannot exceed the pressure head from having the water table at the ground surface, using the following equation [40]:

$$\begin{aligned}
&\psi\,(Z,t) = (Z-d)\,\beta \\
&+ 2\sum_{n=1}^{N} \frac{I_{nZ}}{K_S} H(t-t_n)[D_1(t-t_n)]^{\frac{1}{2}} \sum_{m=1}^{\infty} \left\{ \mathrm{ierfc}\left[\frac{(2m-1)d_{LZ} - (d_{LZ}-Z)}{2[D_1(t-t_n)]^{\frac{1}{2}}}\right] + \mathrm{ierfc}\left[\frac{(2m-1)d_{LZ} + (d_{LZ}-Z)}{2[D_1(t-t_n)]^{\frac{1}{2}}}\right]\right\} \\
&- 2\sum_{n=1}^{N} \frac{I_{nZ}}{K_S} H(t-t_{n+1})[D_1(t-t_{n+1})]^{\frac{1}{2}} \sum_{m=1}^{\infty} \left\{ \mathrm{ierfc}\left[\frac{(2m-1)d_{LZ} - (d_{LZ}-Z)}{2[D_1(t-t_{n+1})]^{\frac{1}{2}}}\right] + \mathrm{ierfc}\left[\frac{(2m-1)d_{LZ} + (d_{LZ}-Z)}{2[D_1(t-t_{n+1})]^{\frac{1}{2}}}\right]\right\}
\end{aligned} \tag{2.12}$$

and,

$$\mathrm{ierfc}(\eta) = \frac{1}{\sqrt{\pi}} \exp\left(-\eta^2\right) - \eta\,\mathrm{erfc}(\eta), \tag{2.13}$$

Where, d_{LZ} is the depth of the impermeable basal boundary measured in the Z-direction; $\mathrm{erfc}(\eta)$ is the complementary error function; $Z = z/\cos\delta$, where Z is the vertical coordinate direction (positive downward) and depth below the ground surface, z is the slope-normal coordinate direction (positive downward), and δ is the slope angle as seen in Figure 2.16. d is the steady-state depth of the water table measured in the vertical direction; $\beta = \cos^2\delta - (I_{\mathrm{ZLT}}/K_s)$. Where K_s is the saturated hydraulic conductivity in the Z direction and I_{ZLT} is the steady (initial) surface flux; I_{nz} is the surface flux of a given intensity for the nth time interval; $D_1 = D_0/\cos^2\delta$, where D_0 is the saturated hydraulic diffusivity; N is the total number of time intervals; and $H(t-t_n)$ is the Heaviside step function where t_n is the time at the nth time interval in the rainfall infiltration sequence [40].

2.6.4. Limitations

As per Baum et al. (2008) and Iverson (2000), the TRIGRS model has the following limitations [40] [79]:

1. Areas with extreme soil anisotropy or heterogeneity in hydrologic properties may cause errors in the solution.
2. Pore pressure results are not accurate for extended periods of alternating rainstorms. As in this scenario, both lateral flow and evapotranspiration are influential but not modelled by the program.
3. Results are sensitive to the initial conditions, such as water-table depth and hydraulic conductivity.

4. This one-dimensional model is not suitable for slopes steeper than 60°. Uncertainty of the infiltration becomes too large at these angles.
5. TRIGRS neglects soil strength evolution, such as contractile strain weakening, dilatant strain hardening, and fabric development.
6. The mechanical effects of 3-D dimensional geometries are neglected.

2.6.5. Conclusion

The ability of TRIGRS to model the timing and distribution of shallow, rainfall-induced landslides and provide dynamic source areas as output, as seen in Figure 2.17, makes it well suited to our study of debris flow surges caused by non-simultaneous landslides [40] [84] [27]. Furthermore, variable rainfall inputs are possible using a step function series [84], and the simple yet effective runoff routing model is said to work for large areas with limited data [85].

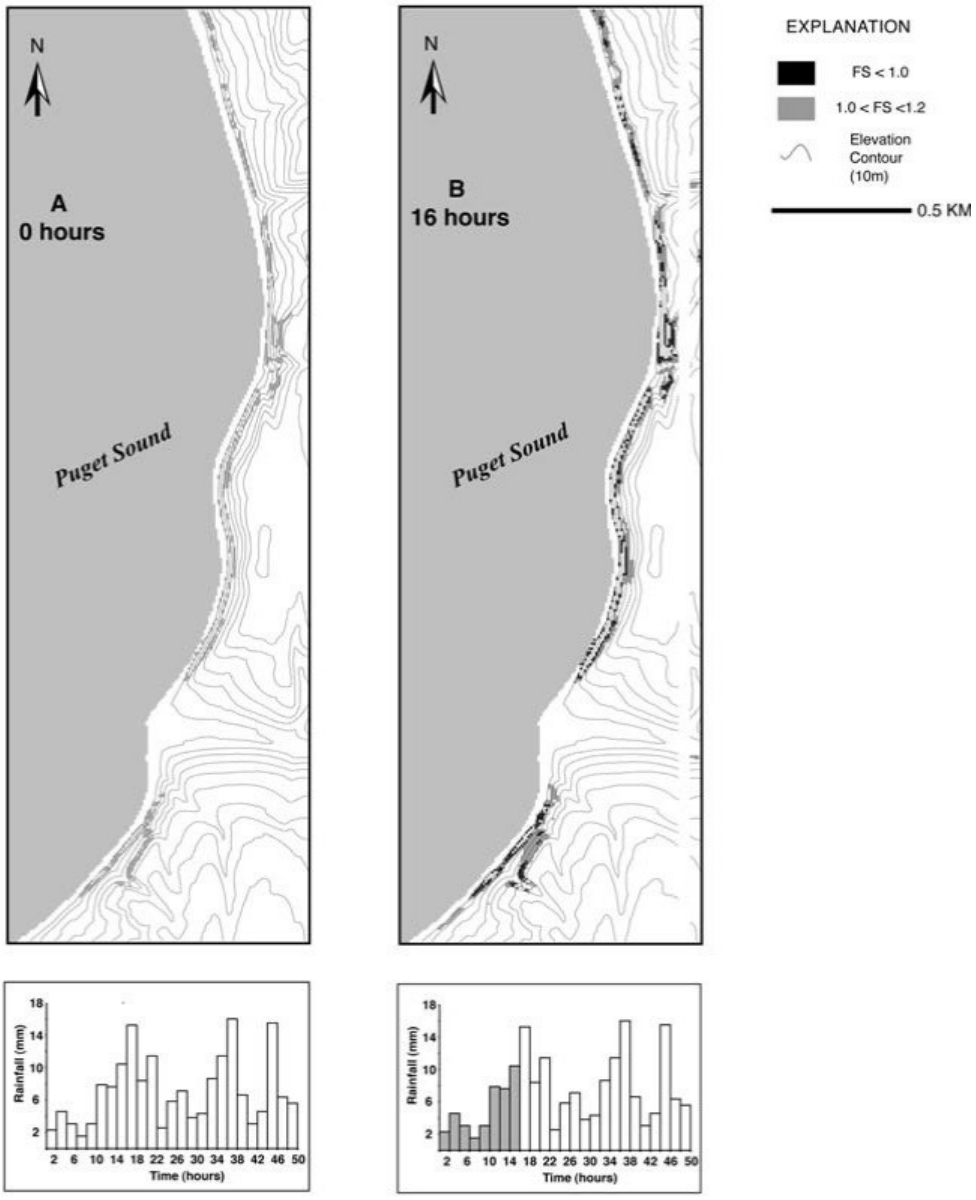

Figure 2.17: An example of the TRIGRS output adapted from Savage et al. (2005) showing the unstable regions changing with time and rainfall [86].

2.6.6. TRIGRS Analysis

The TRIGRS input seen in Table 2.2 is used to model the slope instability of the study area over space and time as a response to rainfall. Thereby determining the location of landslides as well as their time of occurrence. This information is then used to determine the volume, timing and location of debris flow surges.

Table 2.2: TRIGRS Input.

Input	Description	Source
Digital Elevation Model	$5m$ D.E.M. with geotechnical zonation	Chavarro et al. (2020) [87]
Geotechnical Parameters	Each zone is assigned parameters as seen in Table 2.3 and Figure 2.19	Chavarro et al. (2020) [87]
Groundwater Level	45% of soil depth in the zone.	Chavarro et al. (2020) [87]
Precipitation Data	Initially recorded at Mocoa Aqueducto Station with measurement errors corrected by SGC (2018)	SGC (2018) [45]

The $5m$ D.E.M. with geotechnical zonation by Chavarro et al. (2020) was used in TRIGRS because the geotechnical zones are demarcated within this D.E.M. The rainfall data seen in Figure 2.18 was recorded at the Mocoa Acueducto meteorological station in the town of Mocoa. The station's location is not ideal as it records readings in the valley, which may differ from the rainfall in the highlands, where most of the instabilities occur. It is known from records of the event that the debris flow passed through the town in the late hours of March 31st [45]. The storm is considered to be a hundred and two-hour period from 7 pm on the 27th of March to 1 am on the 1st of April divided into intervals of 6 hours each, as deemed statistically relevant by Chavarro et al. (2020) [87]. The Mocoa basin was classified into 16 zones by Chavarro et al. (2020), each with its own geotechnical parameters as seen in Table 2.3 and Figure 2.19.

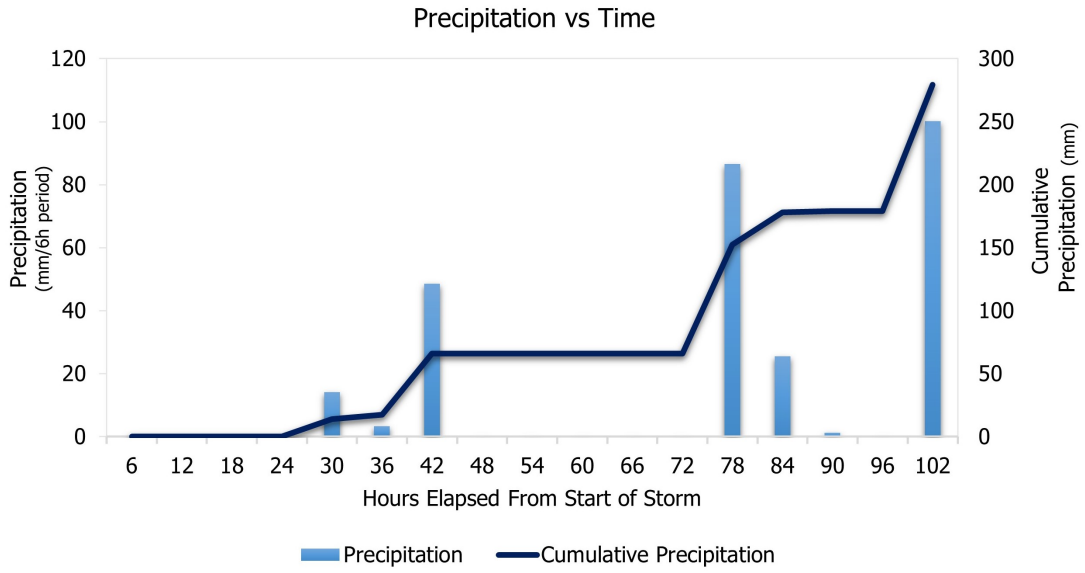

Figure 2.18: Precipitation vs Time for the 102-hour storm period.

Table 2.3: Geotechnical and hydraulic parameters for each of the 16 zones seen in Figure 2.19 courtesy Chavarro et al. (2020) [87].

Zone number	Soil depth (m)	Total Unit Weight (kN/m^3)	Cohesion (kPa)	Friction Angle (°)	Water content at saturation (%)	Residual water content (%)	Saturated hydraulic conductivity (m/s)	Hydraulic diffusivity (m^2/s)	Steady infiltration rate Iz (m/s)
1	2	15	65	28	42.33	0.18	3.31E-07	2.50E-05	5.00E-09
2	1.5	15	65	28	42.33	0.18	3.31E-07	2.50E-05	5.00E-09
3	2.5	15	65	28	42.33	0.18	3.31E-07	2.50E-05	5.00E-09
4	1.7	13	10	20	42.33	0.18	3.31E-07	2.50E-05	5.00E-09
5	1	17	30	20	49.48	0.18	5.00E-07	2.50E-05	5.00E-09
6	1	16	7	14	42.33	0.18	3.31E-07	1.50E-05	3.00E-09
7	1	15	15	28	42.33	0.18	3.31E-07	1.50E-05	3.00E-09
8	2	13	12	19	49.48	0.18	5.00E-07	2.50E-05	5.00E-09
9	2.5	17	50	33	35.17	0.18	5.42E-07	5.00E-05	1.00E-09
10	2	16	60	30	42.33	0.18	3.31E-07	2.50E-05	5.00E-09
11	0.5	13	100	19	49.48	0.18	5.00E-07	2.50E-05	5.00E-09
12	0.5	18	45	33	35.17	0.18	5.42E-07	2.50E-05	5.00E-09
13	0.5	18	25	33	35.17	0.18	5.42E-07	1.50E-05	3.00E-09
14	1.5	15	10	10	35.17	0.18	5.42E-07	1.50E-05	3.00E-09
15	1.7	13	10	20	42.33	0.18	3.31E-07	2.50E-05	5.00E-09
16	2	13	12	19	49.48	0.18	5.00E-07	2.50E-05	5.00E-09

Of the parameters seen in Table 2.3, soil depth was estimated from geological descriptions and field measurements [87]. Total unit weight, cohesion, friction angle and hydraulic conductivity were estimated from soil texture information provided by the Geological Survey of Colombia (SGC) and the Agustín Codazzi Geographic Institute (IGAC) [87]. While the particle size distribution was estimated from classifications made by the United States Department of Agriculture (USDA) [87]. Water content at saturation, Residual water content, Saturated hydraulic conductivity, Hydraulic diffusivity and Steady infiltration rate were based on the particle size distribution and soil classification and were determined by Chavarro et al. (2020) using the MACRO 5.2 model, a one-dimensional, process based soil-water-permeability model [87] [88]. The water table was determined by Chavarro et al. (2020) to be at 45% of soil depth from studying rainfall in the days leading up to the storm period, and by using HYDRUS 1D, a modelling environment for analysis of water flow and solute transport in variably saturated porous media [87] [89]. This information, along with a $5m$ D.E.M., was used to arrive at the distribution of slope stability over the area for the four-day period. The output for the 96th hour, as seen in Figure 2.20, was favourably verified against that of Chavarro et al. (2020) [87]. As per Chavarro et al. (2020), a relative error of about 7% exists in predicting unstable volumes compared to the landslide inventory volume for the whole basin by SGC (2018) [87]. This error is seen in the intermediate zone where no instability is predicted at a Factor of Safety (FoS) of 1. Increasing the Factor of Safety to 1.07 predicts some of the instabilities in the intermediate zone; however, it then falsely predicts greater instabilities in the high-land region. Consequently, the FoS was retained as 1 for further analyses. The distribution of landslide instability in space and over time, obtained from TRIGRS is used in Section 3.3.1 to determine debris flow surge volume and timing.

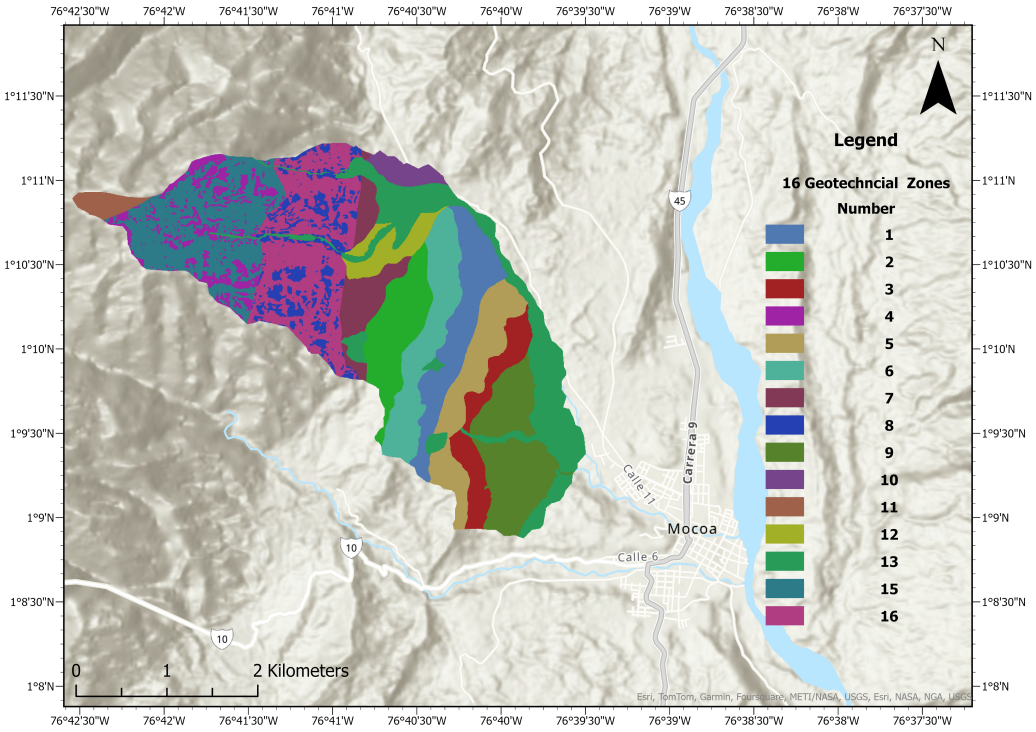

Figure 2.19: TRIGRS Input: The 16 geotechnical zones demarcated by Chavarro et al. (2020) based on the parameters seen in Table 2.3 [87].

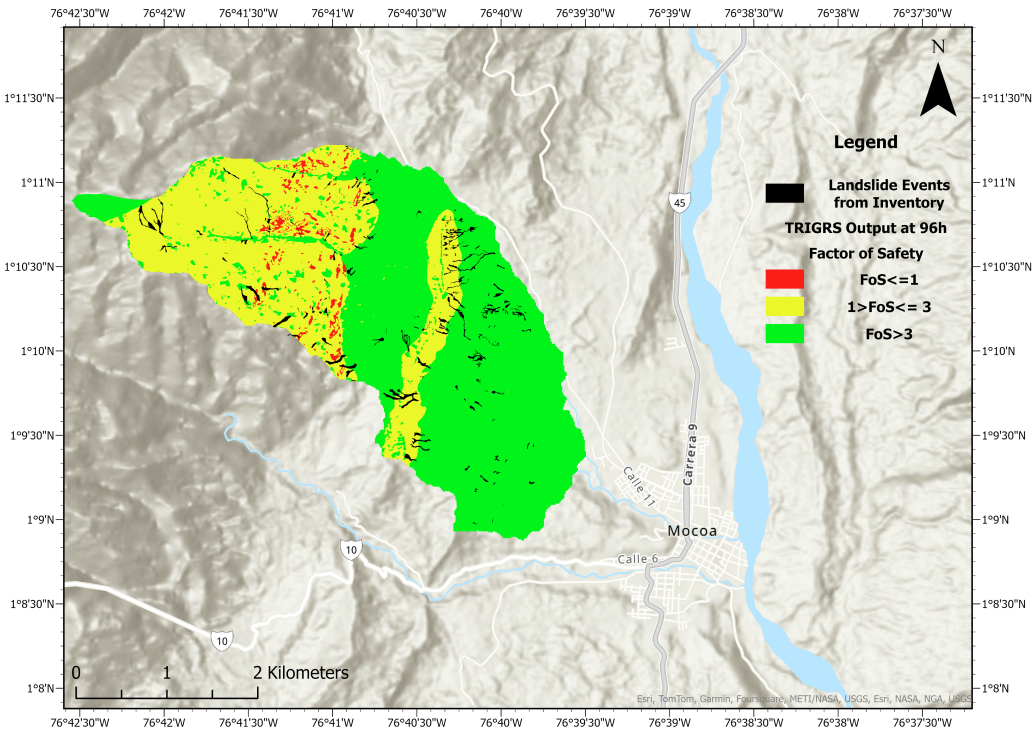

Figure 2.20: TRIGRS Output Factor of Safety at the sixteenth time step ($96h$). Red indicates unstable areas with yellow and green indicating stable areas.

2.7. Simulation Approach

Eleven Scenarios are planned, with each helping to answer one or more research questions. In Table 2.4, the scenarios are described, and the research question they aim to answer is mentioned. Scenarios 1 and 2 are simulated to see if using the landslide inventory is a feasible approach to the spatial resolution of events. Scenarios 3, 4, and 6 develop from the need to spatially resolve source areas before the time-resolved analysis is conducted on Scenarios 8 and 9. Scenarios 2, 5, and 7 are considered as they cover the highland area similar to what was considered by Reyes et al. (2018) and Correa (2023) [46] [48]. Scenarios 8 and 9 are compared to Scenarios 4 and 6 to check if simulating surging has an effect on runout prediction, which is the focus of this study. Scenarios 10 and 11 are included to see if and how, considering the deposition of surges as done in Scenarios 8 and 9, impacts the predicted runout.

Table 2.4: The simulation program consists of eleven scenarios. The horizontal line after Scenario 7 indicates the separation between the spatially resolved scenarios above the line and the time-resolved scenarios below it.

Scenario	Description of Scenario	Modelling Tool Implemented	Modelled Volume (m^3)	Research Question	Basin Division	Block Release(s)	Simulated Runout
1	Scenario 1 uses all 273 mapped landslides over the entire source area as initiation locations.	RAMMS	2.6×10^6	a, b	-	Figure 3.1a	Figure 3.3a
2	Scenario 2 considers only the 149 mapped landslides of the highland source area for initiation locations.	RAMMS	2.1×10^6	b, c	-	Figure 3.6a	Figure 3.8a
3	Scenario 3 considers a single basin that encapsulates the entire debris flow source area and uses a single block release.	RAMMS	2.6×10^6	1, a	Figure 2.11	Figure 3.1b	Figure 3.3b
4	Scenario 4 divides the debris flow source area into four sub-basins with a block release in each one.	RAMMS	2.6×10^6	1, a	Figure 2.13	Figure 3.1c	Figure 3.4a
5	Scenario 5 divides the debris flow source area into four sub-basins, but considers only the two sub-basins of the highland area with a block release in each one.	RAMMS	2.0×10^6	c	Figure 2.13	Figure 3.6b	Figure 3.8b
6	Scenario 6 divides the debris flow source area into seven sub-basins with a block release in each one.	RAMMS	2.6×10^6	1, a	Figure 2.15	Figure 3.1d	Figure 3.4b
7	Scenario 7 divides the debris flow source area into seven sub-basins, but considers only the five sub-basins of the highland area with a block release in each one.	RAMMS	2.1×10^6	c	Figure 2.15	Figure 3.6c	Figure 3.9a
8	Scenario 8 resolves the debris flow into five surges and four sub-basins.	TRIGRS, RAMMS	2.6×10^6	1,d	Figure 2.13	Figure 3.13	Figure 3.16a
9	Scenario 9 resolves the debris flow into five surges and seven sub-basins.	TRIGRS, RAMMS	2.6×10^6	1,d	Figure 2.15	Figure 3.15	Figure 3.16b
10	Scenario 10 is the same as Scenario 8, except it disregards surge depositions.	TRIGRS, RAMMS	2.6×10^6	1,d	Figure 2.13	Figure 3.13	Figure 3.16c
11	Scenario 11 is the same as Scenario 9, except it disregards surge depositions.	TRIGRS, RAMMS	2.6×10^6	1,d	Figure 2.15	Figure 3.15	Figure 3.16d

2.8. Scenario Performance Assessment Criteria

The scenario performance assessment criteria are made up of three key metrics: the Area Coverage Ratio, the Area Outrun Ratio, and the measurement of velocity and width at critical sections.

2.8.1. Area Ratios

This study uses an Area Coverage Ratio and an Area Outrun Ratio to assess the performance of the simulation. The Area Coverage Ratio and the Area Outrun Ratio are defined below.

Given, the Area of Simulated Runout is represented by A_S. The Area Coverage Ratio is the ratio of the Area of the Simulated Runout that lies within the bounds of the measured runout (A_B) and the Measured Runout (A_M) given by;

$$\text{Area Coverage Ratio} = \frac{A_B}{A_M} \tag{2.14}$$

In order to quantify the simulated runout exceeding the Measured Runout Area known as the Area Outrun (A_O), the following ratio is proposed;

$$\text{Area Outrun Ratio} = \frac{A_S - A_B}{A_B} = \frac{A_O}{A_B} \tag{2.15}$$

2.8.2. Release Ratio

The Number of Block Releases (B_N) in a scenario normalised by the total number of landslides (L_N) is termed as the Release Ratio.

$$\text{Release Ratio} = \frac{B_N}{L_N} \tag{2.16}$$

A larger Release Ratio indicates that the scenario has a greater spatial and or time resolution.

2.8.3. Velocity and Width at Cross-Sections of Interest

Sections 1, 2, and 3, as seen in Figure 2.21, were selected to represent points in the runout path where the debris flow has experienced a minimum to moderate to a near complete interaction with infrastructure, respectively. Section 1 is located just ahead of the Mocoa power station, a critical piece of infrastructure that was destroyed by the debris flow. Section 2 is located near residential neighbourhoods that were affected by the debris flow. Section 3 is located in the town across the main road before the debris flow meets the Mocoa River. The variation of velocity and flow width was measured at these sections. The ratio of Simulated Runout Width (S_W) and Measured Runout Width (M_W) is given by

$$\frac{S_W}{M_W} \tag{2.17}$$

Flow velocity was calculated by Garcia-Delgado et al. (2019) at Section 1 as $2.86m/s$ using the Manning Method [43]. Flow velocity was not calculated in the vicinity of Sections 2 and 3. Estimates of the debris flow velocity vary from $5m/s$ by Sarmiento et al. (2019) to $12m/s$ Garcia-Delgado et al. (2019), however, no specific velocity estimate is available for Sections 2 and 3 [43] [2]. While the ratio of Simulated Velocity (V_S) and Calculated Velocity (V_C) is given by

$$\frac{V_S}{V_C} \tag{2.18}$$

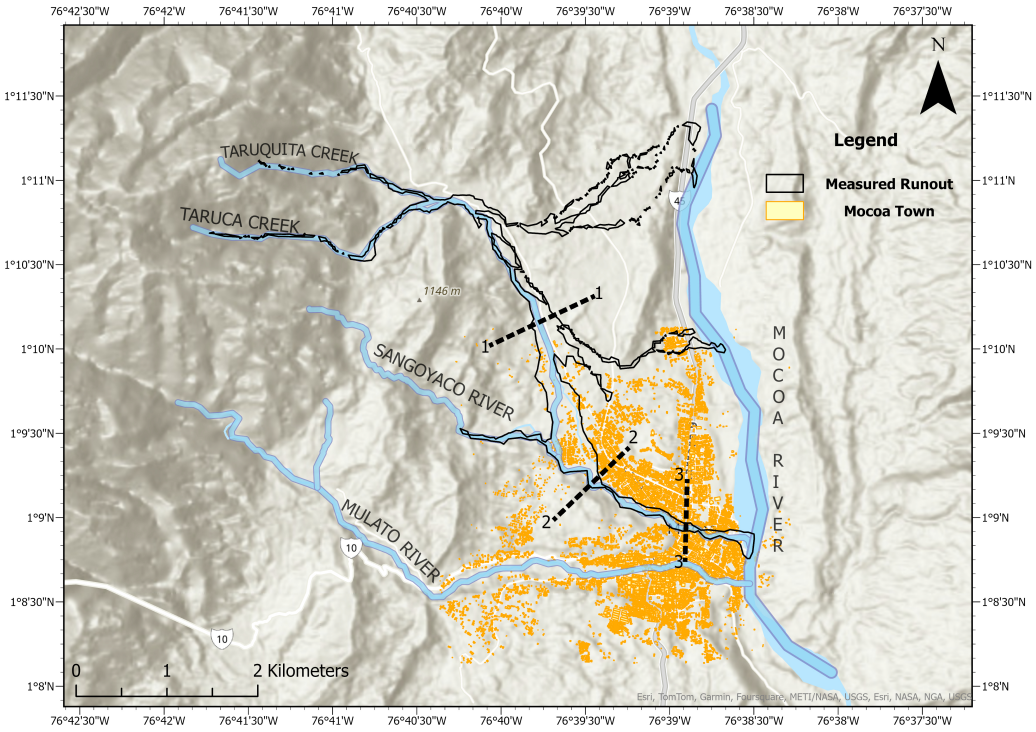

Figure 2.21: The three sections of interest. Sections 1, 2, and 3 within the study area.

The two metrics of Area Coverage Ratio and Area Outrun Ratio will allow us to judge the accuracy and precision of the simulation, respectively. Measuring the width and velocity at the three sections will give us a closer view of debris flow behaviour in key areas. Together, these criteria enable us to objectively assess the performance of all scenarios.

3

Runout Analysis

3.1. Introduction to The Analysis

The analysis consists of two parts. The first part, Section 3.2, is a Spatial Analysis where the debris flow is simulated in seven scenarios that vary the source areas considered. Four of these scenarios, Scenarios 1, 3, 4, and 6, are introduced in Sub Section 3.2.1 and consider the entire source area. They were designed to answer the main research question regarding debris flow surges, the first sub-question on the effect of source area spatial resolution on runout simulations and the second sub-question examining the feasibility of using the exact location of landslides in the simulation. The other three scenarios, Scenarios 2, 5, and 7, consider only the highland region and are introduced in Sub Section 3.2.2. This division of scenarios is made to answer the third sub-research question regarding the sufficiency of only considering the highland area versus the entire source area. The second part of the analysis, Section 3.3 describes the time-resolved analysis of scenarios, which goes to addressing the main research question regarding debris flow surges. The surges are estimated in Sub Section 3.3.1 while the four simulated scenarios, Scenarios 8, 9, 10, and 11, are introduced in Sub Section 3.3.2. These four scenarios go to answering the main research question regarding debris flow surges and the fourth and final sub-question concerning the effect of surge deposition on runout. For an overview of all scenarios, refer to Table 2.4.

Two release methods are used for the debris flow simulations; both are block releases but are differently applied. (a) The first utilises the mapped landslides as release areas, with the modelled volume confined within this area. This method was used to represent the idealised spatial resolution of events as it uses the exact location of the landslides. However, the large heights required ($> 10m$) to contain the volume within the mapped area violate the depth-averaged assumption RAMMS is based on. This is why this method is only seen in Scenarios 1 and 2. (b) In the second method, the release block length starts from the pour point and extends backwards along the stream channel. The width of the block is roughly that of the channel, and the height is limited to $10m$, as is practice when using block releases. This method is used for all other scenarios, i.e. Scenarios 3 to 11. The volume and location, otherwise known as the arrangement, of release blocks used in Scenario 4 and Scenario 6 of the spatial analysis are the same as the ones used in their corresponding time-resolved scenarios of Scenarios 8, 10, and 9, 11, respectively. The only modification is that the block is divided into smaller blocks, which release at different times based on the debris flow surge assessment performed in Section 3.3.1. Therefore, ensuring that the only difference between the spatial and time-resolved simulation is the timing of the volume released and not the arrangement of releases. This enables a direct comparison between spatial and time-resolved scenarios based on the effects of surging alone.

3.2. Spatially Resolved Analysis

The spatially resolved analysis consists of two parts; the first part, Sub Section 3.2.1, is where the whole source area is considered. The second part Sub Section 3.2.2 is where only the highland source area is considered. This division is made to better answer the sub-research question of whether considering

only the highland source area is sufficient to provide an accurate runout prediction. The highland area is comparable to the area considered by Reyes et al. (2018) and Correa (2023) [46] [48]. The scenarios are introduced and described in each sub-section, followed by the simulation output in terms of maximum runout height and maximum velocity.

3.2.1. Spatially Resolved Analysis Whole Source Area: Block Releases

This analysis consists of Scenarios 1, 3, 4, and 6, all of which consider the entire source area as shown in Figure 3.1. This results in a modelled volume of $2.6 \times 10^6 m^3$ for all scenarios as calculated in Section 2.4.

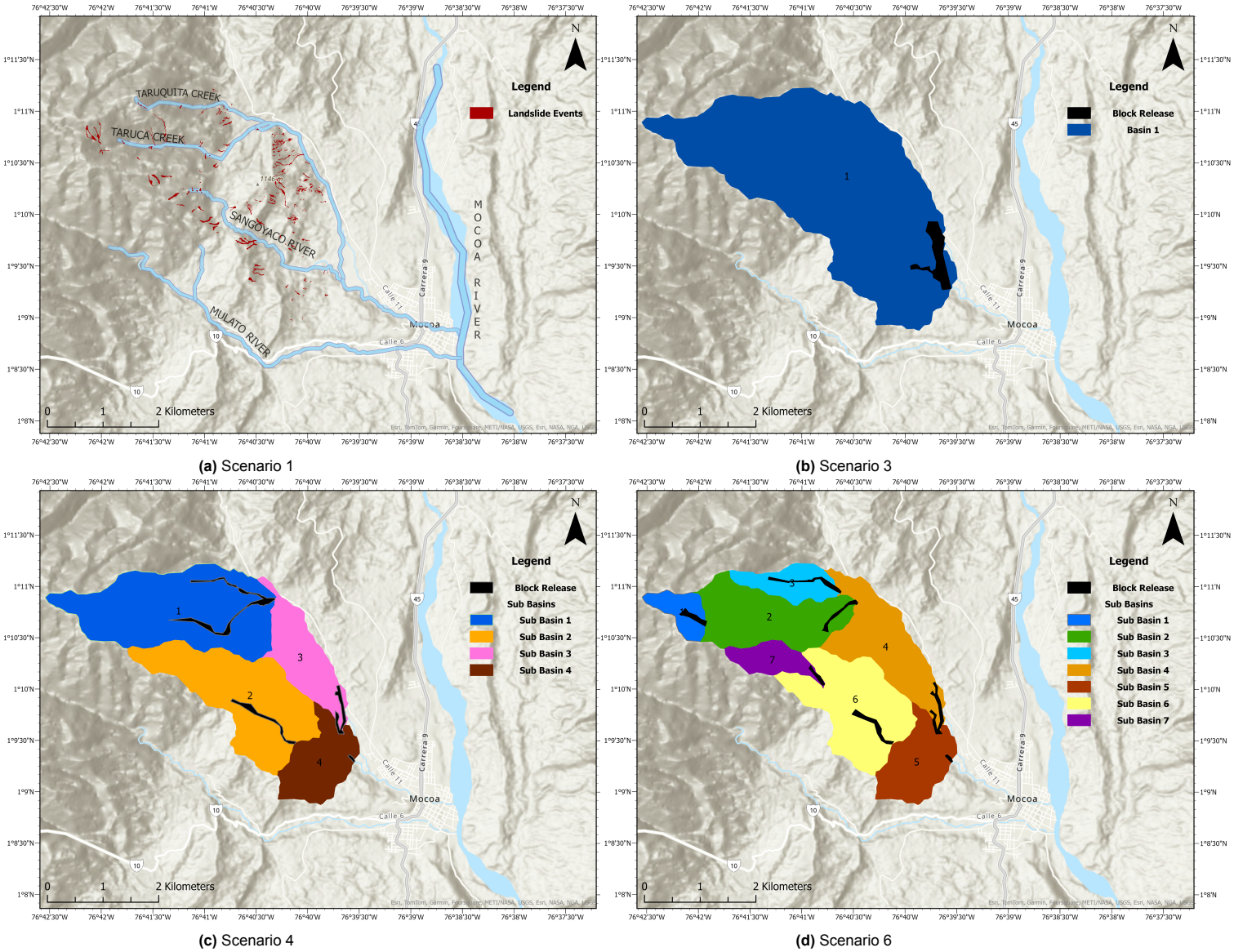

(a) Scenario 1 **(b)** Scenario 3

(c) Scenario 4 **(d)** Scenario 6

Figure 3.1: Block release locations of the four spatially resolved scenarios that consider the entire source area.

Scenario 1 is the idealised spatially resolved scenario, which uses the exact location of landslides from the inventory as release points, as seen in Figure 3.1a. Scenario 3 is the other extreme, where spatial resolution is minimum and the entire source area acts from a single block release, as seen in Figure 3.1b. Scenario 4 uses the division of the source area into four sub-basins as first seen in Figure 2.13, thus creating four block releases, one in each sub-basin as seen in Figure 3.1c. Scenario 6 is based on the division of the source area into seven sub-basins as first seen in Figure 2.15, creating seven block

releases as seen in Figure 3.1d. All four scenarios do not consider surging and are used to calculate the accuracy of runout simulation when the debris flows are initiated instantaneously with different spatial resolutions. Scenarios 4 and 6 serve as the basis for comparison against the time-resolved scenarios to answer the main research question. The distribution of the modelled volume from each sub-basin is seen in Figure 3.2a for Scenario 4 and in Figure 3.2b for Scenario 6. In Scenario 4, Sub-Basin 1 accounts for roughly 50% of all debris volume; this sub-basin is further divided into three sub-basins in Scenario 6, which noticeably changes the location of the block releases. Volume pie charts are omitted for Scenario 1 and 3 as they add little value, considering Scenario 1 consists of individual landslides and Scenario 3 consists of only a single release.

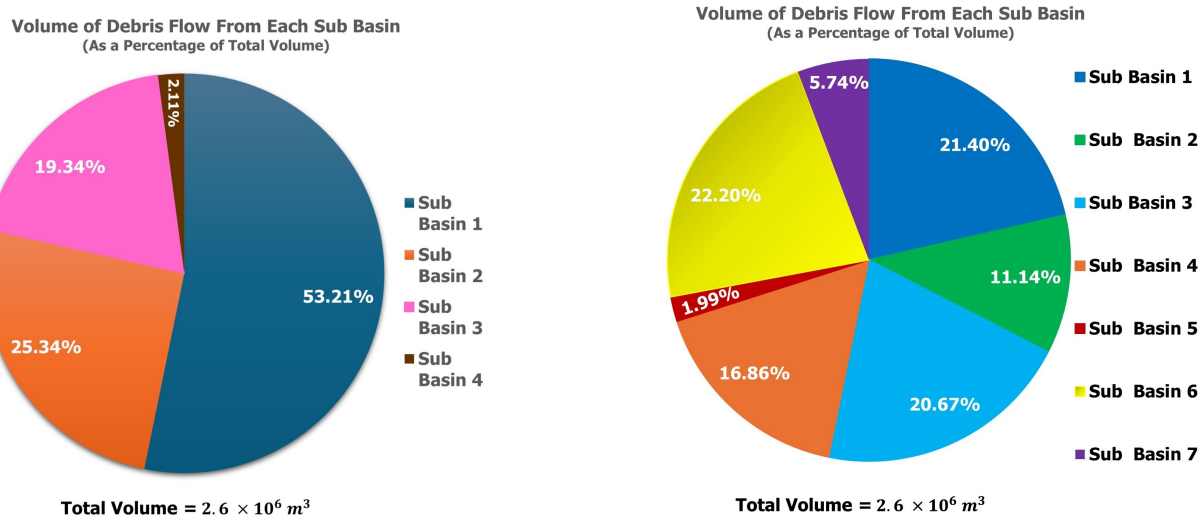

(a) Scenario 1 **(b)** Scenario 3

Figure 3.2: The distribution of the modelled volume from each sub-basin of Scenarios 4 and 6.

Spatially Resolved Analysis Whole Source Area: Maximum Runout Height

The maximum runout heights of Scenarios 1 and 3 are presented in Figure 3.3 and in Figure 3.4 for Scenarios 4 and 6.

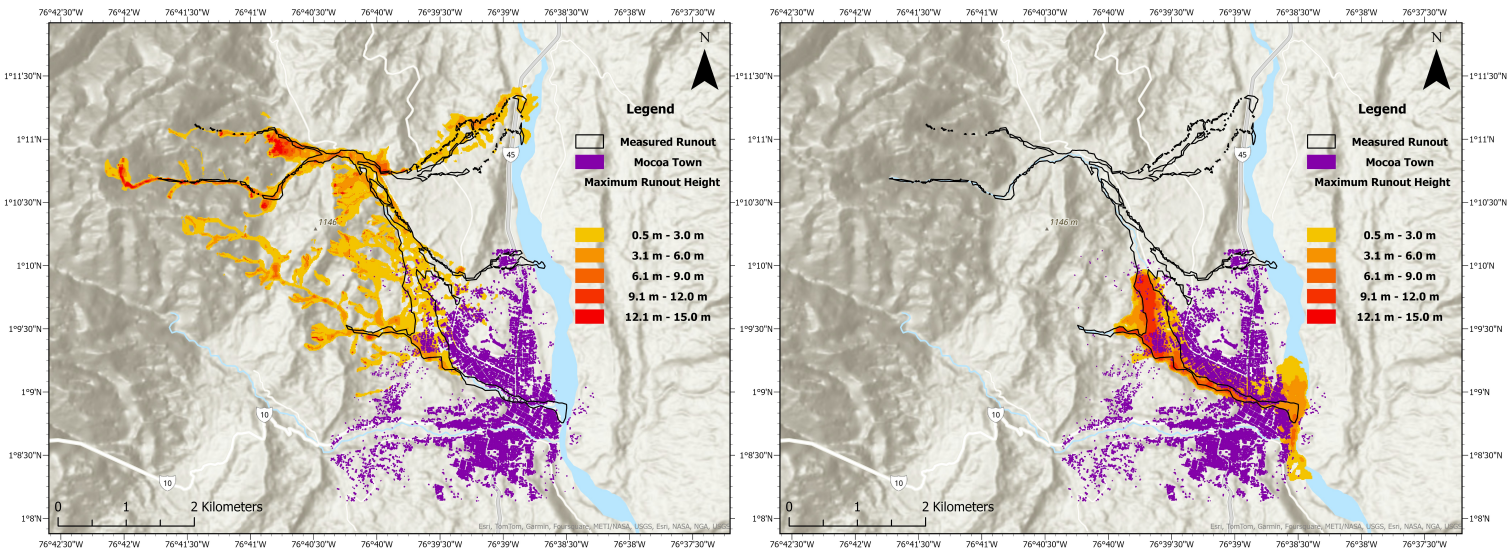

(a) Scenario 1 **(b)** Scenario 3

Figure 3.3: Maximum simulated runout heights for Scenarios 1 and 3.

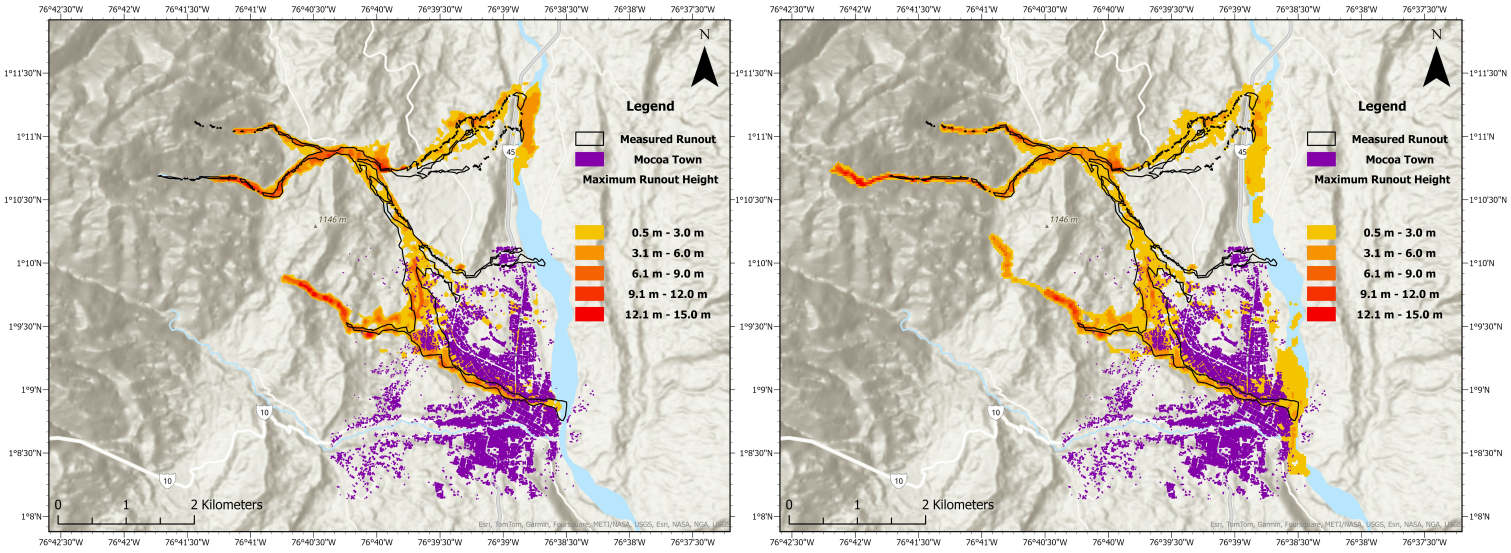

(a) Scenario 4

(b) Scenario 6

Figure 3.4: Maximum simulated runout heights for Scenarios 4 and 6.

In Figure 3.3a of Scenario 1, The simulated runout is spread around the measured runout. This indicates that the simulated flow path is not realistic, as many flows are channelised away from their true path. This is a consequence of using a $12.5m$ D.E.M. where the minor gullies do not match well with reality, and this conflicts with the exact nature of the landslide location being used as release points. This implies that an approximation of the release location is required by way of block releases along the significant channels, thereby reducing the effect of minor gullies on runout simulation. In Figure 3.3b of Scenario 3, The approximated location of the block release causes the runout to neglect the upper part of the measured path. This indicates that a single release is unsuitable, requiring greater spatial resolution. In Figure 3.4a of Scenario 4, the simulated runout appears to be largely faithful to the measured runout, with flow covering most areas, indicating a good reproduction of events. In Figure 3.4b of Scenario 6, the simulated runout is very similar to that of Scenario 4 but with greater discharge in the Mocoa River.

Spatially Resolved Analysis Whole Source Area: Maximum Runout Velocity

The maximum runout velocities of Scenarios 1, 3, 4 and 6 are presented in Figure 3.5

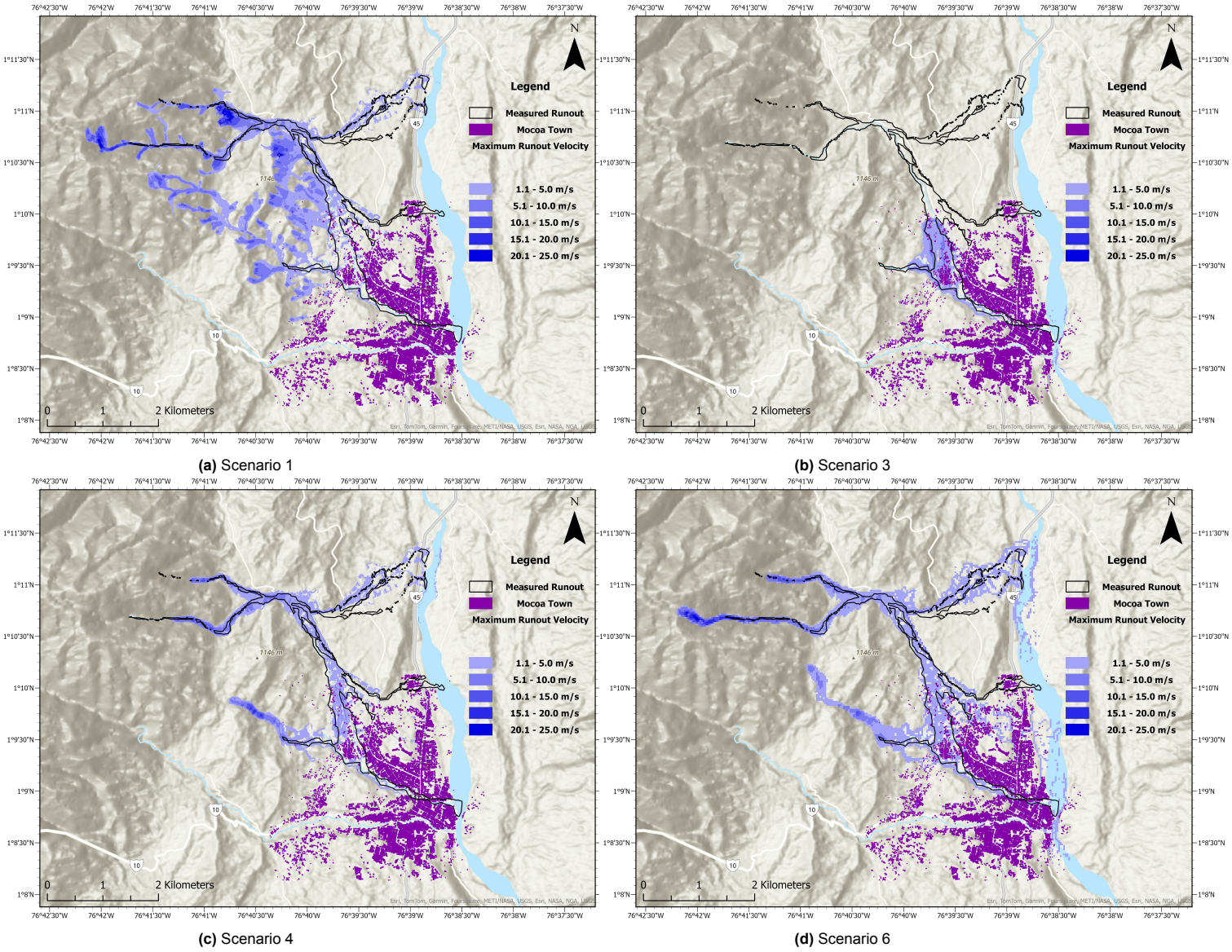

(a) Scenario 1 **(b)** Scenario 3

(c) Scenario 4 **(d)** Scenario 6

Figure 3.5: Maximum simulated runout velocities of the four spatially resolved scenarios that consider the entire source area.

All scenarios in Figure 3.5 indicate higher velocities near the initial release points and lower velocities as the flow is subjected to frictional and turbulent deceleration. Flow velocity is less than $5m/s$ near the urban area, while in the highlands, it reaches almost $25m/s$.

3.2.2. Spatially Resolved Analysis Highland Source Area: Block Releases

The arrangement of the block releases for Scenarios 2, 5 and 7 is presented in Figure 3.6

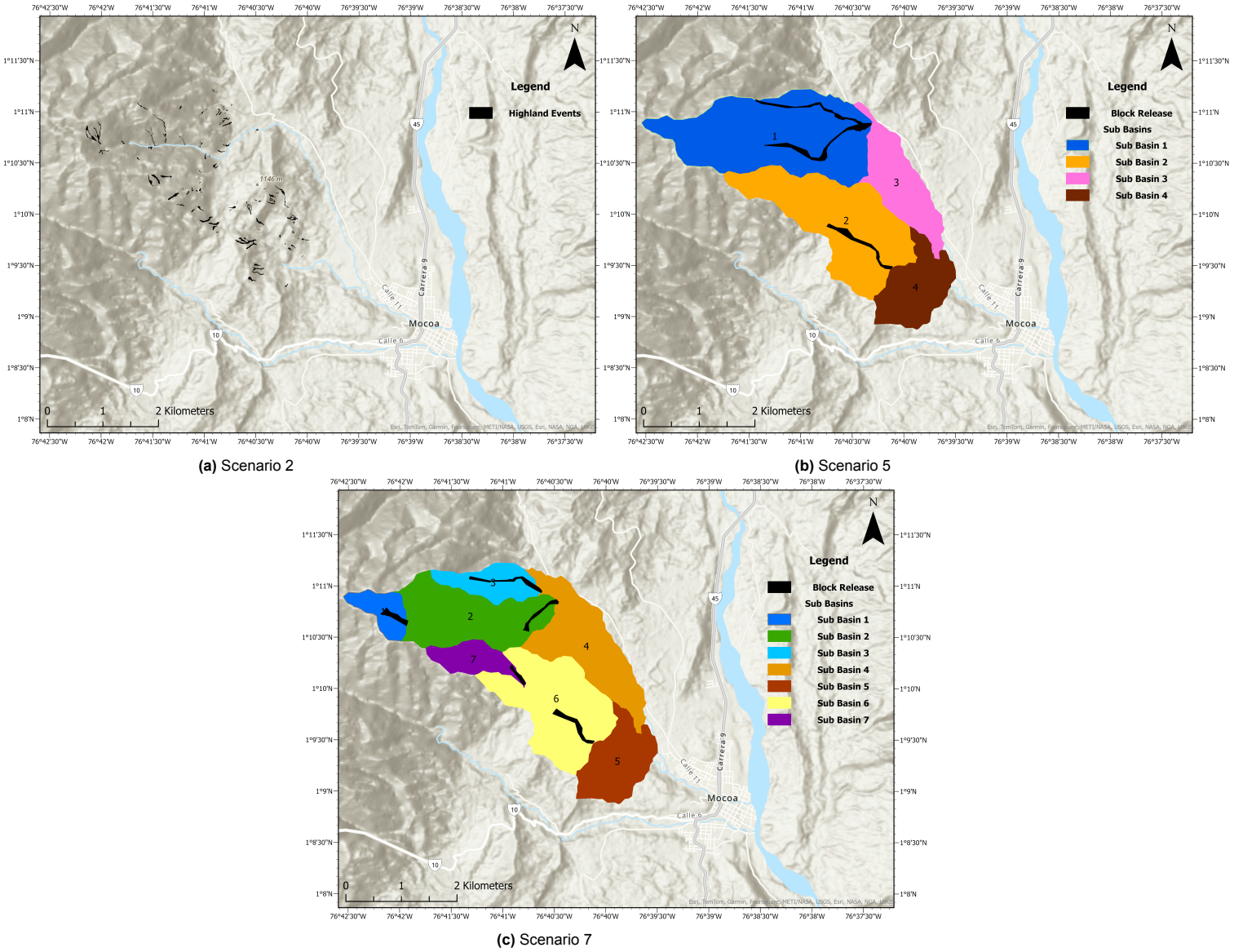

(a) Scenario 2

(b) Scenario 5

(c) Scenario 7

Figure 3.6: Block release locations of the three spatially resolved scenarios that consider only the highland source area.

Scenario 2 is the idealised spatially resolved scenario, which uses the exact location of landslides from the inventory as release points for only the highland areas seen in Figure 3.6a. Scenario 5 uses the division of the source area into four sub-basins as first seen in Figure 2.13 but considers only the highland sub-basins of Sub-Basin 1 and 2, thus creating two block releases, one in each sub-basin as seen in Figure 3.6b. Scenario 7 is based on the division of the source area into seven sub-basins as first seen in Figure 2.15 creating five block releases as seen in Figure 3.6c by considering only the highland region. All four scenarios do not consider surging and are used to calculate the accuracy of runout simulation when the debris flows are initiated instantaneously with different spatial resolutions in only the highland region. They serve to answer the third research sub-question on the appropriateness of studying only the highland region and ignoring the other areas of the case study. The distribution of the modelled volume from each sub-basin is highlighted in Figure 3.7a for Scenario 5 and in Figure 3.7b for Scenario 7. In Scenario 5, Sub-Basin 1 accounts for nearly 70% of all debris volume; this sub-basin is further divided into three sub-basins in Scenario 6, which noticeably changes the location of the

block releases. The increase in spatial resolution in Scenario 7 compared to Scenario 5 increases the modelled volume marginally by 5% as landslides on the edge of sub-basins are included or excluded when the new sub-basins are created. A volume pie chart is omitted for Scenario 2 as it adds little value, considering Scenario 2 consists of individual landslides. Scenario 2 has a modelled volume of $2.1 \times 10^6 m^3$.

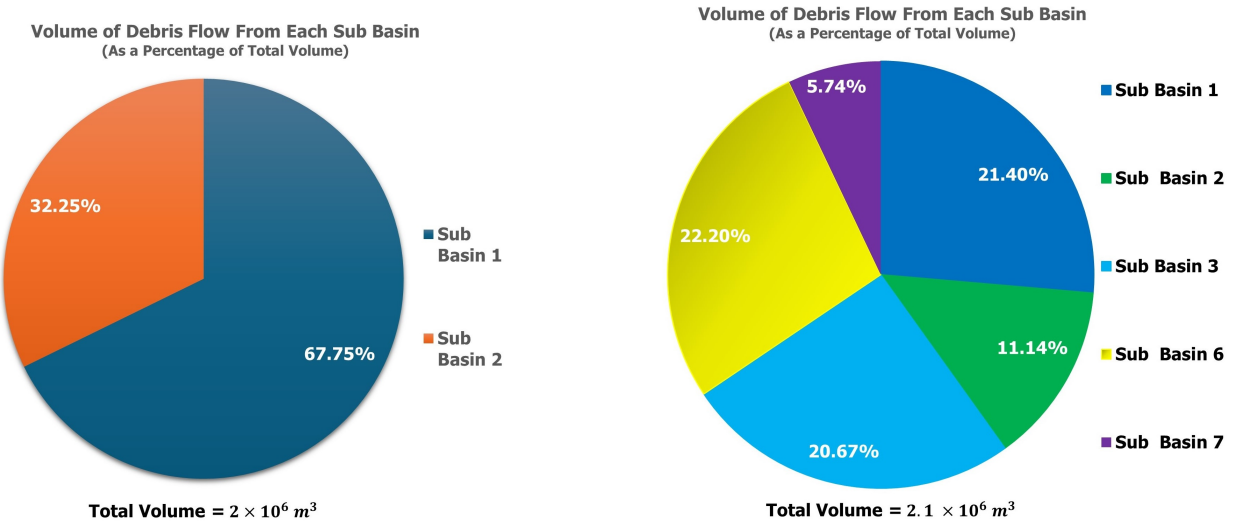

(a) Scenario 5 **(b)** Scenario 7

Figure 3.7: The distribution of the modelled volume from each sub-basin of Scenarios 5 and 7.

Spatially Resolved Analysis Highland Source Area: Maximum Simulated Runout Height

The maximum runout heights of Scenarios 2 and 5 are presented in Figure 3.8 and for Scenario 7 in Figure 3.9.

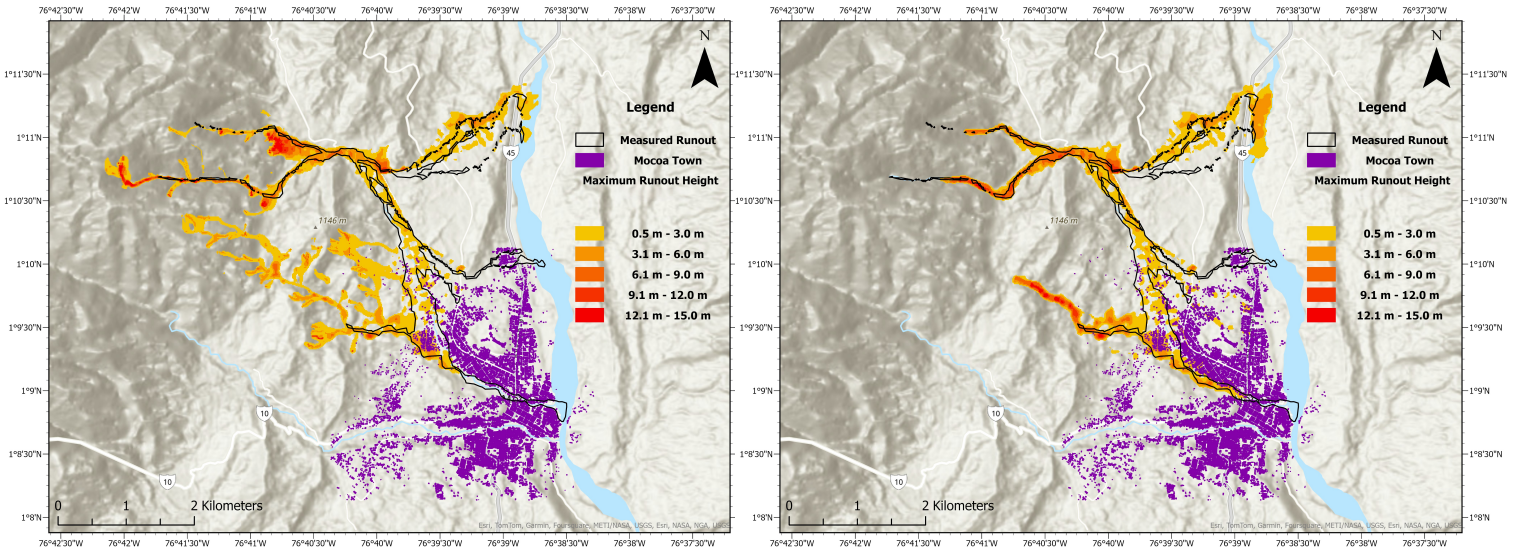

(a) Scenario 2 **(b)** Scenario 5

Figure 3.8: Maximum simulated runout heights for Scenarios 2 and 5, considering only the highland source area.

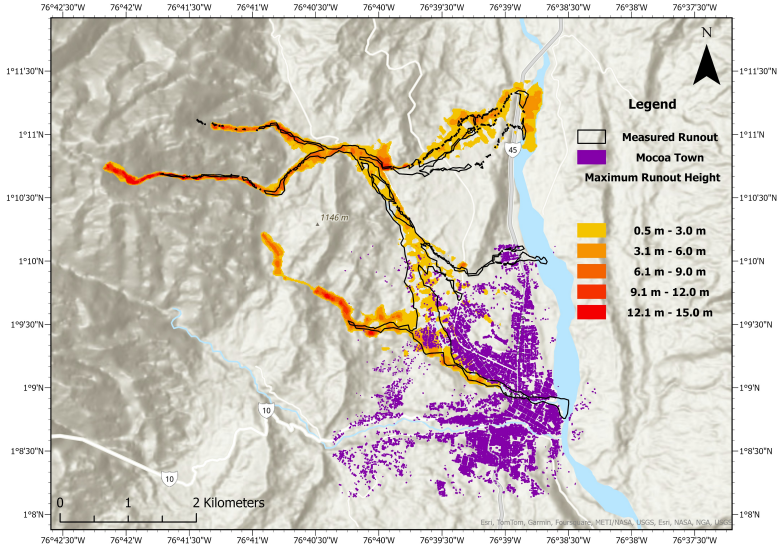

(a) Scenario 7

Figure 3.9: Maximum simulated runout height for Scenario 7, considering only the highland source area.

In Figure 3.8a of Scenario 2, The simulated runout is spread around the measured runout. This indicates that the simulated flow path is not realistic, as many flows are channelised away from their true path. As in the case of Scenario 1, this is a consequence of using a $12.5m$ D.E.M. where the minor gullies do not match well with reality and is at odds with the exact location of landslides being used as release points. This implies that an approximation of the release location is required by way of block releases along the significant channels for the highland region, thereby reducing the effect of minor gullies on runout simulation. In Figure 3.8b of Scenario 5, the simulated runout is noticeably shallow in the middle region, with some gaps being seen. In Figure 3.9a of Scenario 7, the simulated runout is very similar to that of Scenario 4, but it covers more of the initial runout path as a consequence of having block releases that are further apart. Of the three scenarios, Scenarios 5 and 7 appear to perform the best, with all three scenarios failing to simulate the discharge into the Mocoa River.

Spatially Resolved Analysis Highland Source Area: Maximum Simulated Runout Velocity

The maximum runout velocities of Scenarios 2, 5 and 7 are presented in Figure 3.10.

All scenarios in Figure 3.10 indicate higher velocities near the initial release points and lower velocities as the flow is subjected to frictional and turbulent deceleration. Near the urban area, the flow velocity is lower than $1m/s$, indicating that the lower volume simulated in the highland scenarios fails to provide sufficient momentum to the flow.

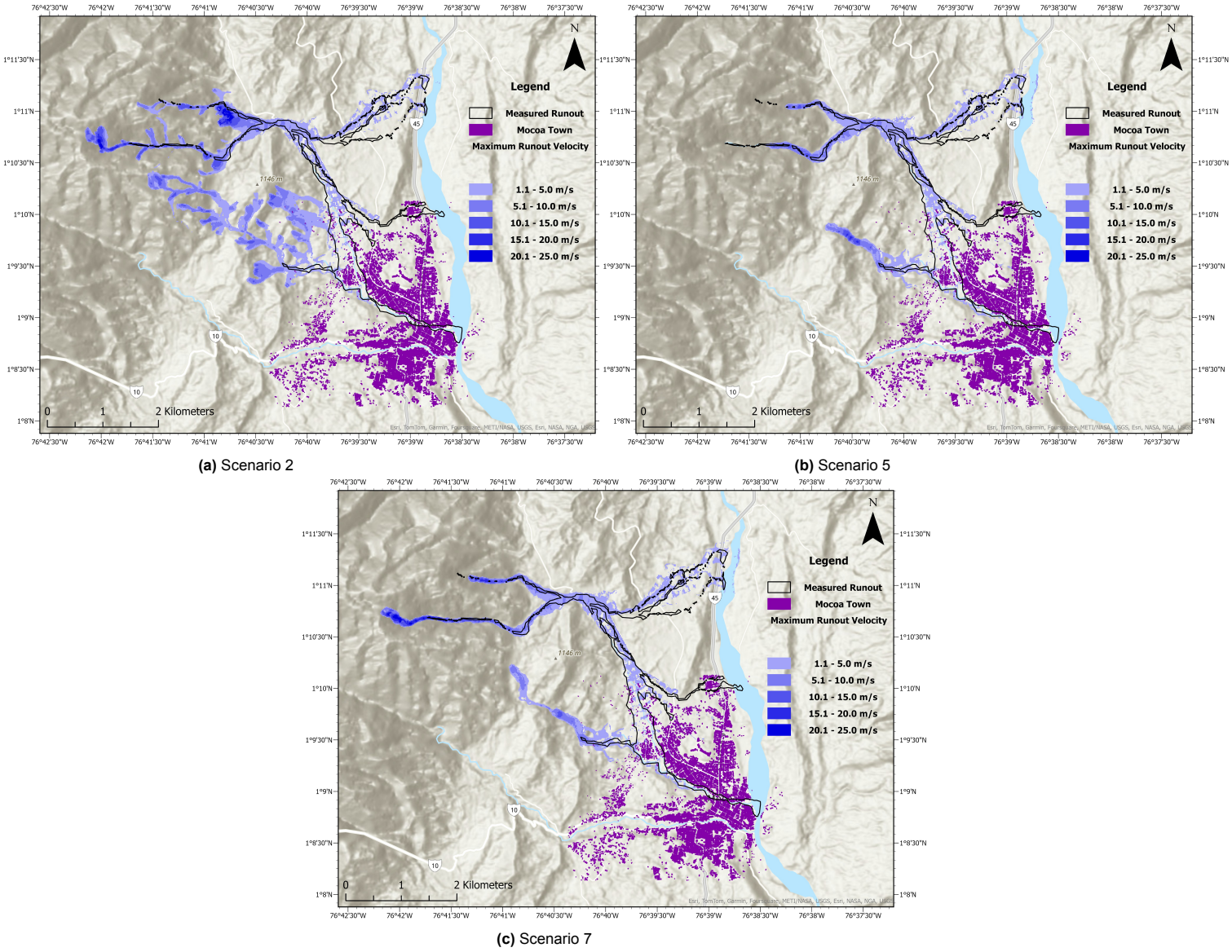

(a) Scenario 2 **(b)** Scenario 5

(c) Scenario 7

Figure 3.10: Maximum simulated runout velocities of the three spatially resolved scenarios that consider only the highland source area.

3.3. Time-Resolved Analysis

3.3.1. Debris Flow Surge Assessment

Although TRIGRS identifies slope failures, it cannot differentiate between those that mobilise into debris flows and those that do not. The unstable cells in each of the seventeen steps are reviewed to determine the volume of debris flow from the indicated instabilities. The first four time-steps record no instabilities and act as references to check that the ground is stable with time when no rainfall is recorded, as seen in Figure 3.11. Going forward in the analysis, this period $(0 - 24h)$ is subsequently left out. The next three steps (till the $42nd$ hour) record negligible instabilities. From the eighth time step onward $(42 - 48h)$, significant instabilities were recorded as seen in Figure 3.12. TRIGRS does not modify the D.E.M. to account for failed cells [87]. This means that cells that have failed in one time step may not be unstable in successive time steps. Therefore, only the time steps where a larger number of cells have failed than the time step before it are considered new failures. The largest number of unstable cells are recorded in the sixteenth time step $(90 - 96h)$, with a decrease occurring in the last time step $(96 - 102h)$. All unstable cells are normalised to the sixteenth time step, and a proportion of unstable areas is calculated. This gives us a ratio of instabilities for all the time steps from $48 - 96h$.

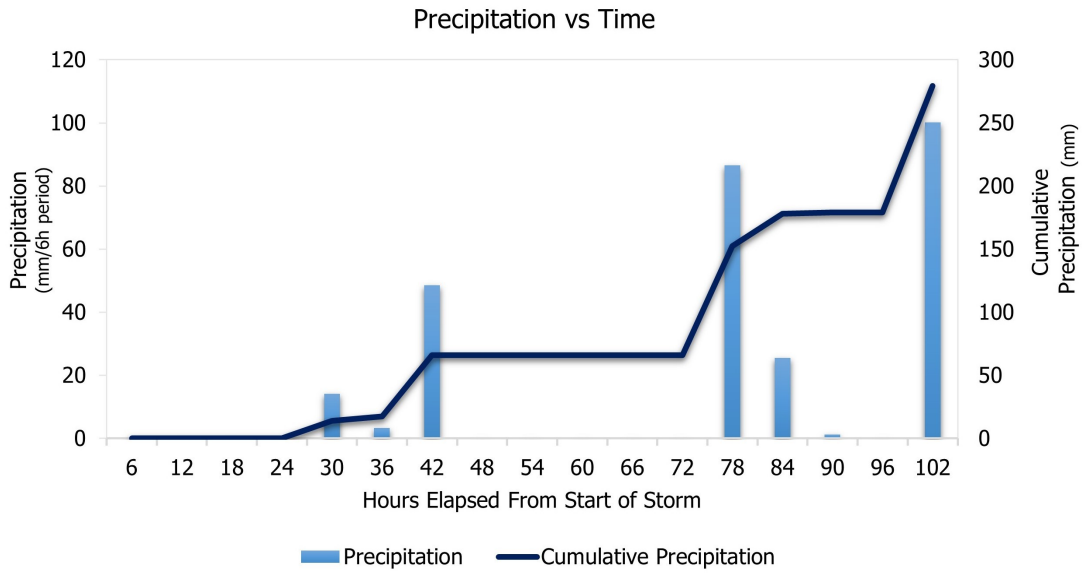

Figure 3.11: Precipitation vs Time for the 102-hour storm period.

From the spatial and landslide analysis, we know the spatial distribution of events and the volume of debris flow contributed by each sub-basin. Applying the proportions calculated from the TRIGRS output to the volume from each basin, which after accounting for entrainment as before, gives us the relative debris flow surge volumes for each time step as seen in Figure 3.12 when four basins are considered and in Figure 3.14 when seven basins are considered. The colours of the sub-basins correspond to the sub-basins seen in Figure 3.13 and Figure 3.15 for easy reference.

The basins in the intermediate and lowland areas are assumed to release in time step 16 $(90 - 96h)$ as is broadly consistent with the recorded time of the major debris flow event [45]. In Figure 3.12, the entire volume contribution from both Sub-Basins 3 and 4 or about 20% of the total debris flow volume is released at the end of the $96h$ period as TRIGRS fails to predict the variation of instability of the lowland region with time. Similarly, in Figure 3.14, the lowland region is covered by Sub-Basins 4 and 5, which are simulated the end of the $96h$ period along with flow volume from Sub-Basin 1, which, despite being in the highland region, is not predicted to fail by TRIGRS. Sub-Basin 1 contains three very large landslides, each greater than $13000m^3$. Consequently, the total debris flow volume contribution from the three Sub-Basins 1, 4 and 5 is about 40%, which is a significant share of the total debris flow volume and is consistent with reports of the major debris flow occurring close to this time [45]. The total modelled volume remains $2.6 \times 10^6 m^3$ as in the Spatial Analysis, which facilitates a comparison of the two methods.

3.3.2. Time-Resolved Scenario Analysis: Block Releases

Scenario 8 and 10 are based on Scenario 4, which is the spatially resolved scenario that considers four sub-basins (as seen in Figure 3.1c). The difference is that Scenario 8 accounts for surging by delaying the block releases of Scenario 4 in an order determined by Section 3.3.1 because this is the only difference between simulations we can directly compare Scenarios 4 and 8 to understand the effects of surging and answer the main research question. The same goes for Scenarios 9, 10 and 6, with Scenario 6 (as seen in Figure 3.1d) being the spatially resolved simulation that the time-resolved scenarios, Scenarios 9 and 11 are based upon. Scenarios 6 and 9 are directly comparable to understand the effects of surging and answer the main research question. The location and timing of the block releases are displayed for Scenarios 8 and 10 in 3.13 and for Scenarios 9 and 11 in Figure 3.15.

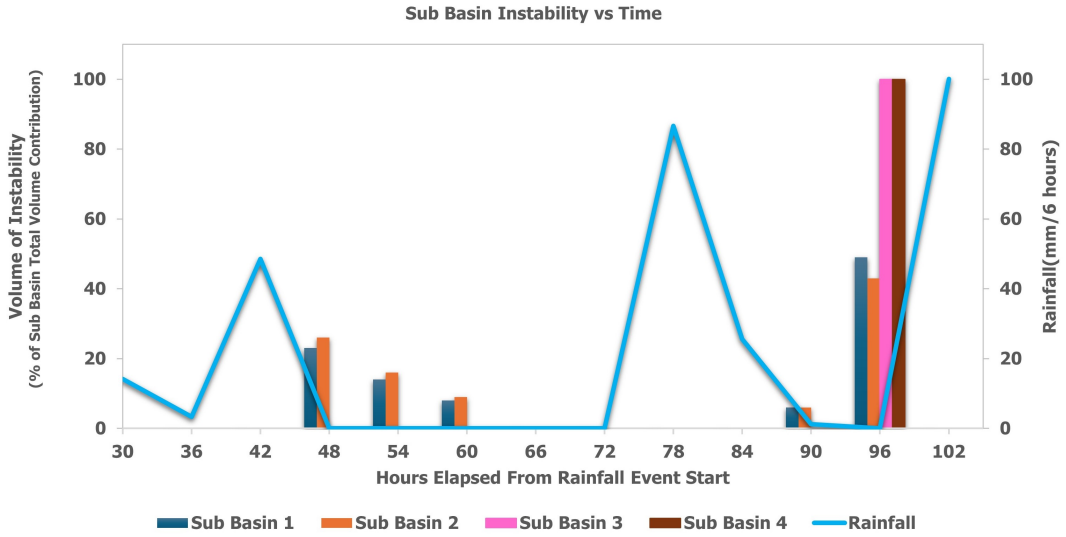

Figure 3.12: The distribution of debris flow volume as a response to rainfall over time and space when considering **four** sub-basins.

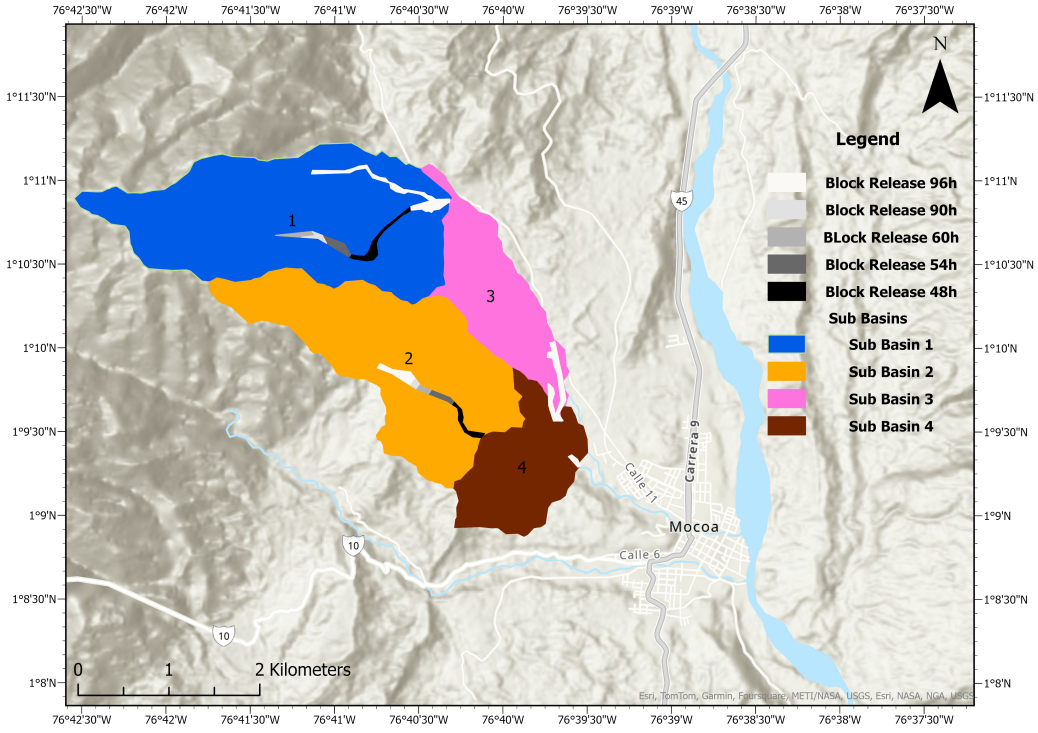

Figure 3.13: Block release locations of the time-resolved scenarios considering four sub-basins, Scenarios 8 and 10.

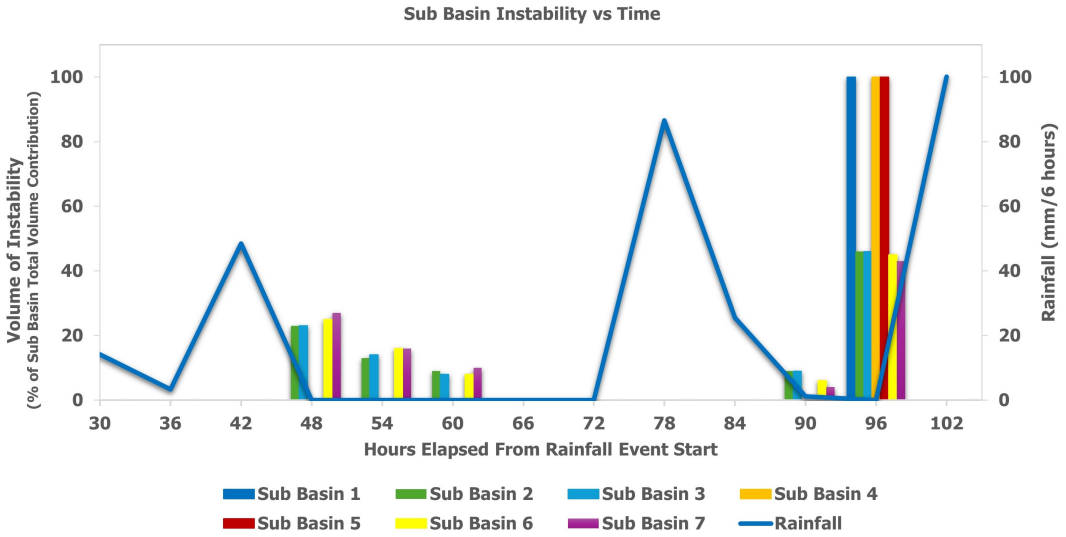

Figure 3.14: The distribution of debris flow volume as a response to rainfall over time and space when considering **seven** sub-basins.

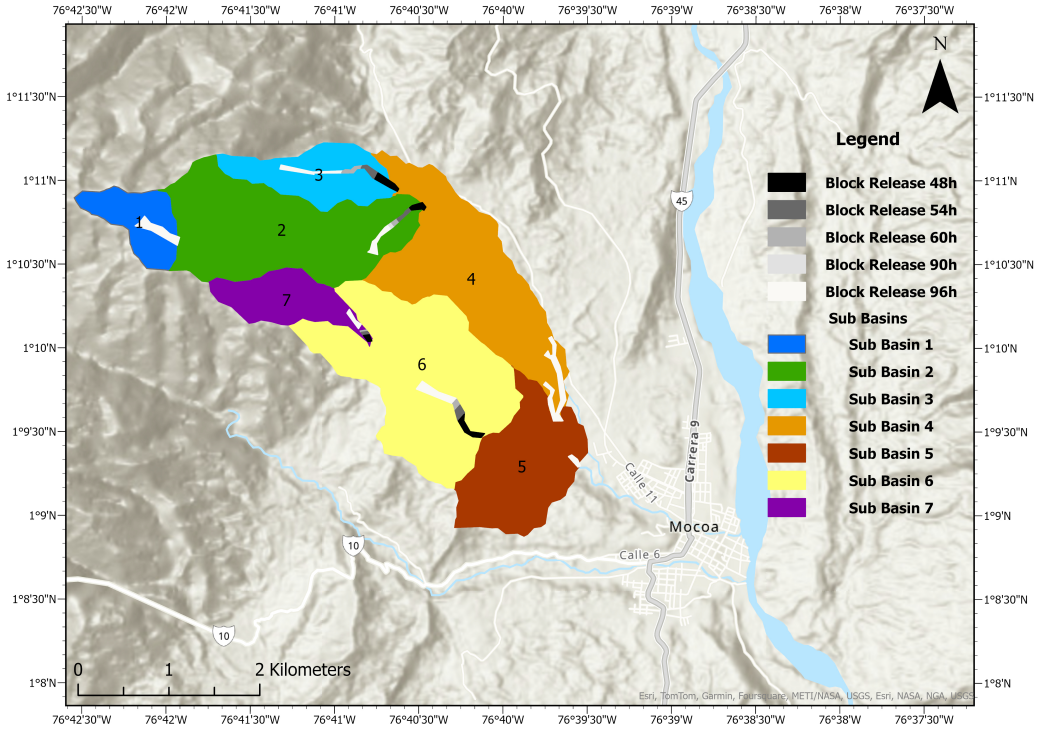

Figure 3.15: Block release locations of the time-resolved scenarios considering seven sub-basins, Scenarios 9 and 11.

Scenarios 8 and 10 are exactly the same, except that Scenario 8 accounts for the deposition of each surge by modifying the D.E.M. between each debris flow simulation, while Scenario 10 disregards deposition and does not modify the D.E.M. between surges. The same can be said of Scenarios 9 and 11, i.e. Scenario 9 accounts for deposition while Scenario 11 does not. This arrangement of scenarios is made to answer the sub-research question of the effects of accounting for the deposition of each surge on the runout simulation.

Time-Resolved Scenario Analysis: Maximum Simulated Runout Height

The maximum runout heights of Scenarios 8, 9, 10 and 11 are presented in Figure 3.16.

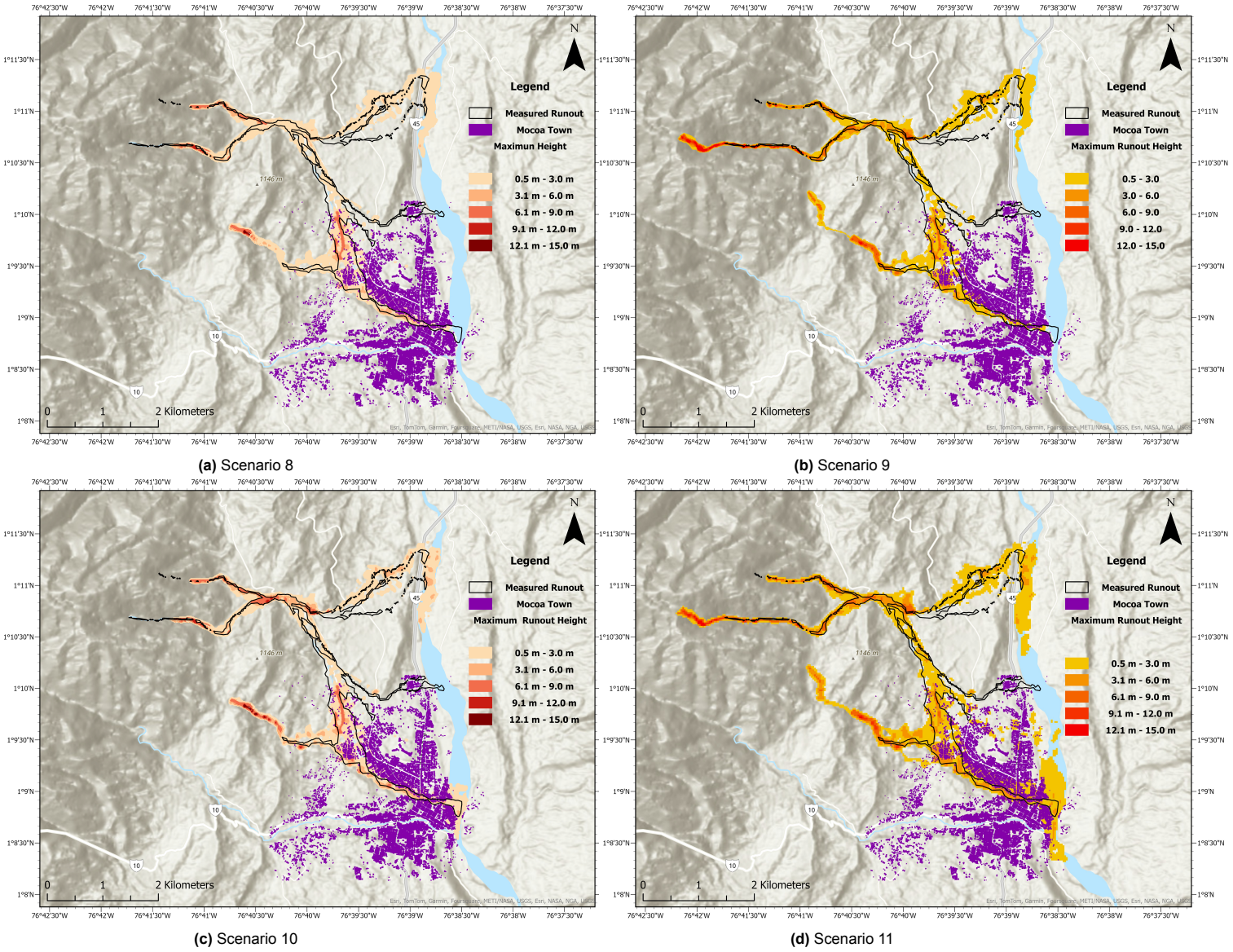

(a) Scenario 8 **(b)** Scenario 9

(c) Scenario 10 **(d)** Scenario 11

Figure 3.16: Maximum simulated runout heights of the four time-resolved scenarios. Scenarios 8 and 10 are based on four sub-basins and do and do not consider deposition, respectively. Scenarios 9 and 11 are based on seven sub-basins and do and do not consider deposition, respectively.

Upon initial examination, there is little to no difference between Scenario 8 in Figure 3.16a and Scenario 10 in Figure 3.16c. The same can be said of Scenarios 9 and 11 in Figure 3.16b and Figure 3.16d, respectively. However, the scenarios that do not consider deposition, Scenarios 10 and 11, show slightly greater discharge into the Mocoa River in Figure 3.16c and Figure 3.16d, respectively, compared to Scenarios 8 and 9 in Figure 3.16a and Figure 3.16b, respectively, which do consider deposition. Scenarios 8 and 9 are based on four and seven sub-basins, respectively. With Scenario 9 simulating the initial paths of the the measured runout better than Scenario 8 as it has block releases starting further upstream. The deposition could be interrupting the flow to a minor extent. This difference is quantified later in Section 4.2.

Time-Resolved Scenario Analysis: Maximum Simulated Runout Velocity

The maximum runout velocities of Scenarios 8, 9, 10 and 11 are presented in Figure 3.17.

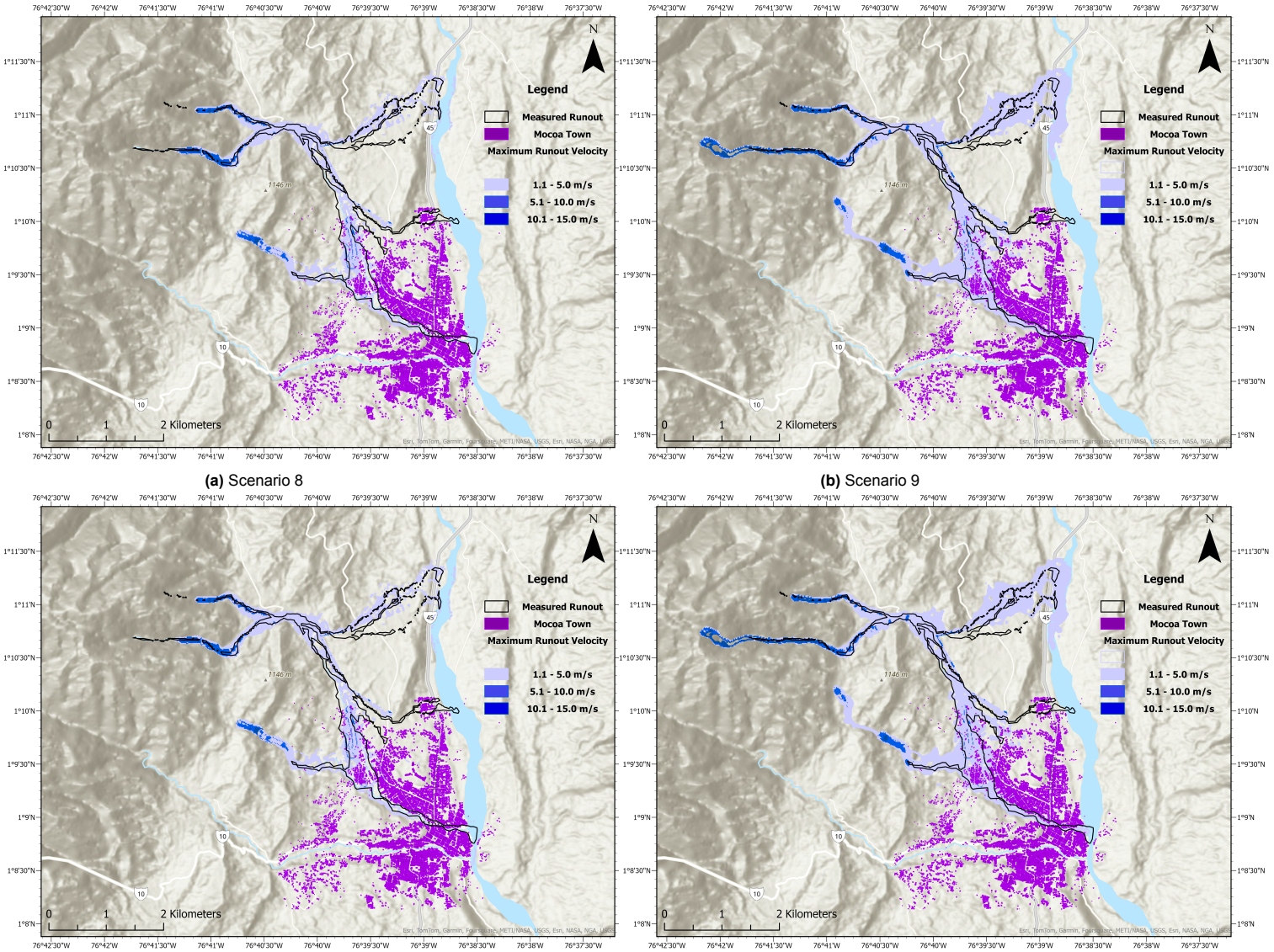

(a) Scenario 8 **(b)** Scenario 9

(c) Scenario 10 **(d)** Scenario 11

Figure 3.17: Maximum simulated runout velocities of the four time-resolved scenarios.

By visual inspection, there is no discernible difference between Scenario 8 and 10 as well as between that of Scenarios 9 and 11 seen in Figure 3.17. Scenarios 8 and 9 are based on four and seven sub-basins, respectively. With Scenario 9 simulating the initial velocity of the the measured runout further upstream of Scenario 8. In the next chapter the measured velocities will be inspected closer to see if deposition has an effect on velocities at the reference sections.

3.4. Simulation Numerical Volume Loss

As part of the approximation made during the numerical integration procedure in RAMMS, which is outlined in Sub-Sub-Section 2.3.3, some loss of volume is expected. This is shown in Table 3.1 for all scenarios. All the time-resolved scenarios of Scenarios 8 to 11 have higher volume losses than the spatially resolved scenarios, as each time-resolved scenario consists of five simulations, one for each debris flow surge. The very low volume loss percentages seen in the last column of Table 3.1 indicate that numerical volume losses for all scenarios are negligible.

Table 3.1: Numerical Volume Losses.

Scenario	Numerical Volume Loss (m^3)	Modelled Volume (m^3)	Volume Loss (%)
1	315.09	2.6×10^6	0.012
2	393.03	2.1×10^6	0.018
3	309.13	2.6×10^6	0.011
4	316.11	2.6×10^6	0.012
5	298.47	2×10^6	0.014
6	236.48	2.6×10^6	0.009
7	169.43	2.1×10^6	0.008
8	964.03	2.6×10^6	0.037
9	1330.66	2.6×10^6	0.051
10	1349.48	2.6×10^6	0.051
11	2170.15	2.6×10^6	0.083

4

Results and Discussion

The results of the analysis are presented in three parts. The first part, Section 4.1, presents the Spatial Analysis results where the debris flow is simulated in seven scenarios that vary the source areas considered as seen in Table 2.4. Four of these seven scenarios, namely, Scenarios 1, 3, 4, and 6, are introduced in Sub Section 4.1.1 and consider the entire source area. They were designed to answer the main research question regarding debris flow surges, the first sub-question regarding the performance of the spatial resolution of source areas, and the second sub-question examining the feasibility of using the exact location of landslides in the simulation. The other three scenarios, Scenarios 2, 5, and 7, consider only the highland region and are presented in Sub Section 4.1.2. This division of scenarios is made to better answer the third sub-research question regarding the sufficiency of only considering the highland area versus the entire source area. The second part of the analysis, Section 4.2 presents the results of the four time-resolved scenarios, Scenarios 8, 9, 10, and 11 as seen in Table 2.4. These four scenarios answer the main research question regarding debris flow surges and the fourth and final sub-question concerning the effect of surge deposition on runout. Finally, part three of the results, Section 4.3 compares the results of the best performing spatial and time-resolved scenarios, namely, Scenarios 4, 6, 8, and 9. This comparison is made to answer the main research question as it compares the performance of scenarios that include debris flow surges (the time-resolved scenarios) to those that neglect debris flow surges (the spatially resolved scenarios). The results are discussed in Section 4.4, and the limitations of this study are declared in Section 4.5.

4.1. Spatially Resolved Results

The Spatially Resolved Results are presented in two parts, Sub Section 4.1.1, which contains the results of Scenarios 1, 3, 4, and 6 of the whole source area and Sub Section 4.1.2, which presents the results of Scenarios 2,5, and 7 of the highland source area.

4.1.1. Spatially Resolved Whole Source Area Results

This section presents the results of all the spatially resolved scenarios that consider the whole source area, namely Scenarios 1, 3, 4, and 6. Scenario 1 has the highest spatial resolution as it was simulated using the exact individual landslide release areas. Scenario 3 has the lowest spatial resolution as it considers the whole source area as a single basin. Scenarios 4 and 6 divide the area into four and seven sub-basins, respectively, resulting in a spatial resolution between that of Scenarios 1 and 3. These scenarios go, in part, to answering the main research question concerning surging as well as the first and second sub-research questions regarding the effect of spatial resolution and the highland area on runout simulation.

Area Ratios

The two area ratios of Area Coverage and Area Outrun are presented below in Figures 4.1a and 4.1b, respectively, for the whole source area scenarios.

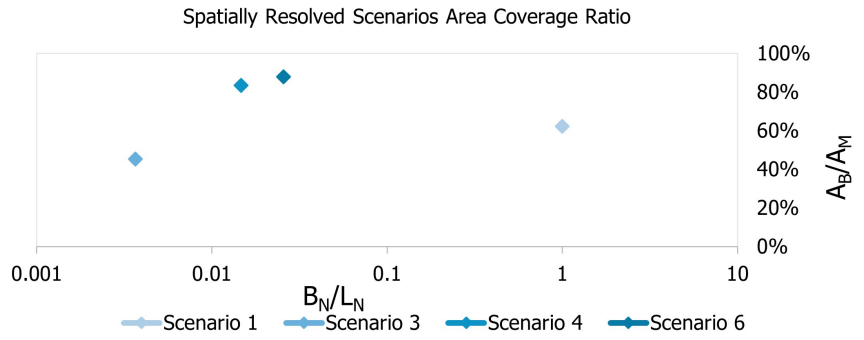

(a) Area Coverage Ratio

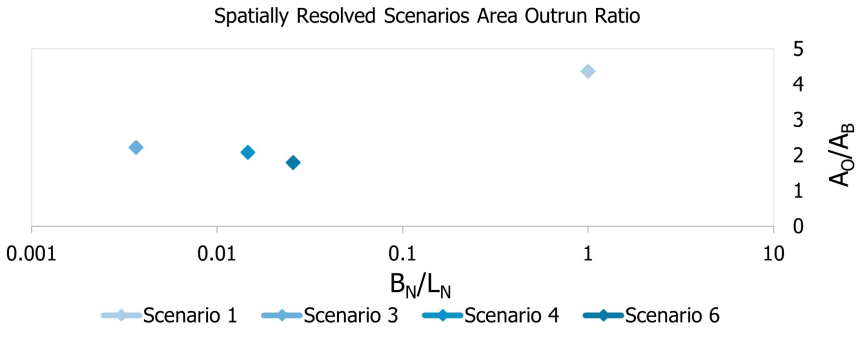

(b) Area Outrun Ratio

Figure 4.1: Area coverage and outrun ratios for the spatially resolved scenarios considering the whole source area.

Scenario 1 has the highest spatial resolution with a $\frac{B_N}{L_N}$ of 1. However, it produces a low $\frac{A_B}{A_M}$ of 60% as seen in Figure 4.1a and a very high $\frac{A_O}{A_B}$ of 4.4 as seen in Figure 4.1b making it a very poor reproduction of events as it is both inaccurate and imprecise. Scenario 3 has a $\frac{A_B}{A_M}$ value of 45% as seen in Figure 4.1a, which is the lowest of all four scenarios but with a $\frac{A_O}{A_B}$ of 2.2 as seen in Figure 4.1b it is more precise than Scenario 1 which has a $\frac{A_O}{A_B}$ of 4.4. Scenarios 4 and 6 are the best-performing scenarios with a $\frac{A_B}{A_M}$ of 83% and 88%,respectively as seen in Figure 4.1a and a $\frac{A_O}{A_B}$ of 2.0 and 1.8, respectively as seen in Figure 4.1b . Making them both the most accurate and precise of all scenarios in this study.

Width at Sections

The $\frac{S_W}{M_W}$ ratio is presented below in Figure 4.2 at all three sections of interest for the whole source area scenarios.

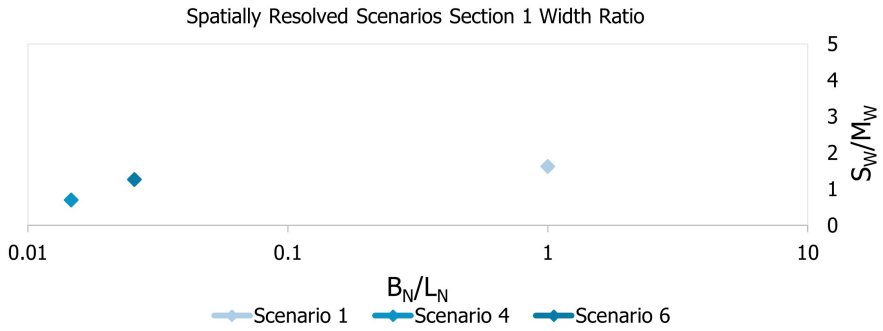

(a) Section 1

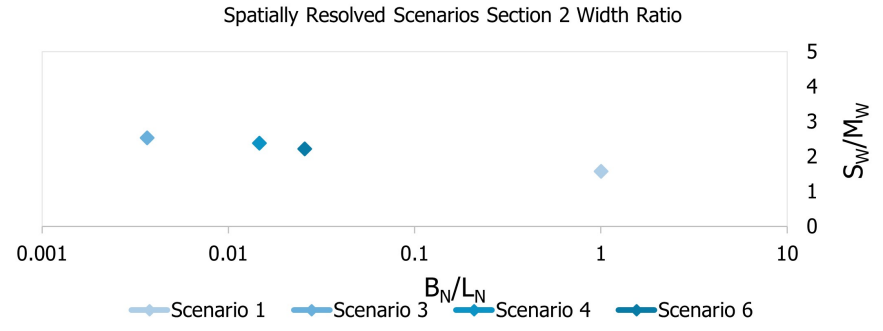

(b) Section 2

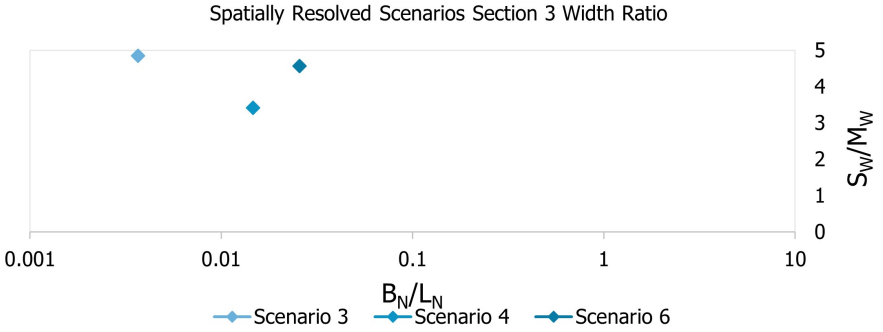

(c) Section 3

Figure 4.2: Width ratios at the three critical sections for the spatially resolved scenarios considering the whole source area.

In Figure 4.2a at Section 1, Scenario 1 overestimates the width by a factor of 1.6. With a $\frac{S_W}{M_W}$ value of 1.2, Scenario 4 provides the best estimate, and Scenario 6 underestimates the width with a $\frac{S_W}{M_W}$ of 0.7. The flow in Scenario 3 is initiated after this section, so it does not appear in the graph. In Figure 4.2b at Section 2, Scenario 1 provides the same estimate of the width as it did in Section 1, but Scenarios 3,4 and 6 overestimate the width by a $\frac{S_W}{M_W}$ value of 2.5, 2.3, and 2.2 respectively. In Figure 4.2c at Section 3, the flow from Scenario 1 does not reach this section. Scenario 3 shows a large overestimation of width with a $\frac{S_W}{M_W}$ of 4.8 followed by Scenarios 6 and 4 with a $\frac{S_W}{M_W}$ value of 4.5 and 3.4 respectively. There is no clear trend between simulated width ratio ($\frac{S_W}{M_W}$) and spatial resolution represented by the release ratio($\frac{L_N}{B_N}$) in these scenarios.

Velocity at Sections

For the whole area scenarios, the $\frac{V_S}{V_C}$ ratio is plotted in Figure 4.3a at Section 1 and the simulated velocity V_S is plotted in Figures 4.3b and 4.3c at Sections 2 and 3, respectively.

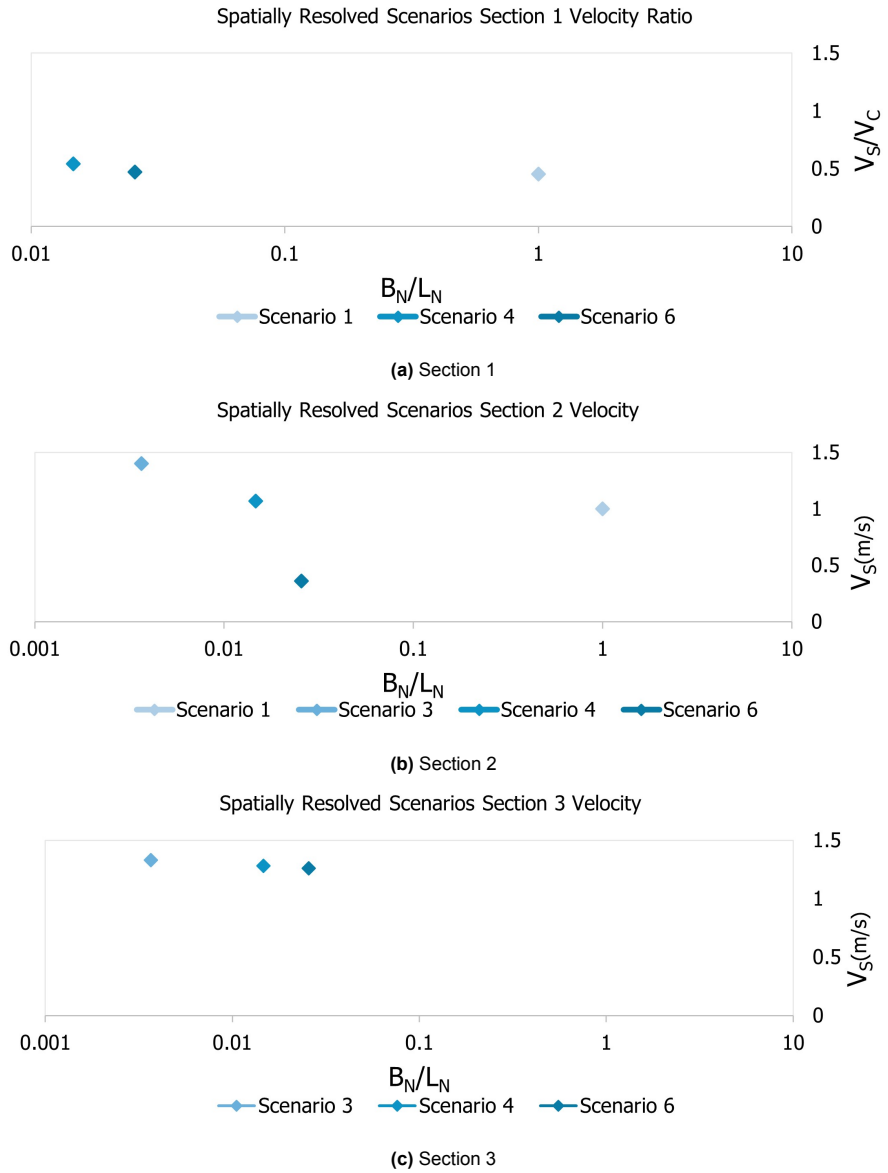

(a) Section 1

(b) Section 2

(c) Section 3

Figure 4.3: Velocity at the three critical sections for the spatially resolved scenarios considering the whole source area.

In Figure 4.3a at Section 1, all scenarios under predict velocity by a factor of about 0.5. In Figures 4.3b 4.3c at Section 2 and Section 3, respectively, all scenarios predict a velocity between $1m/s$ to $1.5m/s$ except for Scenario 6 at Section 2, which simulates a velocity of $0.4m/s$, this appears to be an outlier.

4.1.2. Spatially Resolved Highland Source Area Results

This section presents the results of Scenarios 2, 5, and 7, which consider only the highland source area. Scenario 2 utilises the mapped landslide areas as initiation zones and, therefore, has the highest spatial resolution of all highland scenarios with a $\frac{B_N}{L_N}$ value of 1.8. Scenarios 5 and 7 divide the source area into 4 and 7 basins, respectively, but consider only the highland sources. Scenarios 2, 5, and 7 are essentially subsets of Scenarios 1, 4, and 6 seen in the previous section. These scenarios are used to answer the third sub-research question concerning the feasibility of only analysing the highland source area.

Area Ratios

The two area ratios of Area Coverage and Area Outrun are presented in Figures 4.4a and 4.4b, respectively, for the highland source area scenarios.

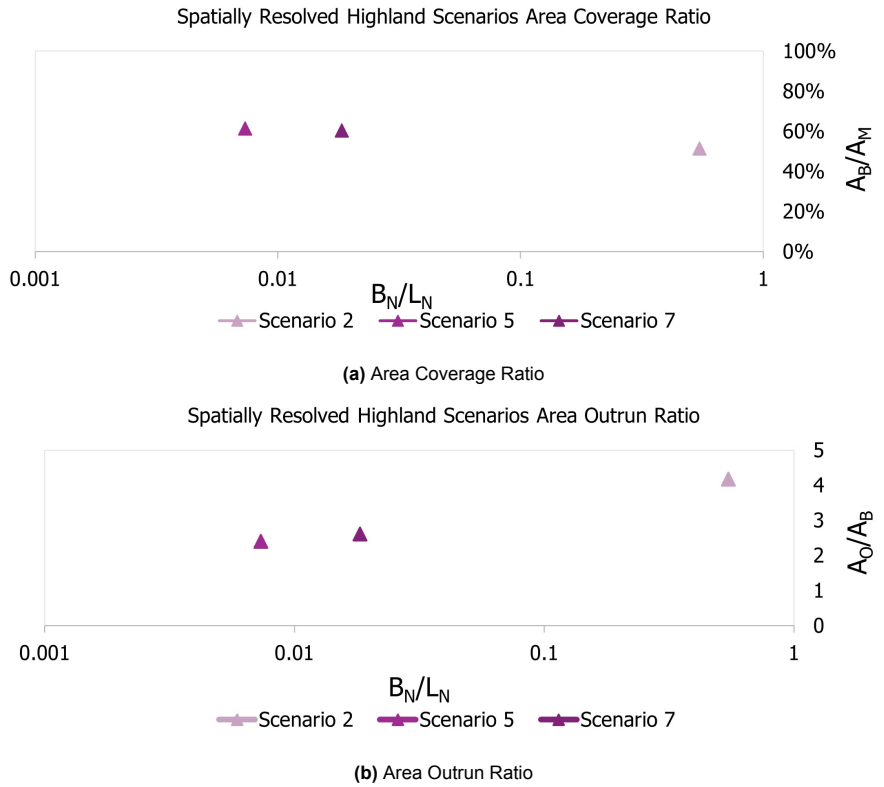

(a) Area Coverage Ratio

(b) Area Outrun Ratio

Figure 4.4: Area coverage and outrun ratios for the spatially resolved scenarios considering the highland source area.

In Figure 4.4a at Section 1, the $\frac{A_B}{A_M}$ value of Scenarios 5 and 7 is consistent at 62% and 61%, respectively while Scenario 2 is lower at 52%. Scenario 2 has a much higher $\frac{A_O}{A_B}$ value of 4 with Scenarios 5 and 7 again having similar values of $\frac{A_O}{A_B}$ of 2.4 and 2.6 respectively. This indicates that the approximated block release is more accurate and precise than the exact landslide block release, except for Scenario 3, which has the lowest spatial resolution of all scenarios (single basin). Therefore, spatially resolved scenarios that consider only the highland source area (Scenarios 2, 5 and 7) have lower accuracy and precision than the corresponding spatially resolved scenarios that consider the whole source area (Scenarios 1, 4 and 6), as seen in Sub Section 4.1.1.

Width at Sections

The $\frac{S_W}{M_W}$ ratio is presented below in Figure 4.5 at all three sections of interest for the highland source area scenarios.

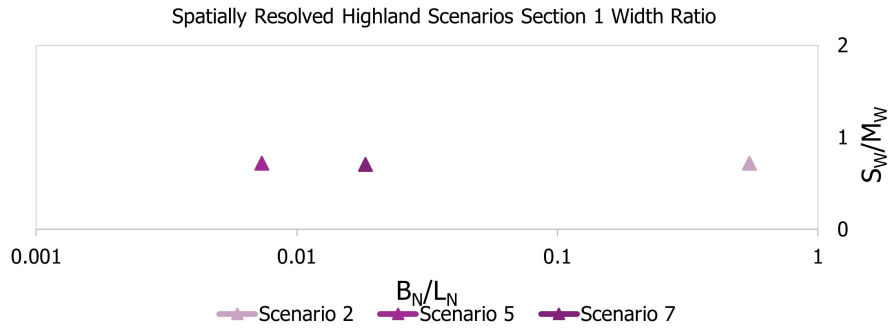

(a) Section 1

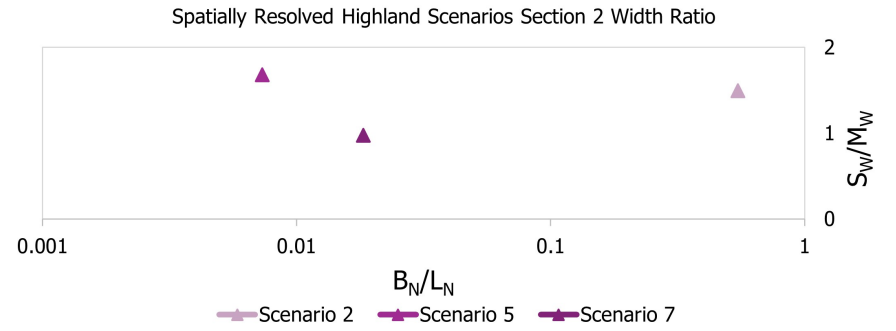

(b) Section 2

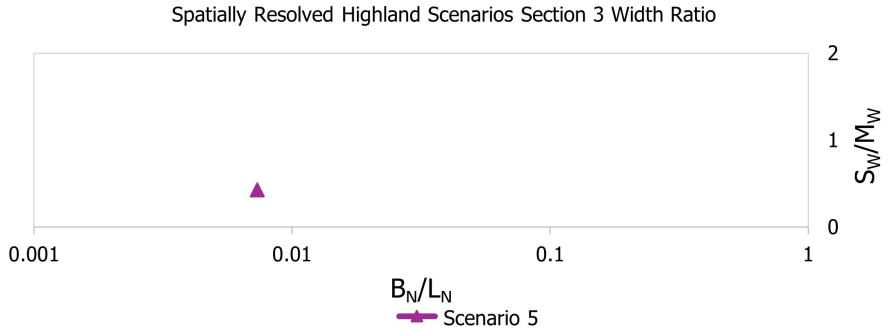

(c) Section 3

Figure 4.5: Width ratios at the three critical sections for the spatially resolved scenarios considering the highland source area.

In Figure 4.5a at Section 1, The $\frac{S_W}{M_W}$ value of all scenarios is remarkably consistent ranging from 0.70 to 0.72. A larger difference in $\frac{S_W}{M_W}$ values is seen after the flow encounters infrastructure and reaches Section 2 as seen in Figure 4.5b with values ranging from 1.7 to 0.97, showing the influence of infrastructure on flow paths. Scenario 7 provides a very accurate estimate of width achieving a $\frac{S_W}{M_W}$ value of 0.97 as seen in Figure 4.5b. In Figure 4.5c at Section 3, only Scenario 5 records a flow, simulating a narrow width resulting in a $\frac{S_W}{M_W}$ value of 0.43 reflecting the lower volume of flow compared to the actual event as a result of disregarding source areas outside of the highland area.

Velocity at Sections

For the highland area scenarios, the $\frac{V_S}{V_C}$ ratio is plotted in Figure 4.6a at Section 1 and the simulated velocity V_S is plotted in Figures 4.6b and 4.6c at Sections 2 and 3, respectively.

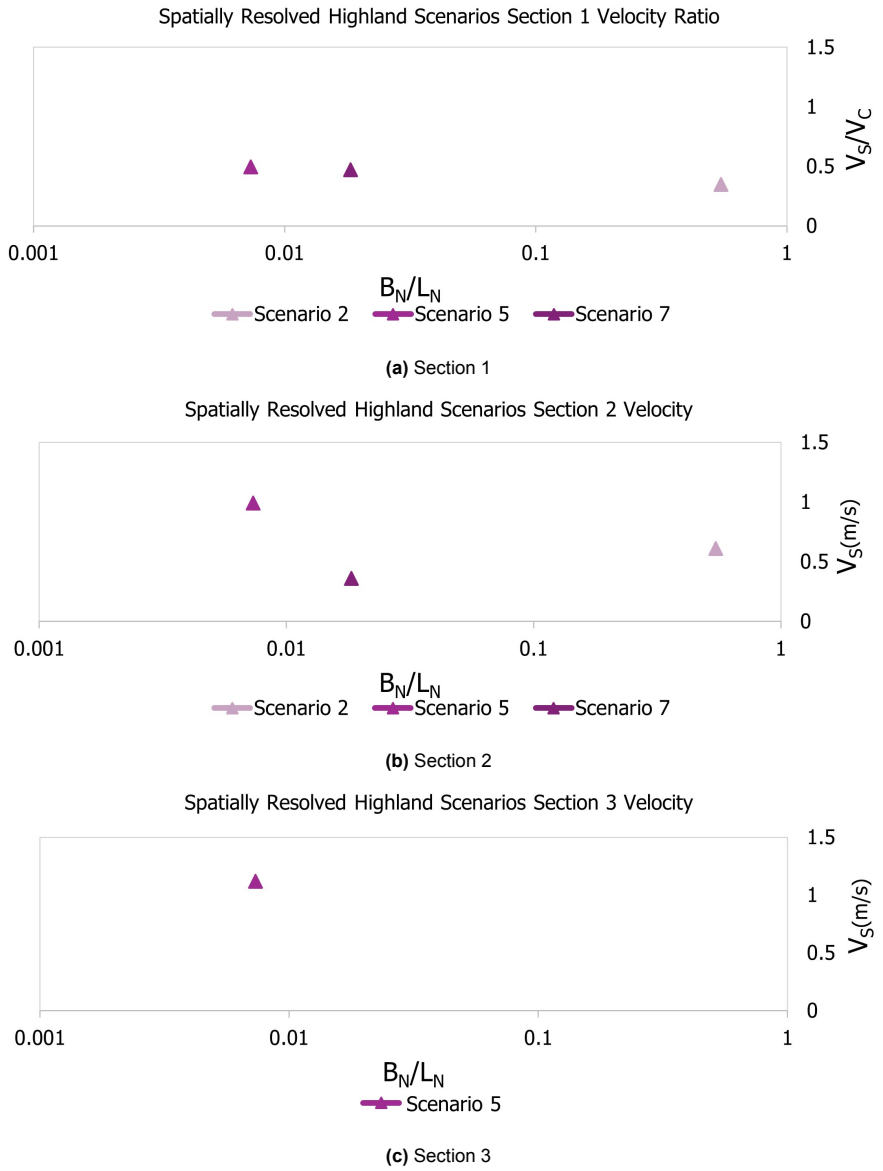

(a) Section 1

(b) Section 2

(c) Section 3

Figure 4.6: Velocity at the three critical sections for the spatially resolved scenarios considering the highland source area.

In Figure 4.6a at Section 1, the $\frac{V_S}{V_C}$ values are 0.35, 0.49, and 0.47 for Scenarios 2, 5, and 7, respectively, mirroring the uniformity in width predictions at this section. More variation is seen Figure 4.6b at Section 2, with Scenario 5 recording a velocity of $1m/s$ while Scenario 7 only predicts a velocity of $0.36m/s$, Scenario 2 lies between the other two scenarios (5 and 7) with a velocity of $0.61m/s$. This is explained by the fact that some of the block releases in Scenario 7 are further away from this section than those of Scenarios 5 and 2, which means the flow travels a longer path and is subject to more deceleration. Only Scenario 5 is recorded at Section 3, as seen in Figure 4.6c with a velocity of $1m/s$, as the other scenarios terminate before Section 3.

4.2. Time-Resolved Results

Scenarios 8, 9, 10, and 11 are the time-resolved scenarios. They take into account debris flow surging, with only Scenarios 8 and 9 accounting for deposition between surges. Scenario 10 is a variant of Scenario 8. They are alike in all respects, except Scenario 10 disregards the deposition of flow between surges. The same relation exists between Scenarios 9 and 11, with Scenario 9 accounting for surge deposition and Scenario 11 disregarding deposition. Scenarios 8 and 10 are based on the four sub-

basin spatial resolution of Scenario 4. While Scenarios 9 and 11 are based on the seven sub-basin spatial resolution of Scenario 6.

Area Ratios

The two area ratios of Area Coverage and Area Outrun are presented in Figures 4.7a and 4.7b, respectively, for the time-resolved scenarios.

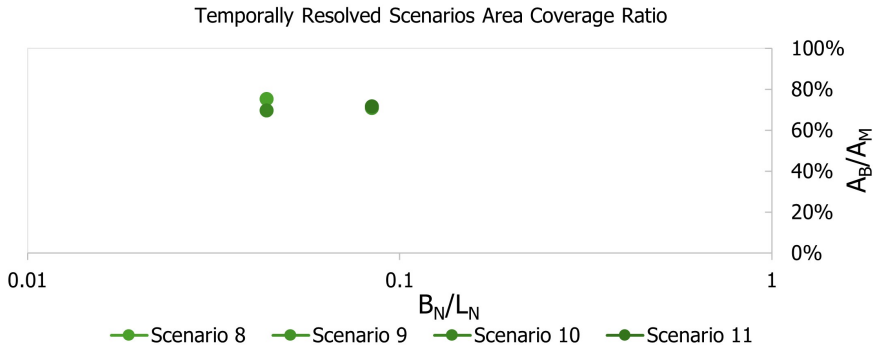

(a) Area Coverage Ratio

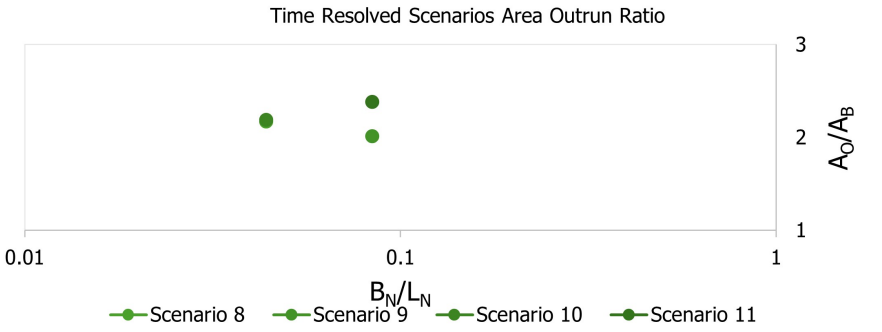

(b) Area Outrun Ratio

Figure 4.7: Area coverage and outrun ratios for the time-resolved scenarios .

In Figure 4.7a, the Area Coverage Ratios ($\frac{A_B}{A_M}$) of all four scenarios are remarkably consistent with Scenarios 9 and 11, showing minimal variation by almost completely overlapping. Scenarios 8 and 10 also overlap, but to a lesser degree in Figure 4.7a. Scenarios 8 and 10 only differ $\frac{A_B}{A_M}$ values by 5%. The Area Outrun Ratio seen in Figure 4.7b is also very consistent between scenarios, with Scenarios 8 and 10 exhibiting a negligible difference as seen by their overlap when plotted and Scenarios 9 and 11 differing marginally by 18% with a $\frac{A_O}{A_B}$ of 2.01 and 2.38 respectively. The uniformity of area ratios indicates that accounting for deposition does not appreciably affect the accuracy and precision of the simulated runout.

Width at Sections

The $\frac{S_W}{M_W}$ ratio is presented below in Figure 4.8 at all three sections of interest for the time-resolved scenarios.

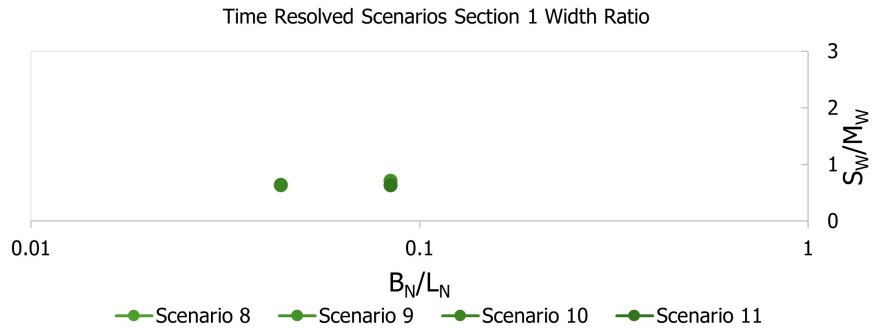

(a) Section 1

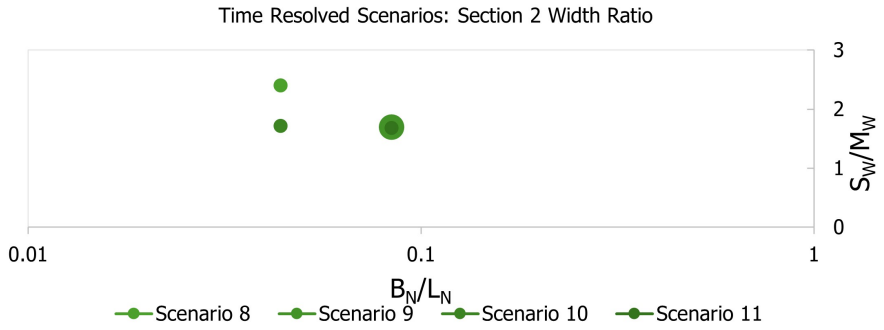

(b) Section 2

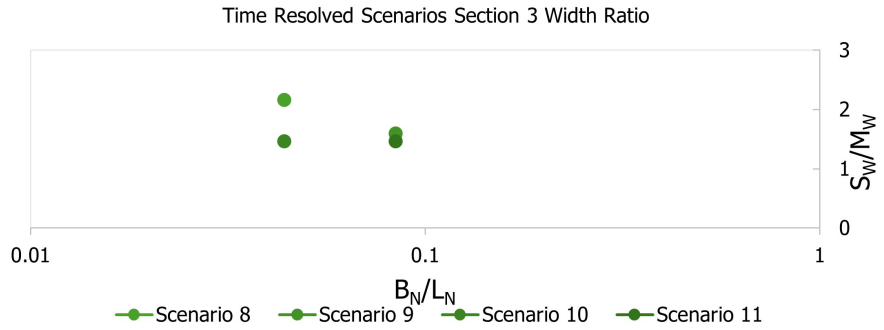

(c) Section 3

Figure 4.8: Width ratios at the three critical sections for the time-resolved scenarios .

In Figure 4.8a at Section 1, the value of $\frac{S_W}{M_W}$ is consistent across scenarios with a value of approximately 0.6 showing an under prediction of width. In Figure 4.8b and Figure 4.8c at Sections 2 and 3, respectively, the consistency between scenarios is reduced with $\frac{S_W}{M_W}$ ranging from 2.4 to 1.7 across scenarios at Section 2 and 2.5 to 1.46 at Section 3 showing the effect of infrastructure on introducing variability to flow width prediction as the debris flow proceeds from Section 1 through to Section 3.

Velocity at Sections

For the time-resolved scenarios, the $\frac{V_S}{V_C}$ ratio is plotted in Figure 4.9a at Section 1 and the simulated velocity V_S is plotted in Figures 4.9b and 4.9c at Sections 2 and 3, respectively.

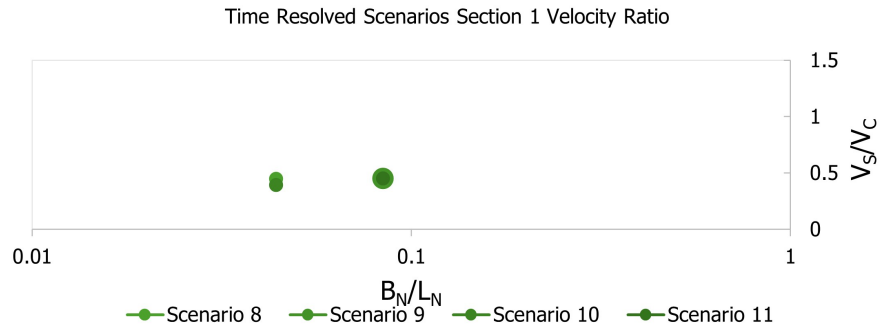

(a) Section 1

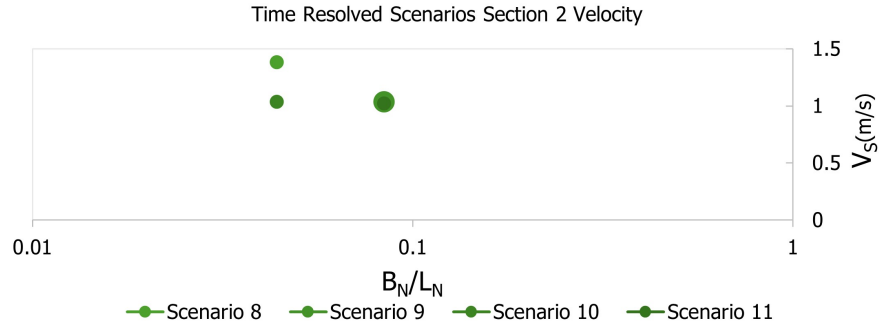

(b) Section 2

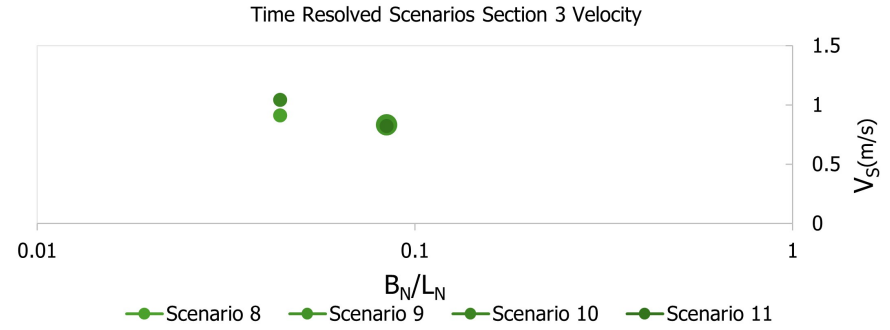

(c) Section 3

Figure 4.9: Velocity at the three critical sections for the time-resolved scenarios.

In Figure 4.9a at Section 1, the velocity is under-predicted across all scenarios with a $\frac{V_S}{V_C}$ value of approximately 0.45 for Scenarios 9 and 11 and 0.40 for Scenarios 8 and 10. In Figure 4.8b and Figure 4.8c at Sections 2 and 3, respectively, the velocities show a slight reduction between sections, maintaining a steady flow of about 1 to $1.4m/s$ for each scenario.

4.3. Comparison of Spatially and Time-Resolved Results

This comparison includes the best-performing scenarios of the spatially resolved analysis, Scenarios 4 and 6, as determined in the previous sections and the best-performing scenarios of the time-resolved analysis, Scenarios 8 and 9. A direct comparison is made between Scenarios 4 and 8 as they are both based on the same spatial resolution, four sub-basins and differ only based on their time resolution of events, where Scenario 4 disregards surging and Scenario 8 accounts for the phenomenon of surging. The same comparison can be made between Scenarios 6 and 9 as they are both based on the seven sub-basin spatial resolution, with Scenario 6 disregarding surging and Scenario 9 being time-resolved, accounts for surging.

Area Ratios

The two area ratios of Area Coverage and Area Outrun are presented in Figures 4.10a and 4.10b, respectively, for the spatially resolved scenarios of Scenarios 4 and 6, along with the time-resolved scenarios of Scenarios 8 and 9.

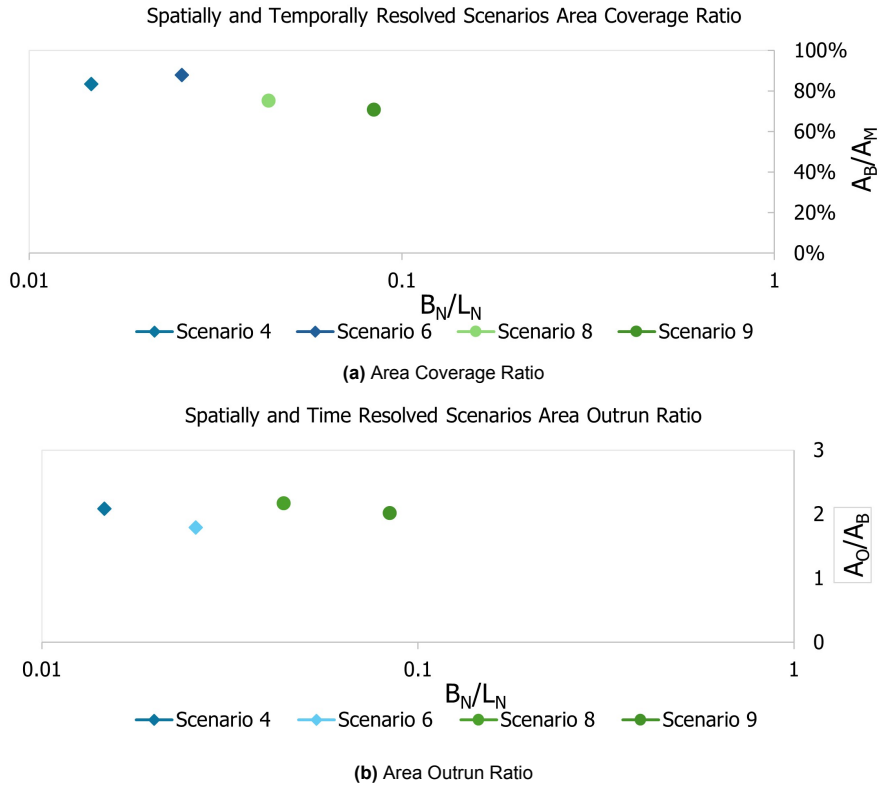

(a) Area Coverage Ratio

(b) Area Outrun Ratio

Figure 4.10: Comparing the area coverage and outrun ratios for the spatially and time-resolved scenarios.

Comparing the spatially and time-resolved scenarios, it is observed in Figure 4.10a that the Spatially Resolved Scenarios of 4 and 6 have higher $\frac{A_B}{A_M}$ ratios with 83% and 88%, respectively compared to 71% and 75% for Scenarios 8 and 9, respectively. In Figure 4.10b, the spatially resolved scenarios also perform marginally better when it comes to the Area Outrun ratio with a $\frac{A_O}{A_B}$ of 1.8 and 2 for Scenarios 4 and 6, respectively. Compared to a $\frac{A_O}{A_B}$ of 2.0 and 2.1 for Scenarios 8 and 9, respectively. Overall the spatially resolved scenarios perform better than the time-resolved scenarios on both area ratio metrics.

Width at Sections

The $\frac{S_W}{M_W}$ ratio is presented below in Figure 4.11 at all three sections of interest for the spatially resolved scenarios of Scenarios 4 and 6, along with the time-resolved scenarios of Scenarios 8 and 9.

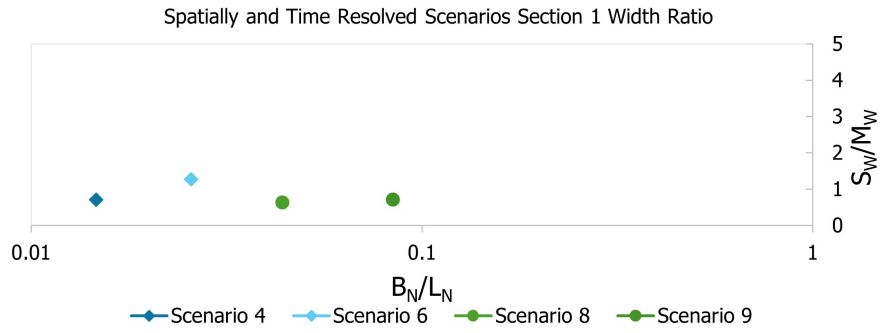

(a) Section 1

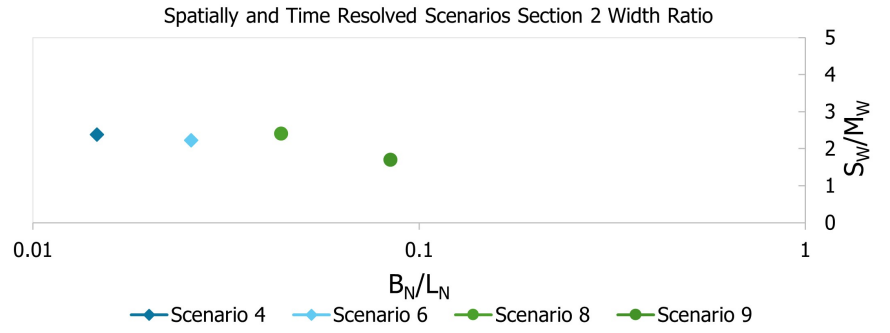

(b) Section 2

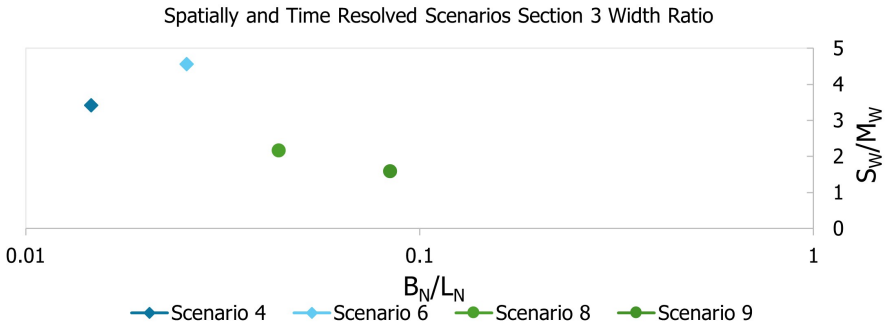

(c) Section 3

Figure 4.11: Comparing the width ratios at the three critical sections for the spatially and time-resolved scenarios .

In Figure 4.11a at Section 1, Scenarios 6, 8 and 9 predict approximately 70% of the actual width with Scenario 4 over-predicting the width by 20%. In Figure 4.11b at Section 2, all scenarios over-predict the width with values ranging from 1.7 to 2.4 for Scenario 9 and 4, respectively. In Figure 4.11c at Section 3, all scenarios over predict width, but the time-resolved scenarios of 8 and 9 have a $\frac{S_W}{S_M}$ of 1.6 and 2.1 which are significantly better than the spatially resolved scenarios of 4 and 6 with a $\frac{S_W}{S_M}$ of 4.5 and 3.4 respectively. Overall the prediction of width at Scenario 1 where infrastructure has little influence over the flow path is better than the predictions at the other two sections where infrastructure is more prevalent. The time-resolved scenarios show a lower value of $\frac{S_W}{S_M}$ across all sections as well as a lower variation of $\frac{S_W}{S_M}$ making the time-resolved scenarios more consistent and better at simulating the width at all three sections. This could be due to the lower volumes flowing in the channel at any given time, which results in a narrower flow for the time-resolved scenarios.

Velocity at Sections

For the spatially resolved scenarios of Scenarios 4 and 6 and the time-resolved scenarios of Scenarios 8 and 9, the $\frac{V_S}{V_C}$ ratio is plotted in Figure 4.12a at Section 1 and the simulated velocity V_S is plotted in Figures 4.12b and 4.12c at Sections 2 and 3, respectively.

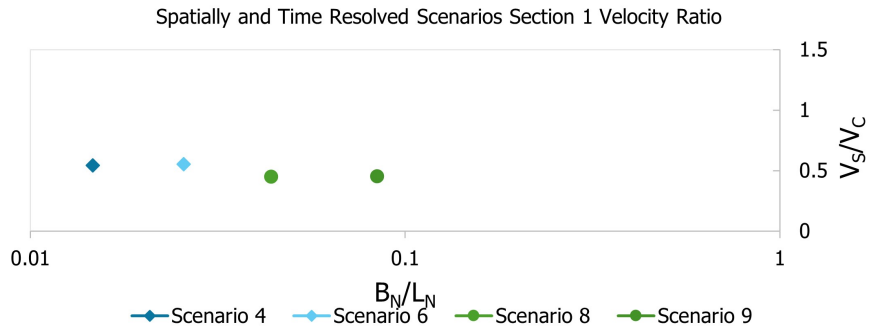

(a) Section 1

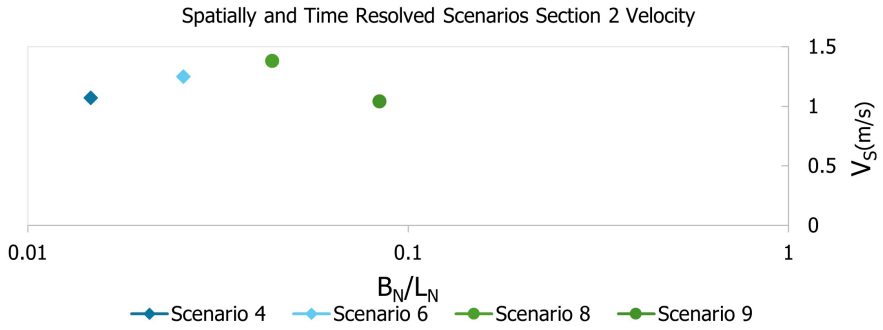

(b) Section 2

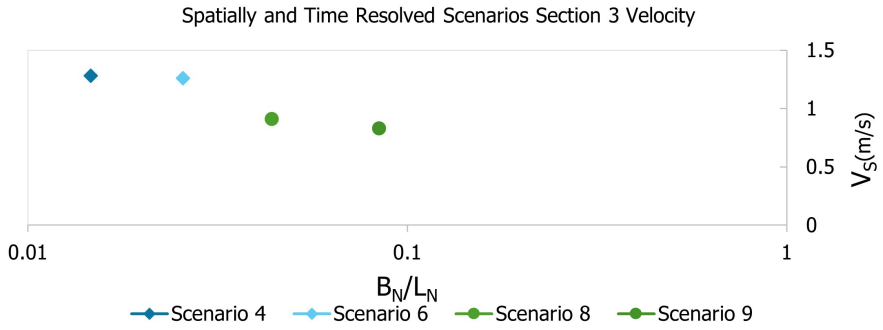

(c) Section 3

Figure 4.12: Comparing velocity at the three critical sections for the spatially and time-resolved scenarios.

In Figure 4.12a at Section 1, $\frac{V_S}{V_C}$ is uniformly predicted to be approximately 0.5 of the estimated value across all scenarios. In Figure 4.12b at Section 2, there is minor variation in terms of predicted velocities, with Scenario 8 estimating the highest V_S of $1.4m/s$ and Scenario 9 the lowest V_S of $1m/s$ across all scenarios. A similar variation is seen between the spatially resolved scenarios. In Figure 4.12c at Section 3, the spatially resolved scenarios estimate a higher V_S than the time-resolved scenarios with an average spatially resolved V_S of $1.27m/s$ and a time-resolved V_S of $0.87m/s$. Overall predicted velocities are lower than calculated velocities across all sections regardless of whether surging is considered.

4.4. Summary of Results and Research Answers

A summary of the key performance metrics of area coverage and area outrun ratios for all eleven scenarios is provided below in Figure 4.13 and Figure 4.14, respectively.

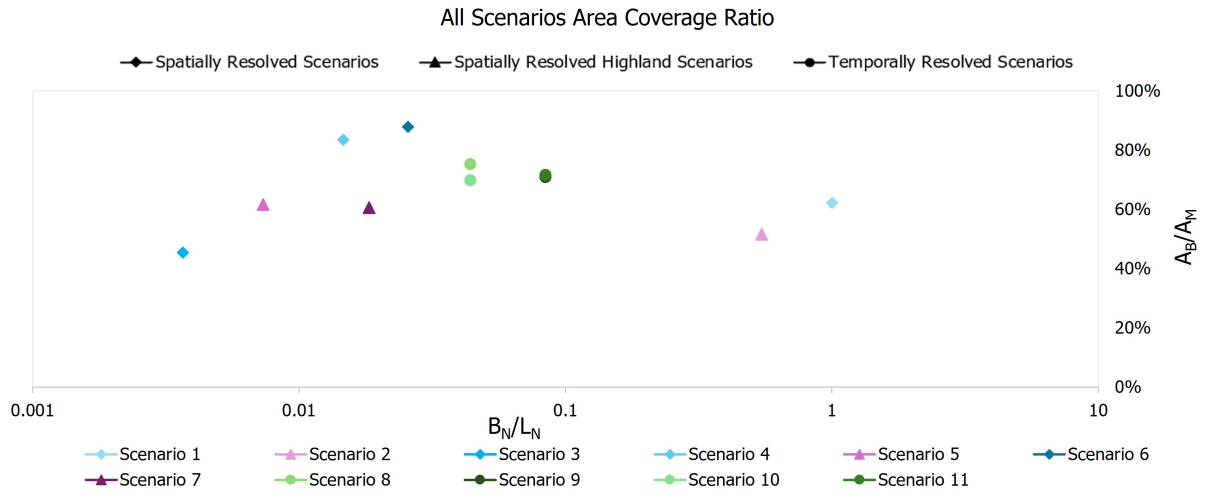

Figure 4.13: Area Coverage ratio for all scenarios.

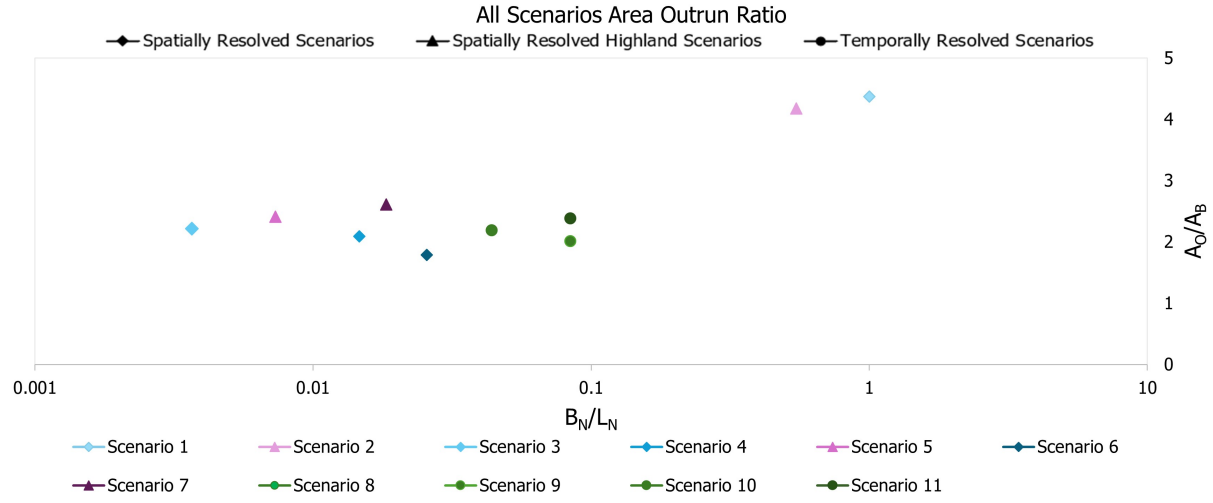

Figure 4.14: Area Outrun ratio for all scenarios.

The research questions are addressed in the following paragraphs,

In Section 4.3, it is found that on the basis of the two area ratios, the time-resolved scenarios of Scenarios 8 and 9, which account for debris flow surges, perform poorer than the spatially resolved scenarios of Scenarios 4 and 6, which do not account for debris flow surges as seen in Figure 4.13 and Figure 4.14. On average, the spatially resolved scenarios (Scenarios 4 and 6) achieve an area coverage of 85.5% and an area outrun ratio of 1.9. The time-resolved scenarios (8 and 9) have a lower average area coverage of 73% and a higher area outrun ratio of 2.09, indicating both lower accuracy and lower precision, respectively. Therefore, it can be said that accounting for debris flow surging caused by non-simultaneous landslides in the Mocoa 2017 event does not improve the accuracy of runout analysis. Thus answering the main research question.

Section 4.1.1 shows that an increase in spatial resolution from Scenario 3 (single basin) to Scenario 4 (four sub-basins) to Scenario 6 (seven sub-basins) improves the accuracy and precision of runout prediction as evidenced by the area coverage ratio increasing from 45% to 83% to 88%, respectively as seen in Figure 4.13. As well as by the area outrun ratio decreasing from 2.21 to 2.08 to 1.79, respectively, as seen in Figure 4.14. Thus, the first sub-research question was positively answered by showing that an increase in spatial resolution does improve debris flow runout analysis.

Section 4.1 the analysis of Scenarios 1 and 2 shows that utilising the exact landslide areas conflicts with the depth-averaged assumption by creating high block releases. Use of the precise release areas is also constrained by the low resolution of the D.E.M. ($12.5m$), which does not represent small gullies, thereby providing inaccurate flow paths for individually mobilised landslides, resulting in low area coverage ratios (62% and 52% for Scenarios 1 and 2) as seen in Figure 4.13 along with high area outrun ratios (4.4 and 4.1 for Scenarios 1 and 2 respectively) as seen in Figure 4.14. Therefore, using the mapped landslides as release locations in this case study is not suitable. This answers the second sub-research question by showing that it is not feasible in our case to directly use the locations of mapped landslides for runout analysis.

In Section 4.1.2, the low area coverage ratio, 58% on average across all three scenarios, and high average area outrun ratio, 3.1 across the three scenarios indicates that considering only the highland area does not generate an accurate portrayal of the debris flow event. Therefore, the third sub-research question on the viability of considering only the highlands as a source area is answered in the negative.

In Section 4.2, results show that there is remarkable consistency across all metrics between the scenarios that consider deposition, Scenarios 8 and 9 and the scenarios that disregard deposition, Scenarios 10 and 11. There is a negligible difference (5%) in the area coverage ratio of Scenarios 8 and 10, with Scenarios 9 and 11 showing an even lower difference of 1%. This can be seen in Figure 4.13. Consequently, this study answers the fourth and final research sub-question by showing that accounting for depositions in debris flow surges has a negligible effect on runout analysis for this case study.

4.5. Limitations of This Study and Recommendations for Future Studies

This study is subject to the following limitations:

The D.E.M. resolution of $12.5m$ for the debris flow simulation is a possible cause for error. The performance of RAMMS is sensitive to the resolution of the D.E.M. [90]. However, other debris flow studies have used resolutions from $1m$ to up to $30m$ [39] [91] [92]. As per Claessens et al. (2005) the ideal D.E.M. resolution that captures all possible slope failures in space and time may not exist, and the chosen resolution is often governed by availability and the context of the analysis [93]. We used the ALOS $12.5m$ D.E.M. as, to our knowledge, it was the highest resolution D.E.M. freely available [68]. The absolute accuracy of the simulations will increase with a better D.E.M. resolution. However, this study compares the relative performance of two methods, spatial and time-resolved debris flows, and using a single D.E.M. of $12.5m$ resolution is sufficient to facilitate such a like-for-like comparison as any inaccuracies in the D.E.M. affects both methods [90].

Erosion is expected in debris flows of this size. Without reliable information, such as the erosion rate associated with the event, this study is unable to include the phenomena in our simulations. Instead, the estimated entrained volume was included in the debris flow volume at the start of the simulation. Therefore, volumes representative of the actual event were used in the simulation.

There is a possibility that the rheological parameters obtained from Correa (2023) could be further calibrated for each scenario [48]. However, by using a single set of parameters for all scenarios, we could focus on the difference caused by the spatial and time resolution of the event.

This study could not model the remobilisation of material deposited in preceding time steps by flow in successive time steps due to the inability of RAMMS to model releases delayed by over 1000 seconds between each other within a single simulation. However, given the considerable duration between surges in our simulation (at least six hours), we do not consider this to have had a significant effect. Moreover, there was little to no variation in performance between scenarios that considered deposition altering the topography and those that did not. A hydrograph release is recommended by the developers of RAMMS for channelised debris flows to avoid large initial release heights ($> 10m$) (RAMMS::DEBRISFLOW User Manual, 2022, p. 87) [49]. However, RAMMS does not allow for multiple hydrograph releases within a simulation. Using a single hydrograph would prevent spatially resolving the debris flow source area. This limitation is overcome by implementing multiple block releases with heights lower than ten metres.

Precipitation data was measured at a single station several kilometres ($5 - 9km$) away and at a lower elevation from the highland region, where the majority of instabilities were observed. However, the Mocoa Aqueducto was the closest meteorological station and had to suffice for this analysis.

The unstable volumes generated by TRIGRS were assumed proportionate to the landslide volume generated in the basins and wholly mobilised at the end of the six-hour interval being considered. In reality, the instabilities are generated throughout the interval per the time evolution of pore pressure and may or may not develop into debris flows [27]. A proposal could be made to vary the time resolution of the event or increase it for a specific duration within the four days we considered after reassessing the groundwater level. For example, a decreased hourly interval could be considered closer to the time of the event or when significant volumes are indicated as unstable. This would be an interesting avenue for future studies to explore as Viet et al. (2017) have shown that TRIGRS tends to predict failure earlier than when it occurs rather than later [85].

There is a discrepancy between the simulated velocities and those ascribed to the event by García-Delgado et al. (2019). Given (a) the low velocities estimated across all our scenarios compared to the velocity calculated by García-Delgado et al. (2019) and those reported by eyewitnesses to the event [2] [43] and (b) the fact that residents did not report the surges that were simulated to travel towards inhabited areas in the days preceding the event as predicted by TRIGRS. We suspect that some of the predicted instabilities by TRIGRS in response to the rainfall, although consistent with the landslide inventory, may have been landslides that did not instantaneously mobilise into debris flow surges to the degree we assumed them to have done at the start of this study. According to Ruiz (2020), some landslides created dams across the creeks and rivers [94]. Ruiz (2020) recognised at least five dam sites along the Taruquita Creek and three along the Taruca Creek, estimating a reservoir volume of almost $25,000m^3$, which is not more than 10% of our total landslide volume [94]. However, this volume could have had a significant impact on debris flow velocity as Ruiz (2020) states that the formation of dams along the creek and the subsequent sudden failure of several dams sequentially along the creeks by the heavy rainfall generated high speeds ascribed to the debris flow event due to the stored potential energy being converted to kinetic energy [94]. This mechanism of surging is different from those described by Hungr (2005) as being typical of debris flows and would benefit from further study [16]. Conversely, Cordon et al. (2020) have shown that of the 534 shallow landslides associated with the Mocoa multi-hazard event 511 contributed to the debris and mud flows, some occurring in swarms and others separately [95]. This number differs from the 273 landslides of our analysis as it includes landslides that were not officially mapped due to inaccessible terrain as well as those pertaining to the multi-hazard event and, therefore, are not limited to those landslides that contributed to the debris flow. [95]. This goes to show that there is evidence of non-simultaneous landslides that could cause surging. It is unlikely that the surging mechanisms are mutually exclusive, which is why it is fair to say that one or more mechanisms could have occurred to varying extents. However, without measurements taken during the debris flow, it is difficult to determine which mechanism influenced the debris flow and to what degree it did so. A future study could examine a case where such measurements are available.

5

Conclusion

This study began by highlighting the dangers of rainfall-triggered shallow landslides and debris flows and by providing an overview of how such hazards are assessed. It introduced the phenomenon of surging and reviewed literature that had addressed debris flow surges caused by non-simultaneous landslides [27] [39] [37]. The limited understanding of the effects of surging caused by non-simultaneous landslides on the accuracy of runout analysis was identified as a research gap, along with the particular absence of case studies assessing surging with long runouts. A case study involving the Mocoa, 2017 event in Colombia was introduced as it is one of few thoroughly studied debris flow events that involved hundreds of landslides (273), making it an ideal candidate for our study [45] [2].

The core research question; Does accounting for debris flow surging caused by non-simultaneous landslides improve the accuracy of runout analysis in the Mocoa, 2017 event? (Scenarios 3, 4, 6, and 8-11); is answered by specific simulation scenarios along with four sub-research questions : (a) How does the spatial resolution of debris flow source areas affect the accuracy of the runout simulation? (Scenarios 1, 3, 4, and 6), (b) Is it feasible to utilise the landslide inventory for the exact location of shallow landslides to simulate the runout? (Scenarios 1, and 2), (c) Is it adequate to consider only the highland region as a source area for accurate runout simulation? (Scenarios 2, 5, and 7) (d) Does the deposition between debris flow surges significantly affect the simulated runout? (Scenarios 8-11). A methodology was introduced to answer each question, with a landslide inventory provided by the Colombian Geological Service informing this study [45]. Following a landslide inventory analysis where the volume of landslides and the contribution of erosion are determined, the study area was divided into smaller source areas or sub-basins using stream orders; as part of this process, the eleven scenarios mentioned earlier were introduced along with the main tools of this study. RAMMS, a depth-averaged continuum model, is used to simulate and analyse debris flow runout with parameters for the Voellmy rheological model obtained from Correa (2023) for all scenarios [48]. TRIGRS, a process-based landslide susceptibility model, was implemented using parameters from Chavarro et al. (2020) to identify the development of slope instability during a one-hundred-and-two-hour storm period (four days and six hours). This led to the identification of five debris flow surges, which were then simulated in Scenarios 8 to 11 [87].

Of the eleven scenarios, Scenarios 1 and 2 were based on release areas from the mapped landslides and differed based on the source area considered. Scenario 1 considered the whole source area, while Scenario 2 considered only the highland area. Scenario 3 represented the lowest spatial resolution by considering the entire area as a single source basin. Scenarios 4 and 6 introduce a spatial resolution of the source area by considering four and seven sub-basins, respectively. These sub-basins were demarcated based on the Strahler stream order algorithm in keeping with observations of debris flow behaviour and basin morphometry made by Hungr (2005) and De Haas et al. (2024) [16] [70]. Scenarios 5 and 7 were designed as subsets of Scenario 4 and 6, respectively, using the same spatial resolution of their parent scenarios but considering only the highland source area. Scenarios 8 and 9 were also based on Scenarios 4 and 6, respectively, sharing the same spatial resolution of each scenario, but with the addition of a time resolution of debris flow events made possible by using TRIGRS, allowing them to simulate surging. Scenarios 10 and 11 are based on Scenarios 8 and 9, respec-

tively, differing only by their omission of debris flow surge deposits. These scenarios were simulated in RAMMS using block releases, and the results were analysed using the two key performance criteria of Area Coverage Ratio, which acts as a measure of the simulation's accuracy by measuring the area covered by the simulated debris flow versus the actual area covered by the debris flow, and Area Overrun Ratio which measures the simulated flow outside of the actual runout versus the simulated flow within the actual runout, thereby acting as a measure of the simulation's precision. Simulated velocities and runout heights were also plotted and measured at three key sections, representing three stages of the flow from an area surrounded by little infrastructure to moderate to high infrastructure, respectively. Based on these measurements, the scenarios were compared, and the results were discussed along with limitations of the study, such as the absence of measured flow data during the event, which prevented this study from determining the extent of surging that occurred in reality.

The main conclusions from this work are; With regard to the main research question of how accounting for debris flow surges affected runout analysis? Based on the two area ratios, it is found that the time-resolved scenarios of 8 and 9, which account for debris flow surges, perform poorer than the spatially resolved scenarios of 4 and 6, which do not account for debris flow surges. On average, the spatially resolved scenarios of 4 and 6 achieve a coverage area of 85.5% and an average area outrun ratio of 1.9. The time-resolved scenarios of 8 and 9 have a lower average coverage area of 73% and a higher average area outrun ratio of 2.09, indicating both lower accuracy and lower precision, respectively. Therefore, accounting for debris flow surging caused by non-simultaneous landslides in the Mocoa 2017 event does not improve the accuracy of runout analysis, thus answering the main research question.

The first research sub-question is answered by finding that a greater spatial resolution of events increases the accuracy and precision of runout analysis. An increase in spatial resolution from Scenario 3 (single basin) to Scenario 4 (four sub-basins) to Scenario 6 (seven sub-basins) improves the accuracy and precision of runout prediction as evidenced by the area coverage ratio increasing from 45% to 83% to 88% and the area outrun ratio decreasing from 2.21 to 2.08 to 1.79, respectively. Thus, the first sub-research question is answered by showing that an increase in spatial resolution improves debris flow runout analysis.

The second sub-research question concerning the use of the mapped landslides as release locations was answered by the finding that doing so created poor predictions of runout and violated the depth-averaged assumption made by RAMMS because it necessitated large (>10m) block heights. The results of Scenarios 1 and 2 show that utilising the exact landslide areas conflicts with the depth-averaged assumption by creating high block releases and that the precise nature of the release areas is constrained by the low resolution of the D.E.M., which does not represent small gullies thereby providing inaccurate flow paths for individually mobilised landslides and low area coverage ratios (62% and 52% for Scenarios 1 and 2, respectively) along with high area outrun ratios (4.4 and 4.1 for Scenarios 1 and 2 respectively).

Addressing the third sub-research question, this study found that considering only the highland region as a source area made for a poorer runout prediction than when the whole area was considered. Evidence of the poor prediction is seen by the low area coverage ratio, 58% on average across all three scenarios 2, 5, and 7, along with a high average area outrun ratio of 3.1 across the three scenarios, indicates that considering only the highland area does not generate an accurate portrayal of the debris flow event. Thereby answering the third sub-research question on the viability of considering only the highlands as a source area.

Finally, the fourth research sub-question was answered by the uniformity between all the time-resolved scenarios, showing that neglecting deposition between surges has a negligible effect on runout prediction for the Mocoa event. Results are consistent across all metrics between the scenarios that consider deposition, Scenarios 8 and 9, and those scenarios that disregard deposition, Scenarios 10 and 11. There is a negligible difference (5%) in the area coverage ratio of Scenarios 8 and 10, with Scenarios 9 and 11 showing an even lower difference of 1%. Consequently, this study answers the fourth and final research sub-question by showing that accounting for depositions in debris flow surges has a negligible effect on runout analysis for this case study.

These findings are subject to limitations, particularly the absence of measured data during the event,

which prevents the determination of the extent of surging associated with the debris flow. Other limitations include; a low D.E.M. resolution of $12.5m$ with its consequential inaccuracies, a single source for precipitation data across the entire study area, not simulating erosion caused by the debris flow, rheological parameters that are not calibrated specifically for each scenario, the inability to model the remobilization of debris between surges and an assumption that the instabilities generated by TRIGRS are proportionate to the landslide volume generated in the basins and are completely mobilised at the end of each six-hour interval.

In summary, this study introduced a method to spatially resolve debris flow source areas and simulated runout to a near 90% accuracy based on the area coverage ratio of Scenarios 4 and 6. This study also showed that increasing the spatial resolution by dividing the source area into as many as seven sub-basins improves runout prediction and that using the mapped landslides as release areas or considering only the highland area decreases the accuracy of the simulation based on the area coverage ratios. Finally, this study conclusively demonstrated that accounting for debris flow surging caused by non-simultaneous shallow landslides with or without including surge deposition does not improve the forensic analysis of the Mocoa 2017 event.

References

[1] D. Sim, Saldarriaga.J, and Reuters. *Aerial photo show scale of devastation in mudslide-hit Colombian city of Mocoa*. Web Page. 2017. URL: https://www.ibtimes.co.uk/aerial-photos-show-scale-devastation-mudslide-hit-colombian-city-mocoa-1615234.

[2] L. Prada Sarmiento, M. Cabrera, R. Camacho, N. Estrada, and A. Ramos. "The Mocoa Event on March 31 (2017): analysis of a series of mass movements in a tropical environment of the Andean-Amazonian Piedmont". In: *Landslides* 16 (2019), pp. 1–10. DOI: 10.1007/s10346-019-01263-y.

[3] M. J. Froude and D. N Petley. "Global fatal landslide occurrence from 2004 to 2016". In: *Nat. Hazards Earth Syst. Sci* 18. 2161–2181 (2018). DOI: https://doi.org/10.5194/nhess-18-2161-2018. URL: https://nhess.copernicus.org/articles/18/2161/2018/nhess-18-2161-2018.pdf.

[4] Scientific Visualization Studio NASA. *Global Landslide Hazard Assessment Model (LHASA) with Global Landslide Catalog (GLC) data*. Web Page. 2018. URL: https://svs.gsfc.nasa.gov/4710/.

[5] M. Van Den Eeckhaut and J. Hervás. "State of the art of national landslide databases in Europe and their potential for assessing landslide susceptibility, hazard and risk". In: *Geomorphology* 139-140 (2012), pp. 545–558. ISSN: 0169-555X. DOI: https://doi.org/10.1016/j.geomorph.2011.12.006. URL: https://www.sciencedirect.com/science/article/pii/S0169555X11006192.

[6] C Dandridge, T. A. Stanley, D. B. Kirschbaum, and V. Lakshmi. "Spatial and Temporal Analysis of Global Landslide Reporting Using a Decade of the Global Landslide Catalog". In: *Sustainability* 15.4 (2023), p. 3323. ISSN: 2071-1050. DOI: 10.3390/su15043323. URL: https://dx.doi.org/10.3390/su15043323.

[7] UNDRR. *Human cost of disasters - An overview of the last 20 years 2000-2019*. Report. Centre for Research on the Epidemiology of Disasters., 2020.

[8] M Larsen, G. Wieczorek, L Eaton, and H. Torres Sierra. "NATURAL HAZARDS ON ALLUVIAL FANS: THE DEBRIS FLOW AND FLASH FLOOD DISASTER OF DECEMBER 1999, VARGAS STATE, VENEZUELA". In: *Proceedings of the Sixth Caribbean IslandsWater Resources Congress* (2001).

[9] D. Cheng, Y. Cui, F. Su, Y. Jia, and C. Choi. "The characteristics of the Mocoa compound disaster event, Colombia." In: *Landslides.* 15 (2018). DOI: 10.1007/s10346-018-0969-1.

[10] H. Pei Y.and Qiu, D. Yang, S. Liu Z.and Ma, J. Li, M. Cao, and W. Wufuer. "Increasing landslide activity in the Taxkorgan River Basin (eastern Pamirs Plateau, China) driven by climate change". In: *CATENA* 223 (2023). Increase of landslides with global warming, p. 106911. ISSN: 0341-8162. DOI: https://doi.org/10.1016/j.catena.2023.106911. URL: https://www.sciencedirect.com/science/article/pii/S0341816223000024.

[11] UNISDR. *Words into Action Guidelines:National Disaster RiskAssessment Hazard Specific Risk Assessment*. Government Document. 2017.

[12] P. Redshaw and J Bottomley. *The Global Landslide Hazard Map Final Project Report*. Report. The World Bank and Arup, 2020. URL: https://datacatalog.worldbank.org/search/dataset/0037584/Global-landslide-hazard-map.

[13] O. Hungr, S. Leroueil, and L. Picarelli. "The Varnes classification of landslide types, an update". In: *Landslides* 11 (2014). DOI: 10.1007/s10346-013-0436-y..

[14] L.M Highland and P. Bobrowsky. *The landslide handbook—A guide to understanding landslides*. Report. U.S. Geological Survey, 2008.

[15] M. Lynn Highland and Johnson. *Landslide Types and Processes*. Government Document. 2006. URL: http://pubs.usgs.gov/fs/2004/3072/.

[16] O. Hungr. “Classification and terminology”. In: *Debris-flow Hazards and Related Phenomena*. Ed. by Matthias Jakob and Oldrich Hungr. Berlin, Heidelberg: Springer Berlin Heidelberg, 2005, pp. 9–23. ISBN: 978-3-540-27129-1. DOI: 10.1007/3-540-27129-5_2. URL: https://doi.org/10.1007/3-540-27129-5_2.

[17] M. Jakob. “A size classification for debris flows”. In: *Engineering Geology* 79 (July 2005), pp. 151–161. DOI: 10.1016/j.enggeo.2005.01.006.

[18] O. Hungr, S. Evans, M. Bovis, and J. N. Hutchinson. “Review of the classification of landslides of the flow type”. In: *Environmental and Engineering Geoscience* 7 (2001), pp. 221–238. DOI: 10.2113/gseegeosci.7.3.221.

[19] J. W. Vallance. “Lahars: Origins, Behavior and Hazards”. In: *Advances in Debris-flow Science and Practice*. Ed. by M. Jakob, S. McDougall, and Paul Santi. Cham: Springer International Publishing, 2024, pp. 347–382. ISBN: 978-3-031-48691-3. DOI: 10.1007/978-3-031-48691-3_12. URL: https://doi.org/10.1007/978-3-031-48691-3_12.

[20] R. M. Iverson. “Debris-flow mechanics”. In: *Debris-flow Hazards and Related Phenomena*. Berlin, Heidelberg: Springer Berlin Heidelberg, 2005, pp. 105–134. ISBN: 978-3-540-27129-1. DOI: 10.1007/3-540-27129-5_6. URL: https://doi.org/10.1007/3-540-27129-5_6.

[21] R. M. Iverson and D. L. George. “Numerical Modeling of Debris Flows: A Conceptual Assessment”. In: *Advances in Debris-flow Science and Practice*. Ed. by Matthias Jakob, Scott McDougall, and Paul Santi. Cham: Springer International Publishing, 2024, pp. 127–163. ISBN: 978-3-031-48691-3. DOI: 10.1007/978-3-031-48691-3_5. URL: https://doi.org/10.1007/978-3-031-48691-3_5.

[22] T. C. Pierson. “Hyperconcentrated flow — transitional process between water flow and debris flow”. In: *Debris-flow Hazards and Related Phenomena*. Berlin, Heidelberg: Springer Berlin Heidelberg, 2005, pp. 159–202. ISBN: 978-3-540-27129-1. DOI: 10.1007/3-540-27129-5_8. URL: https://doi.org/10.1007/3-540-27129-5_8.

[23] C. A. Dowling and P. M. Santi. “Debris flows and their toll on human life: a global analysis of debris-flow fatalities from 1950 to 2011”. In: *Natural Hazards* 71.1 (2014), pp. 203–227. ISSN: 1573-0840. DOI: 10.1007/s11069-013-0907-4. URL: https://doi.org/10.1007/s11069-013-0907-4.

[24] T. C. Pierson. “Flow behavior of channelized debris flows, Mount St. Helens, Washington, in: Hillslope Processes, the Binghamton symp”. In: *Geomorphology* (1986), pp. 269–296.

[25] P. Reichenbach, M. Rossi, B. D. Malamud, M. Mihir, and F. Guzzetti. “A review of statistically-based landslide susceptibility models”. In: *Earth-Science Reviews* 180 (2018), pp. 60–91. ISSN: 0012-8252. DOI: https://doi.org/10.1016/j.earscirev.2018.03.001. URL: https://www.sciencedirect.com/science/article/pii/S0012825217305652.

[26] S. McDougall. “2014 Canadian Geotechnical Colloquium: Landslide runout analysis — current practice and challenges”. In: *Canadian Geotechnical Journal* 54.5 (2016). doi: 10.1139/cgj-2016-0104, pp. 605–620. ISSN: 0008-3674. DOI: 10.1139/cgj-2016-0104. URL: https://doi.org/10.1139/cgj-2016-0104.

[27] G. La Porta, A. Leonardi, M. Pirulli, F. Cafaro, and F. Castelli. “Time-resolved triggering and runout analysis of rainfall-induced shallow landslides”. In: *Acta Geotechnica* (2023), pp. 1–17. DOI: 10.1007/s11440-023-01996-0.

[28] F. G. Murillo Garcia and I. Alcantara-Ayala. “Landslide Susceptibility Analysis and Mapping Using Statistical Multivariate Techniques: Pahuatlán, Puebla, Mexico”. In: Springer International Publishing, 2015, pp. 179–194. DOI: 10.1007/978-3-319-11053-0_16. URL: https://dx.doi.org/10.1007/978-3-319-11053-0_16.

[29] Muge P. Komu, Hakan A. Nefeslioglu, and Candan Gokceoglu. *A Review of the Prediction Methods for Landslide Runout*. Electronic Article. 2023. DOI: 10.3390/IECG2022-14604.

[30] S. Sinha and G. Walton. “Understanding continuum and discontinuum models of rock-support interaction for excavations undergoing stress-induced spalling”. In: *International Journal of Rock Mechanics and Mining Sciences* 123 (2019), p. 104089. ISSN: 1365-1609. DOI: https://doi.org/10.1016/j.ijrmms.2019.104089. URL: https://www.sciencedirect.com/science/article/pii/S1365160919305921.

[31] M. Jakob. “Debris-flow hazard analysis”. In: *Debris-flow Hazards and Related Phenomena*. Ed. by Matthias Jakob and Oldrich Hungr. Berlin, Heidelberg: Springer Berlin Heidelberg, 2005, pp. 411–443. ISBN: 978-3-540-27129-1. DOI: 10.1007/3-540-27129-5_17. URL: https://doi.org/10.1007/3-540-27129-5_17.

[32] T. Corthouts. *Debris Flow, cirque wall, Sacagawea Trail*. Web Page. 2009. URL: https://serc.carleton.edu/download/images/18152/debris_flow_marginal_levees.webp.

[33] P. Strouth A.and LeSueur, S. Zubrycky, F. de Vilder S.and Lo, K. Ho, and S. McDougall. “Debris-Flow Risk Assessment”. In: *Advances in Debris-flow Science and Practice*. Ed. by Matthias Jakob, Scott McDougall, and Paul Santi. Cham: Springer International Publishing, 2024, pp. 433–493. ISBN: 978-3-031-48691-3. DOI: 10.1007/978-3-031-48691-3_14. URL: https://doi.org/10.1007/978-3-031-48691-3_14.

[34] C. Ouyang, Z. Wang, H. An, X. Liu, and D. Wang. “An example of a hazard and risk assessment for debris flows—A case study of Niwan Gully, Wudu, China”. In: *Engineering Geology* 263 (2019), p. 105351. ISSN: 0013-7952. DOI: https://doi.org/10.1016/j.enggeo.2019.105351. URL: https://www.sciencedirect.com/science/article/pii/S0013795218316867.

[35] M. Arai, J. Hubl, and R. Kaitna. “Occurrence conditions of roll waves for three grain-fluid models and comparison with results from experiments and field observation”. In: *Geophysical Journal International* 195 (Dec. 2013), pp. 1464–1480. DOI: 10.1093/gji/ggt352.

[36] R. M. Iverson and David L. George. “Numerical Modeling of Debris Flows: A Conceptual Assessment”. In: *Advances in Debris-flow Science and Practice*. Ed. by Matthias Jakob, Scott McDougall, and Paul Santi. Cham: Springer International Publishing, 2024, pp. 127–163. DOI: 10.1007/978-3-031-48691-3_5. URL: https://doi.org/10.1007/978-3-031-48691-3_5.

[37] L. Stancanelli, D. Peres, A. Cancelliere, and E. Foti. “A combined triggering-propagation modeling approach for the assessment of rainfall induced debris flow susceptibility”. In: *Journal of Hydrology* 550 (2017). DOI: 10.1016/j.jhydrol.2017.04.038.

[38] D. J. Peres and A Cancelliere. “Estimating return period of landslide triggering by Monte Carlo simulation”. In: *Journal of Hydrology* 541 (2016), pp. 256–271. ISSN: 0022-1694. DOI: https://doi.org/10.1016/j.jhydrol.2016.03.036.

[39] W. Zhou, H. Qiu, L. Wang, Y. Pei, B. Tang, D. Ma S.and Yang, and M. Cao. “Combining rainfall-induced shallow landslides and subsequent debris flows for hazard chain prediction”. In: *CATENA* 213 (2022), p. 106199. ISSN: 0341-8162. DOI: https://doi.org/10.1016/j.catena.2022.106199. URL: https://www.sciencedirect.com/science/article/pii/S0341816222001850.

[40] R.L. Baum, W.Z. Savage, and J.W. Godt. *TRIGRS—A Fortran program for transient rainfall infiltration and grid-based regional slope-stability analysis, version 2.0*. Report. U.S. Geological Survey, 2008.

[41] Britannica The Editors of Encyclopaedia. “Mocoa”. In: (2008). URL: https://www.britannica.com/place/Mocoa.

[42] W. Sirko, S. Kashubin, M. Ritter, A. Annkah, Y. S. E. Bouchareb, Y. Dauphin, M. Keysers D.and Neumann, M. Cisse, and J. A. Quinn. “Continental-scale building detection from high resolution satellite imagery”. In: *arXiv preprint arXiv:2107.12283* (2021).

[43] H. Garcia Delgado, S. Machuca, and E. Medina Bello. “Dynamic and geomorphic characterizations of the Mocoa Debris Flow (March 31st, 2017, Putumayo Department, Southern Colombia)”. In: *Landslides* 16 (2019), pp. 597–609. DOI: 10.1007/s10346-018-01121-3.

[44] M. L. Zimmermann. *Colombia:un desastre ambiental anunciado*. Web Page. 2017. URL: https://es.mongabay.com/2017/04/colombia-desastre-ambiental-anunciado/.

[45] H. García-Delgado, E. Medina Bello, and S. Machuca. *Caracterización del movimiento en masa tipo flujo del 31 de marzo de 2017 en Mocoa–Putumayo*. Jan. 2018. DOI: 10.13140/RG.2.2.18803.43045.

[46] N. Reyes Gil, M. Barros, C. Fuentes, C. Barajas, J. Escobar-Vargas, L. Prada Sarmiento, and A. Ramos. "Simulación integrada comparativa de avenidas torrenciales. Caso de estudio: Mocoa - Colombia." In: Sept. 2018.

[47] N. Prakash, P. Santi, A. Strouth, S. A. Sepulveda, and C. Dowling. "Fatalities from Debris Flows: Worldwide Distribution and Trends". In: *Advances in Debris-flow Science and Practice*. Ed. by Matthias Jakob, Scott McDougall, and Paul Santi. Cham: Springer International Publishing, 2024, pp. 75–91. ISBN: 978-3-031-48691-3. DOI: 10.1007/978-3-031-48691-3_3. URL: https://doi.org/10.1007/978-3-031-48691-3_3.

[48] M. I. L. Correa. "Numerical modeling of debris flows. Application to Rebaixader (Pyrenees) and Mocoa (Colombia)". Thesis. Universitat Politecnica de Catalunya, 2023.

[49] *RAMMS::DEBRISFLOW User Manual v1.8.0 (2022). Davos, Svizzera: WSL Institute for Snow and Avalanche.*

[50] F. Frank, B. W. McArdell, C. Huggel, and A. Vieli. "The importance of entrainment and bulking on debris flow runout modeling: examples from the Swiss Alps". In: *Nat. Hazards Earth Syst. Sci.* 15.11 (2015). NHESS, pp. 2569–2583. ISSN: 1684-9981. DOI: 10.5194/nhess-15-2569-2015. URL: https://nhess.copernicus.org/articles/15/2569/2015/.

[51] P. Bartelt, Y. Buhler, O. Buser, M. Christen, and L. Meier. "Modeling mass□dependent flow regime transitions to predict the stopping and depositional behavior of snow avalanches". In: *Journal of Geophysical Research: Earth Surface* 117.F1 (2012). DOI: 10.1029/2010jf001957.

[52] S. B. Savage and K. Hutter. "The motion of a finite mass of granular material down a rough incline". In: *Journal of Fluid Mechanics* 199.2697 (1989). Export Date: 17 February 2024; Cited By: 1405, pp. 177–215. DOI: 10.1017/S0022112089000340. URL: https://www.scopus.com/inward/record.uri?eid=2-s2.0-0024611991&doi=10.1017%2fS0022112089000340&partnerID=40&md5=62444f9ca65fda5c80a4b08a2a21ef2b.

[53] S. B. Savage and K. Hutter. "The dynamics of avalanches of granular materials from initiation to runout. Part I: Analysis". In: *Acta Mechanica* 86.1-4 (1991). Export Date: 17 February 2024; Cited By: 376, pp. 201–223. DOI: 10.1007/BF01175958. URL: https://www.scopus.com/inward/record.uri?eid=2-s2.0-0025721526&doi=10.1007%2fBF01175958&partnerID=40&md5=865a0498806f1f8ffbe134c63a0e4663.

[54] F. Vagnon, M. Pirulli, I. Manzella, K. Kelfoun, and A. M. Ferrero. "Numerical analysis of the rheological behaviour of the socompa debris avalanche, Chile". In: *Geomechanics and Geodynamics of Rock Masses - Selected Papers from the 2018 European Rock Mechanics Symposium, EUROCK 2018*. Export Date: 01 January 2024; Cited By: 2, pp. 409–414. URL: https://www.scopus.com/inward/record.uri?eid=2-s2.0-85063635459&partnerID=40&md5=5db06e5099d9a3ae068e395648f7c5e5.

[55] M. Christen, J. Kowalski, and P. Bartelt. "RAMMS: Numerical simulation of dense snow avalanches in three-dimensional terrain". In: *Cold Regions Science and Technology* 63 (2010), pp. 1–14. DOI: 10.1016/j.coldregions.2010.04.005.

[56] R. M. Iverson. "Debris-flow mechanics". In: *Debris-flow Hazards and Related Phenomena*. Ed. by Matthias Jakob and Oldrich Hungr. Berlin, Heidelberg: Springer Berlin Heidelberg, 2005, pp. 105–134. ISBN: 978-3-540-27129-1. DOI: 10.1007/3-540-27129-5_6. URL: https://doi.org/10.1007/3-540-27129-5_6.

[57] F. Zimmermann, B. W. McArdell, C. Rickli, and C. Scheidl. "2D Runout Modelling of Hillslope Debris Flows, Based on Well-Documented Events in Switzerland". In: *Geosciences* 10.2 (2020), p. 70. ISSN: 2076-3263. URL: https://www.mdpi.com/2076-3263/10/2/70.

[58] A. Simoni, M. Mammoliti, and C. Graf. *Performance of 2D debris flow simulation model RAMMS. Back-analysis of field events in Italian Alps*. 2012. DOI: 10.5176/2251-3361_GEOS12.59.

[59] M. A. Khan, Z. Mustaffa, A. L. B. Balogun, M. A. M. Al-Bared, and A. Ahmad. “Role of the Rheological Parameters in Debris Flow Modelling”. In: *IOP Conference Series: Materials Science and Engineering* 1092.1 (2021), p. 012041. DOI: 10.1088/1757-899X/1092/1/012041. URL: https://dx.doi.org/10.1088/1757-899X/1092/1/012041.

[60] C. Scheidl, . Rickenmann, and B. W. McArdell. “Runout Prediction of Debris Flows and Similar Mass Movements”. In: *Landslide Science and Practice: Volume 3: Spatial Analysis and Modelling*. Ed. by Claudio Margottini, Paolo Canuti, and Kyoji Sassa. Berlin, Heidelberg: Springer Berlin Heidelberg, 2013, pp. 221–229. ISBN: 978-3-642-31310-3. DOI: 10.1007/978-3-642-31310-3_30. URL: https://doi.org/10.1007/978-3-642-31310-3_30.

[61] J.T. Fischer, J. Kowalski, and S. P. Pudasaini. “Topographic curvature effects in applied avalanche modeling”. In: *Cold Regions Science and Technology* 74-75 (2012), pp. 21–30. ISSN: 0165-232X. DOI: https://doi.org/10.1016/j.coldregions.2012.01.005.

[62] G. Meyrat, J. Munch, A. Cicoira, B. McArdell, C. R. Müller, H. Frey, and P. Bartelt. “Simulating glacier lake outburst floods (GLOFs) with a two-phase/layer debris flow model considering fluid-solid flow transitions”. In: *Landslides* 21.3 (2024), pp. 479–497. ISSN: 1612-5118. DOI: 10.1007/s10346-023-02157-w. URL: https://doi.org/10.1007/s10346-023-02157-w.

[63] P. Bartelt, B. Salm, and U. Gruber. “Calculating dense-snow avalanche runout using a Voellmy-fluid model with active/passive longitudinal straining”. In: *Journal of Glaciology* 45.150 (1999), pp. 242–254. ISSN: 0022-1430. DOI: 10.3189/S002214300000174X.

[64] R. Dash, D. Kanungo, and J. P. Malet. “Runout modelling and hazard assessment of Tangni debris flow in Garhwal Himalayas, India”. In: *Environmental Earth Sciences* 80 (2021). DOI: 10.1007/s12665-021-09637-z.

[65] Y. Deubelbeiss. “Two different starting conditions in numerical debris-flow models - case study at Dorfbach, Randa (Valais, Switzerland)”. In: *Mattertal - ein Tal in Bewegung* (2013), p. 125.

[66] F. Frank, B. W. McArdell, N. Oggier, P. Baer, M. Christen, and A. Vieli. “Debris-flow modeling at Meretschibach and Bondasca catchments, Switzerland: sensitivity testing of field-data-based entrainment model”. In: *Nat. Hazards Earth Syst. Sci.* 17.5 (2017). NHESS, pp. 801–815. ISSN: 1684-9981. DOI: 10.5194/nhess-17-801-2017. URL: https://nhess.copernicus.org/articles/17/801/2017/.

[67] H.Y. Hussin, B. Quan Luna, C.J. van Westen, M. Christen, J.P. Malet, and Th.W.J. van Asch. “Parameterization of a numerical 2-D debris flow model with entrainment: a case study of the Faucon catchment, Southern French Alps”. In: *Nat. Hazards Earth Syst. Sci.* 12.10 (2012). NHESS, pp. 3075–3090. ISSN: 1684-9981. DOI: 10.5194/nhess-12-3075-2012. URL: https://nhess.copernicus.org/articles/12/3075/2012/.

[68] ALPSRP224070000-RTC-HI-RES; Includes Material JAXA/METI 2023 JAXA/METI ALOS PALSAR ASF DAAC 2014. Online Database. Accessed through ASF DAAC on 1-02-2024. URL: www.asf.alaska.edu.

[69] Esri and D. Djokic. “Creating a Hydrologically Conditioned DEM”. In: URL: https://proceedings.esri.com/library/userconf/proc15/tech-workshops/tw_897-156.pdf#:~:text=Hydrologically%20conditioned%20DEM%20%28Hydro%20DEM%29%20is%20a%20DEM,pattern%2C%20not%20the%20actual%20elevation%20in%20the%20DEM..

[70] T. de Haas, C.A. Lau, and D. Ventra. “Debris-Flow Watersheds and Fans: Morphology, Sedimentology and Dynamics”. In: *Advances in Debris-flow Science and Practice*. Ed. by Matthias Jakob, Scott McDougall, and Paul Santi. Cham: Springer International Publishing, 2024, pp. 9–73. ISBN: 978-3-031-48691-3. DOI: 10.1007/978-3-031-48691-3_2. URL: https://doi.org/10.1007/978-3-031-48691-3_2.

[71] D. Tarboton. “A new method for the determination of flow directions and upslope areas in grid digital elevation models”. In: *Water Resources Research* 33.2 (1997), pp. 309–319. DOI: https://doi.org/10.1029/96WR03137. eprint: https://agupubs.onlinelibrary.wiley.com/doi/pdf/10.1029/96WR03137. URL: https://agupubs.onlinelibrary.wiley.com/doi/abs/10.1029/96WR03137.

[72] D. Greenlee. “Raster and vector processing for scanned linework”. In: *Photogrammetric Engineering and Remote Sensing* 53 (1987), pp. 1383–1387. URL: https://api.semanticscholar.org/CorpusID:51852908.

[73] Esri. “Flow Direction (Spatial Analyst)”. In: (2024). URL: https://desktop.arcgis.com/en/arcmap/latest/tools/spatial-analyst-toolbox/flow-direction.htm.

[74] Esri. “Flow Accumulation (Spatial Analyst)”. In: (2024). URL: https://desktop.arcgis.com/en/arcmap/latest/tools/spatial-analyst-toolbox/flow-accumulation.htm.

[75] Susan K. J. and Julia O. D. “Extracting topographic structure from digital elevation data for geographic information-system analysis”. In: *Photogrammetric Engineering and Remote Sensing* 54 (1988), pp. 1593–1600. URL: https://api.semanticscholar.org/CorpusID:17401619.

[76] David Gavin Tarboton, Rafael L. Bras, and Ignacio Rodriguez□Iturbe. “On the extraction of channel networks from digital elevation data”. In: *Hydrological Processes* 5 (1991), pp. 81–100. URL: https://api.semanticscholar.org/CorpusID:35883749.

[77] Esri. *How Stream Order works*. Web Page. URL: https://pro.arcgis.com/en/pro-app/latest/tool-reference/spatial-analyst/how-stream-order-works.htm.

[78] ESRI. *How Watershed works*. Web Page. URL: https://pro.arcgis.com/en/pro-app/latest/tool-reference/spatial-analyst/how-watershed-works.htm#:~:text=The%20outlet%2C%20or%20pour%20point%2C%20is%20the%20point,lowest%20point%20along%20the%20boundary%20of%20a%20watershed..

[79] R. M. Iverson. “Landslide triggering by rain infiltration”. In: *Water Resources Research* 36.7 (2000), pp. 1897–1910. DOI: 10.1029/2000WR900090. URL: https://pubs.usgs.gov/publication/70022499.

[80] R. Srivastava and T. C. J. Yeh. “Analytical solutions for one-dimensional, transient infiltration toward the water table in homogeneous and layered soils”. In: *Water Resources Research* 27.5 (1991), pp. 753–762. ISSN: 0043-1397. DOI: https://doi.org/10.1029/90WR02772. URL: https://agupubs.onlinelibrary.wiley.com/doi/abs/10.1029/90WR02772.

[81] L. A. Richards. “CAPILLARY CONDUCTION OF LIQUIDS THROUGH POROUS MEDIUMS”. In: *Physics* 1.5 (1931), pp. 318–333. ISSN: 0148-6349. DOI: 10.1063/1.1745010. URL: https://doi.org/10.1063/1.1745010.

[82] S. Shekhar. “Darcy’s law”. In: e-PG Pathshala, UGC, MHRD, Govt. of India, Oct. 2017.

[83] D. W. Taylor. *Fundamentals of soil mechanics*. ”References”: p. 683-691. New York: J. Wiley, 1948, xii, 700 p. URL: //catalog.hathitrust.org/Record/003884917%20http://hdl.handle.net/2027/mdp.39015052877415.

[84] D. W. Park, N. V. Nikhil, and S. R. Lee. “Landslide and debris flow susceptibility zonation using TRIGRS for the 2011 Seoul landslide event”. In: *Nat. Hazards Earth Syst. Sci.* 13.11 (2013). NHESS, pp. 2833–2849. ISSN: 1684-9981. DOI: 10.5194/nhess-13-2833-2013. URL: https://nhess.copernicus.org/articles/13/2833/2013/.

[85] T. T. Viet, G. Lee, T. M. Thu, and H. Uk. An. “Effect of Digital Elevation Model Resolution on Shallow Landslide Modeling Using TRIGRS”. In: *Natural Hazards Review* 18.2 (2017). DEMCHAngesandTRIGRSgood, p. 04016011. DOI: doi:10.1061/(ASCE)NH.1527-6996.0000233. URL: https://ascelibrary.org/doi/abs/10.1061/%28ASCE%29NH.1527-6996.0000233.

[86] W. Savage and R. Baum. “Instability of steep slopes”. In: *Debris-flow Hazards and Related Phenomena*. Ed. by Matthias Jakob and Oldrich Hungr. Berlin, Heidelberg: Springer Berlin Heidelberg, 2005, pp. 53–79. ISBN: 978-3-540-27129-1. DOI: 10.1007/3-540-27129-5_4. URL: https://doi.org/10.1007/3-540-27129-5_4.

[87] A. Felipe Prieto Chavarro, Luis Felipe Prada Sarmiento, and Ramos A. *Integrated numerical model to simulate the mass movements of the Mocoa event on March 31 (2017)*. Conference Paper. 2020.

[88] N.J. Jarvis and M. Larsbo. “MACRO (V5.2): Model use, calibration, and validation”. In: *Transactions of the ASABE* 55 (July 2012), pp. 1413–1423. DOI: 10.13031/2013.42251.

[89] J. Simunek, K. Huang, M. Sejna, and M.Th. van Genuchten. *HYDRUS-1D Model*. https://www.ars.usda.gov/pacific-west-area/riverside-ca/agricultural-water-efficiency-and-salinity-research-unit/docs/model/hydrus-1d-model/. Version 3.01 [Software]. Last Modified September 9, 2020. U.S. Salinity Laboratory, USDA-ARS, Riverside, California, 2005.

[90] M. Galoie and A. Motamedi. "Evaluation of Errors and Uncertainties in Debris Flow Modeling with RAMMS". In: (2024). DOI: 10.21203/rs.3.rs-3953511/v1. URL: https://doi.org/10.21203/rs.3.rs-3953511/v1.

[91] J. He, H. Qiu, F. Qu, S. Hu, D. Yang, Y. Shen, Y. Zhang, H. Sun, and M. Cao. "Prediction of spatiotemporal stability and rainfall threshold of shallow landslides using the TRIGRS and Scoops3D models". In: *CATENA* 197 (2021), p. 104999. ISSN: 0341-8162. DOI: https://doi.org/10.1016/j.catena.2020.104999.

[92] C. Sarma, A. Dey, and A. Murali Krishna. "Influence of digital elevation models on the simulation of rainfall-induced landslides in the hillslopes of Guwahati, India". In: *Engineering Geology* 268 (2020), pp. 1–13. DOI: 10.1016/j.enggeo.2020.105523.

[93] L. Claessens, G. Heuvelink, J. M. Schoorl, and A. Veldkamp. "DEM resolution effects on shallow landslide hazard and soil redistribution modelling". In: *Earth Surface Processes and Landforms* 30 (2005), pp. 461–477. DOI: 10.1002/esp.1155.

[94] G. Ruiz. "Debris flows that affected Mocoa city, Colombia on March 31, 2017". In: *SCG-XIII INTERNATIONAL SYMPOSIUM ON LANDSLIDES- JUNE 15th-19th-2020*. INTERNATIONAL SOCIETY FOR SOIL MECHANICS and GEOTECHNICAL ENGINEERING, 2020. URL: https://www.issmge.org/uploads/publications/105/106/ISL2020-112.pdf.

[95] J. Chaparro Cordón, E. Rodriguez, M. Rangel Florez, H. García-Delgado, and E. Medina Bello. *Statistical description of some landslide inventories from Colombian Andes: study cases in Mocoa, Villavicencio, Popayán, and Cajamarca*. Oct. 2020. DOI: 10.13140/RG.2.2.17237.04327.